Chapter 5

AM01, AM03 AND AM04: SEISMIC vs AMISOR DATA

In the Antarctic summer seasons 2002/2003, 2004/2005 and 2005/2006 a series of detailed seismic CDP profiles were undertaken nearby to sites where AMISOR had hot-water drilled through the AIS to collect conductivity-temperature-depth (CTD) measurements within the water column. The purpose of these seismic surveys were:

- To test the validity of the pre-existing seismic velocity model for the AIS by comparing the model with known ice thicknesses and depths at known sites,
- To test the ability of the seismic technique to pick up reflections from physically observed ice boundaries and whether these boundaries occur at the same depths,
- To calculate the degree of change in physical properties and over how short a distance these changes produce seismic reflections, and
- (for AM03) to provide details for a re-evaluation of 2002/03 seismic data.

5.1 The survey sites

5.1.1 AM01

A short low-fold survey was carried out adjacent to the location of the AM01 borehole as it stood at December 2004. AM01 was originally drilled in mid-January 2002, and a repeat drill was carried out in mid-December 2003, named AM01b. The AM01 site moved downstream towards the ice shelf front, carrying the mooring equipment and data recording instruments left encased in the hole. It was at the December 2004 location of this migrated AM01 borehole that the seismic line was surveyed. The AM01 Line (as it shall be known) was aligned approximately N-S, approximately 50 m to the west of the AM01 2004 site. The relative location of these sites is shown in Figure 5.1.

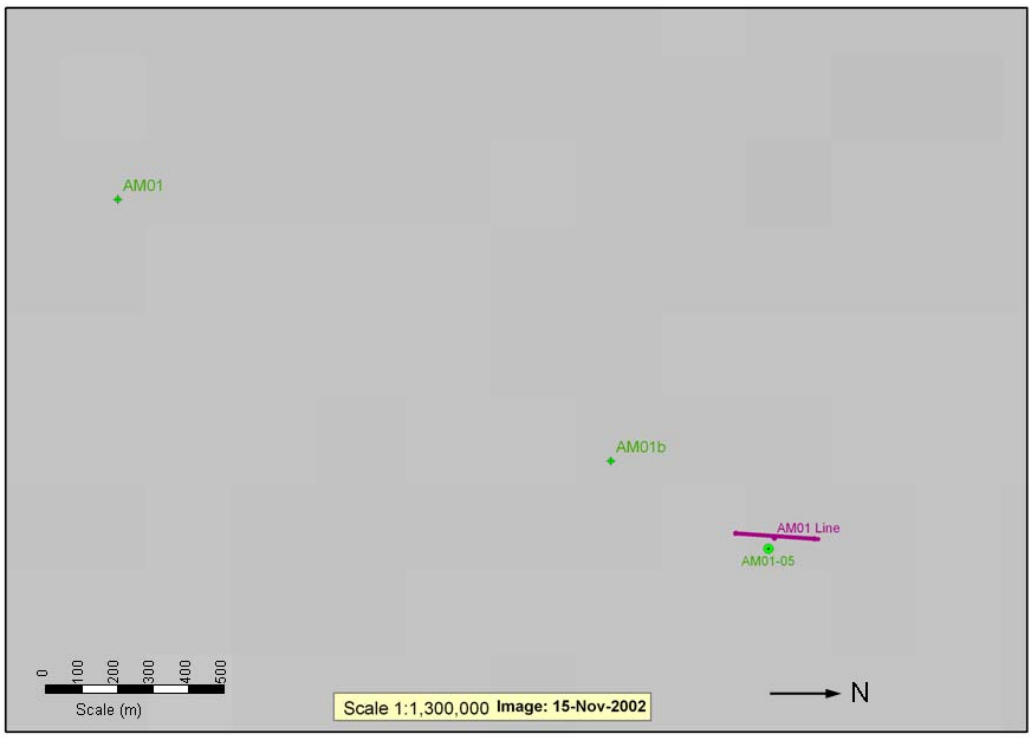

Figure 5.1 – Relative location of AM01, AM01b, the December 2004 location of the AM01 borehole, and the AM01 seismic Line.

5.1.2 AM04

AM04 is located approximately 70 km upstream of AM01 along the same flowline within the Eastern PCM Flow Unit (as shown in Figure 2.6). Two seismic lines were surveyed just south of the AM04 borehole location. The relative locations of these sites are shown in Figure 5.2.

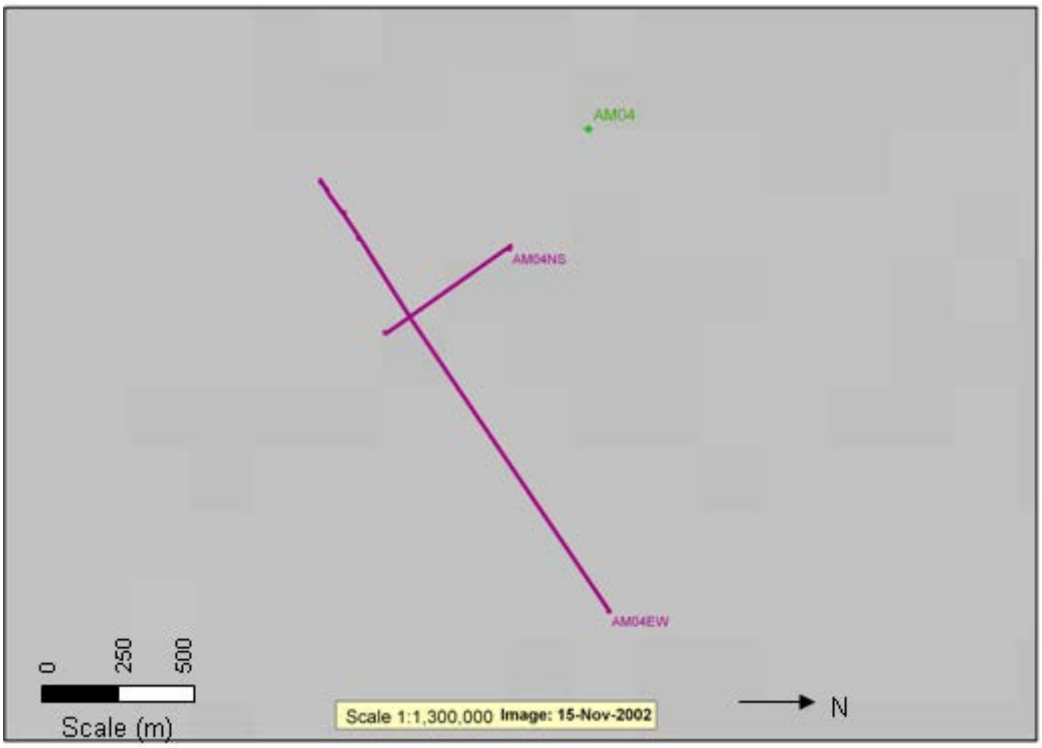

Figure 5.2 – AM04EW and AM04NS Lines in relation to the AM04 borehole location.

5.1.3 AM03

Refer to Figure 4.1 in Chapter 4 for relative locations of the seismic lines to the AM03 borehole.

5.2 Processing & results

5.2.1 Processing sequence

The seismic data were processed using Disco Focus software at Geoscience Australia. The processing sequence is similar to those outlined in Section 4.1.2 and 4.2.1 for the G2A seismic data.

AM04 Processing Steps

- Create input files for Disco Focus (seg2 to seg-y conversion and apply geometry via line, pattern, and source files)
- Combine seg-y files to create one Disco Focus seg-y file
- Spectral analysis to determine frequency content of the data
- Resampling data to 1 ms to reduce spatial aliasing (Tassell, 2004)
- Bandpass filtering
- Trace removal of noisy traces
- Front end muting to remove groundroll and refracted arrivals
- Surgical muting to remove deep hyperbolic noise
- Deconvolution (single trace predictive)
- CDP sorting
- Velocity analysis using an interactive velocity definition model (VELDEF). Velocities are picked and stored in the Disco Focus database to be applied in the NMO correction. Moveout velocities were selected for each reflection.
- Pre-stack NMO correction applied
- Stacking
- Runmix on 3 traces with weight 1, 2, 1
-

AM01 Processing Steps

- Create input files for Disco Focus (seg2 to seg-y conversion and apply geometry via line, pattern, and source files)
- Combine seg-y files to create one Disco Focus seg-y file
- Spectral analysis to determine frequency content of the data
- Resampling data to 1 ms to reduce spatial aliasing (Tassell, 2004)
- Notch filter (70 Hz) – to remove the noise introduced by the existing AM01 downhole equipment, due to the proximity of the survey to the borehole site.
- Bandpass filtering
- Front end muting to remove groundroll and refracted arrivals
- Surgical muting to remove deep hyperbolic noise
- Deconvolution (single trace predictive)

- CDP sorting
- Velocity analysis using an interactive velocity definition model (VELDEF). Velocities are picked and stored in the Disco Focus database to be applied in the NMO correction. Moveout velocities were selected for each reflection.
- Pre-stack NMO correction applied
- Stacking
- Runmix on 3 traces with weight 1, 2, 1

5.2.2 Seismic CDP profiles

The AM01 seismic profile is shown in Figure 5.3. The final CDP profile and interpreted sections of the AM04EW Line are shown in Figure 5.4. Figures 5.5 and 5.6 respectively display the final CDP profile and the interpreted CDP profile for AM04NS. The seismic profiles for G2A0203 and G2A0506 are displayed in Figures 4.3 and 4.5.

Both AM01 and AM04 presented problems for interpretation and modelling. As recognised in the field while collecting data, a basal ice reflection and a reflection from the boundary between meteoric and marine ice was difficult to view. These sites were expected to display a marine ice layer, from modelling of the marine ice under the AIS (Fricker et al., 2001), and from previous AMISOR drilling data. Larger explosive charges were used for the shots for these surveys, but this did not completely resolve the issue. The reduced thickness of the ice layers in these locations (being closer to the ice shelf front) also increased the difficulty in seeing these ice reflections in the stacked seismic data. Since front end muting removes refraction arrivals to an approximate maximum time of 400 ms and the ice reflections were occurring before this time, this reduced the fold coverage on the ice reflections.

Figures 5.3-5.6 display a best evaluation of reflections as seen in the data. AM01 (Figure 5.3), although a relatively short-length low-fold survey, shows the marine-meteoric ice boundary (MIP) at 150 ms, but only in the south end of the profile. The base of the ice shelf (IP) occurs at 203 ms, only at the north end of the survey. The seafloor depth here decreases from 807 ms to 820 ms (south-north).

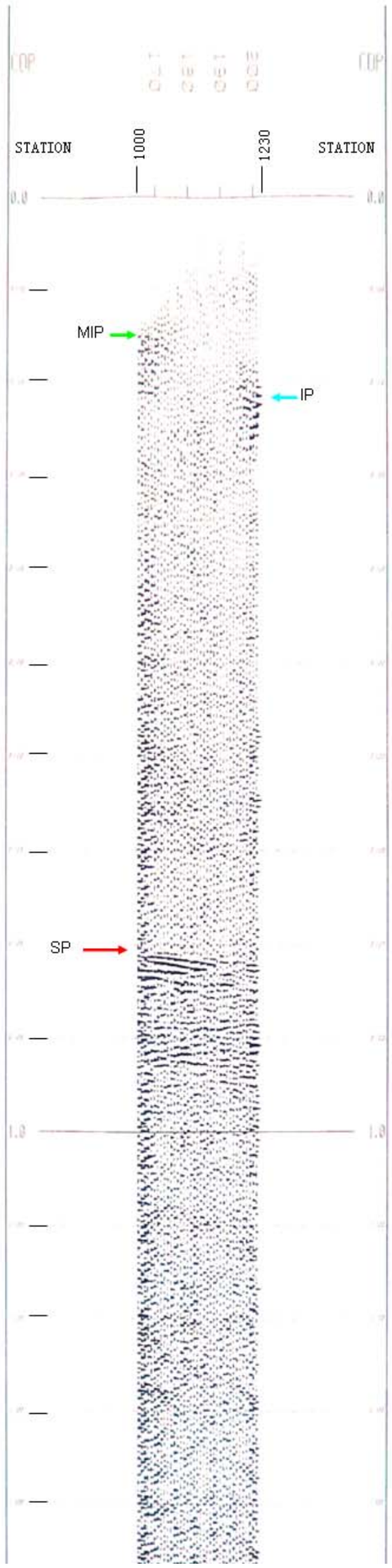

Figure 5.3 – AM01 CDP profile: Station location vs two-way time (s). Reflections: MIP = Meteoric-marine Ice primary, IP = Ice Primary (base of ice shelf); SP = Seafloor primary.

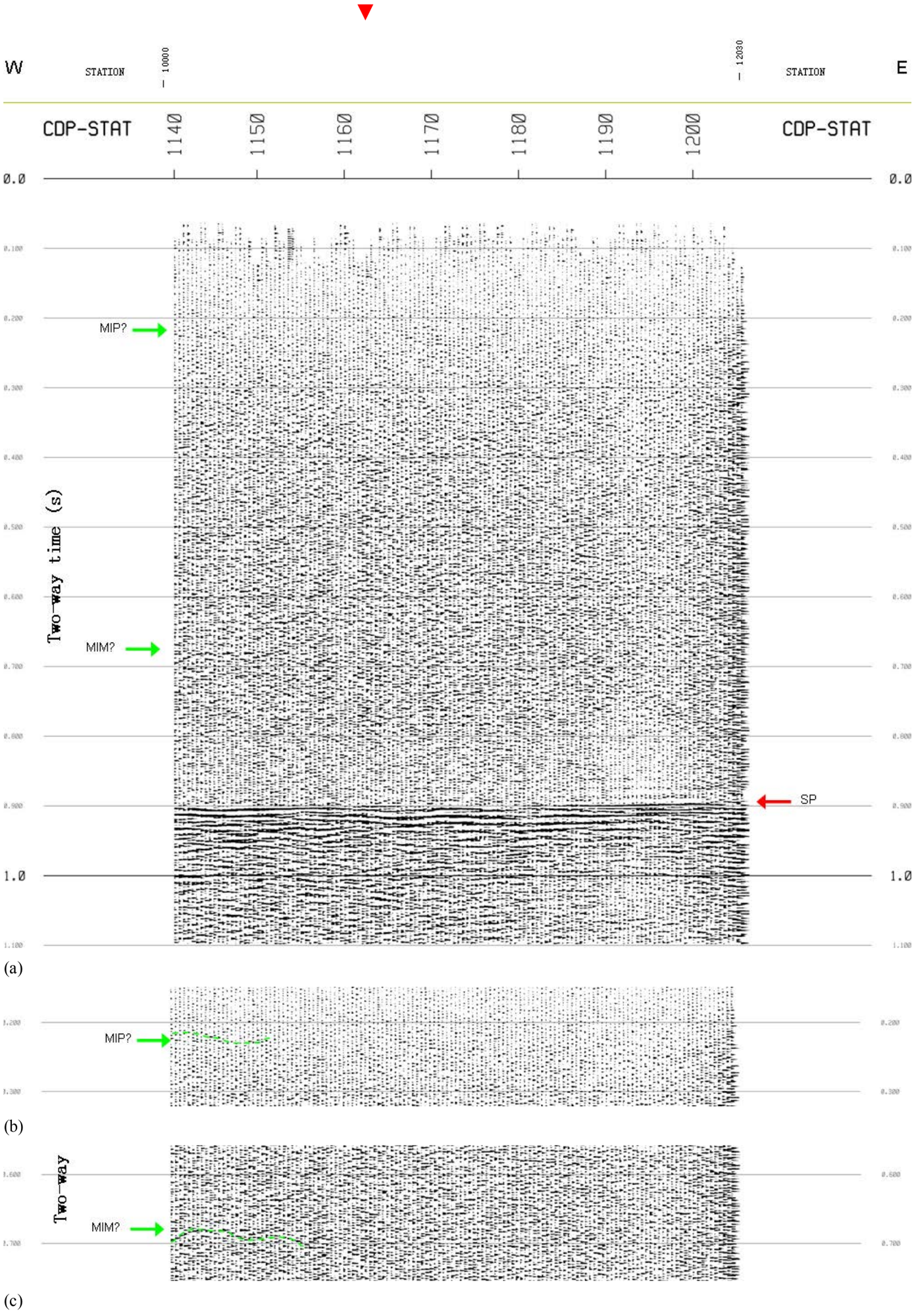

Figure.5.4 – (a) Full AM04EW CDP profile: Reflections: MIP? = Possible Meteoric-marine ice primary; MIM? = Possible meteoric-marine ice multiple (second multiple); SP = Seafloor primary. (b) Possible interpretation of MIP? reflection. (c) (b) Possible interpretation of MIM? reflection. Intersection point with AM04NS indicated by ▼

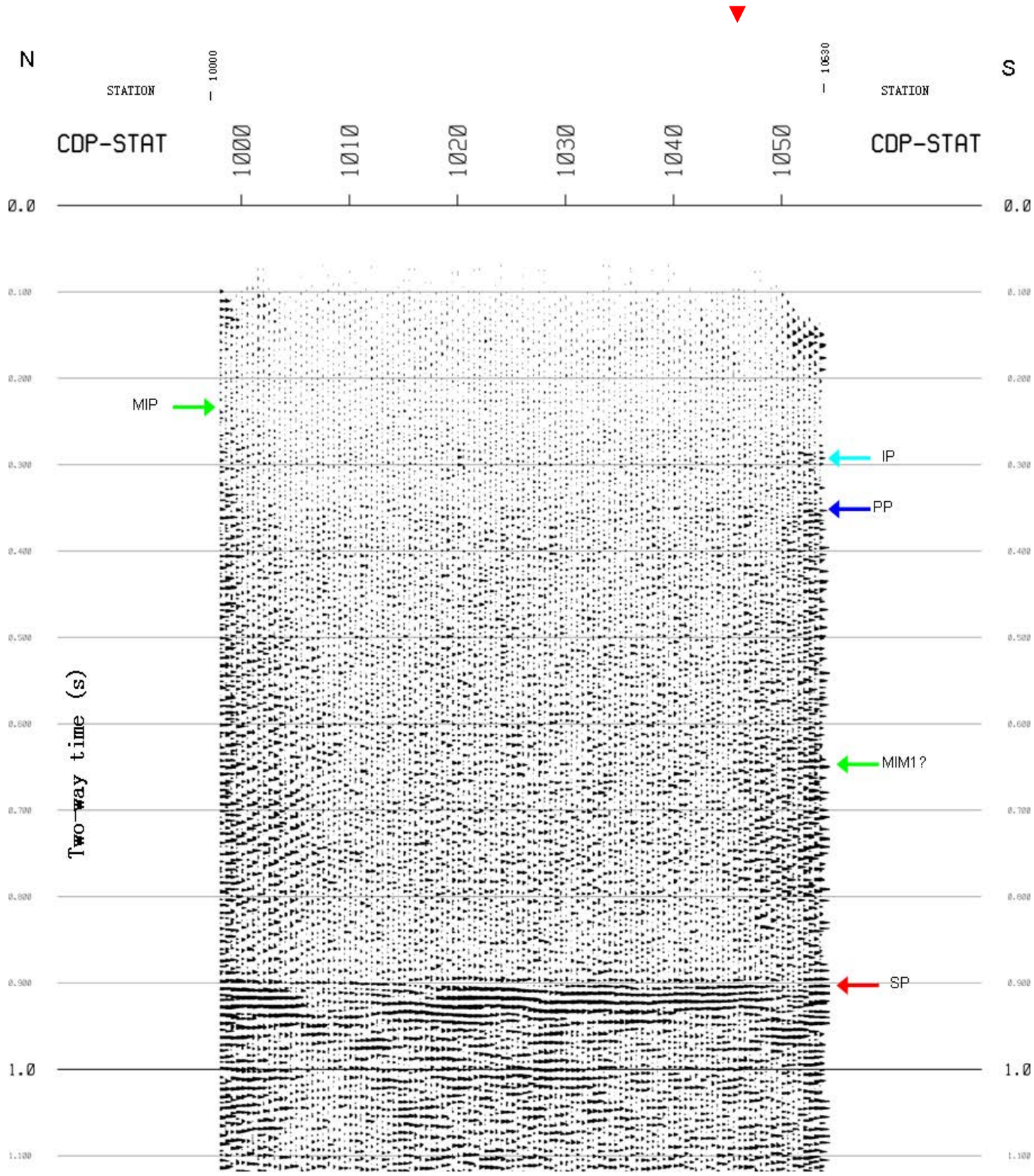

Figure 5.5 – AM04NS CDP profile: Reflections: MIP = Meteoric-marine ice primary, with reflection highlighted; IP = Ice primary (base of ice shelf); PP= pycnocline; MIM1? = Possible meteoric-marine ice multiple; SP = Seafloor primary. Intersection point with AM04EW indicated by ▼

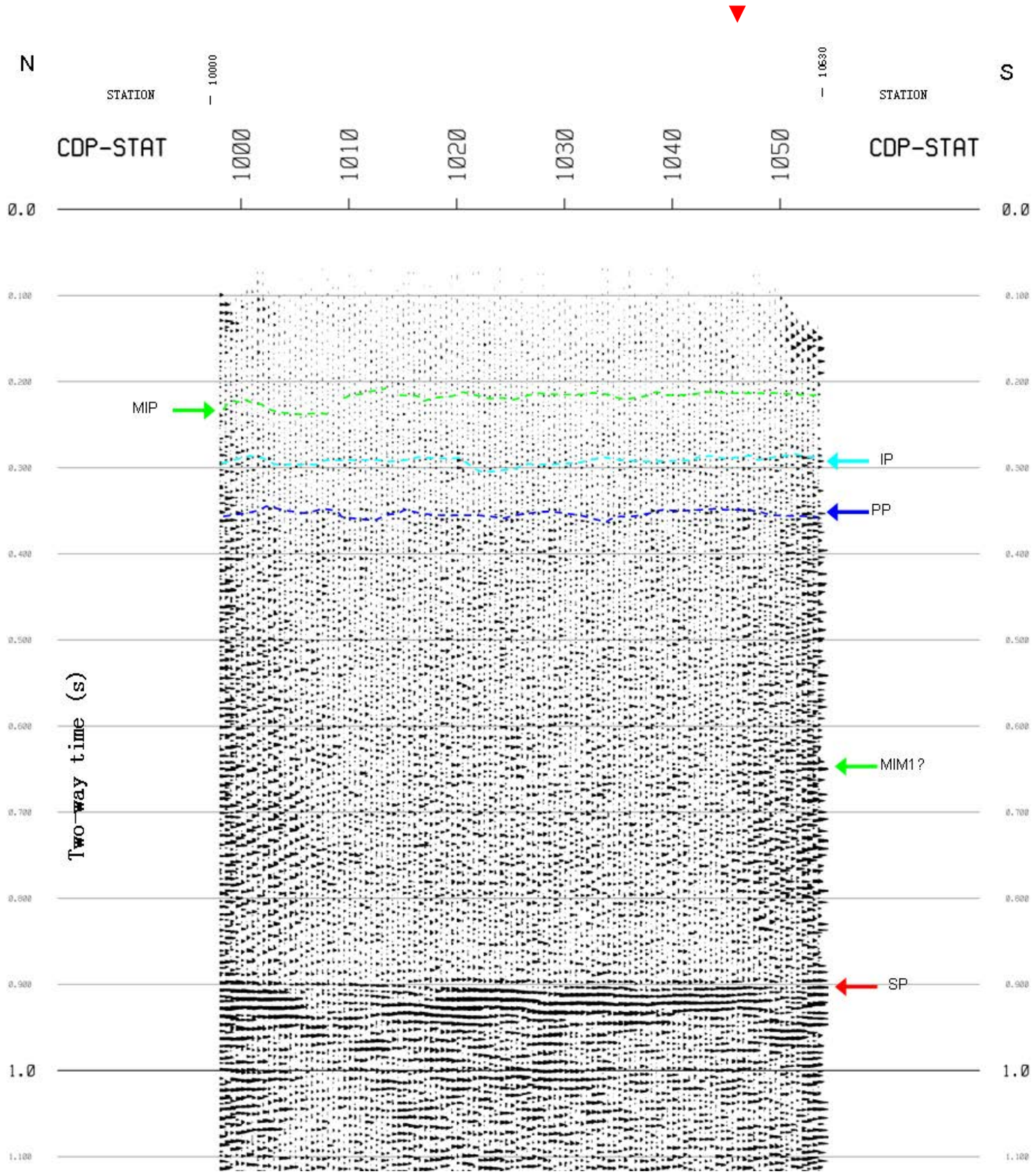

Figure 5.6 – AM04NS CDP profile including reflection possible interpretations.: Reflections: MIP = Meteoric-marine ice primary, with reflection highlighted; IP = Ice primary (base of ice shelf); PP= pycnocline; MIM1? = Possible meteoric-marine ice multiple; SP = Seafloor primary. Intersection point with AM04EW indicated by ▼

AM04EW (Figure 5.5) displays the seafloor well, showing the reflection to be horizontal at 906-897 ms. The ice reflections, however, are difficult to discern. There is a possible reflection that could relate to the MIP in the west end of the survey, at ~213-228 ms, but it does not continue throughout the profile. There is also a possible multiple arising from this primary at ~697-706 ms, although it is not the first multiple.

AM04NS (Figure 5.6) displays a MIP reflection at 237-213 ms in the north (left) and 217 ms in the south (right); an estimation of where the MIP reflection can be traced across the CDP profile is displayed on the profile. The IP reflection varies from 288-305 ms, but it is generally around 288 ms. A PP reflection also displays similarly - faint, varying in depth and non-horizontal - occurring at ~362-343 ms in the north and 351 ms in the south. The difficulty in tracing these reflections greatly increases the error in the arrival times and any depths calculated from them. The error in time could be up to ±10 ms, which would correspond to a depth error of ±18.5 m. The seafloor is horizontal at 893-897 ms.

These two profiles intersect at Station 10630 for AM04EW (1157 in Figure 5.5) and Station 10470 for AM04NS (1047 in Figure 5.6). Unfortunately the lack of ice reflections in AM04EW means that limited comparison can be made between these lines, however, the seafloor does occur at the same time of 901 ms.

Depths and depth errors have been calculated from these arrival times, and are listed in Table 5.1 and Table 5.2. The AMISOR drill depths have been included in Table 5.1. Comparing drill depths to seismic data, AM01 seismic results give a depth for the meteoric-marine ice boundary well within error of the AM01 drill depth. The reflection for the base of the ice shelf gives a depth ~100 m less than that measured at AM01. The seafloor seismic depth is 18-24 m less than the AM01 depth. If we take the ice base depth measured at AM01 and convert that depth to time, that would give an arrival time of 258 ms. Calculating for depth using this arrival time with the seafloor reflection time would give a seafloor depth of 878-887 m. This also is not within error. The site of the seismic line was however located a few kilometres downstream of where the AM01 borehole was drilled and measured in 2002. The rate of basal melt and thinning over this distance

Table 5.1 - Table of Ice (Base of Meteoric and base of Marine ice) & Seafloor Depths: including measured ice depths at AM01 and AM04, calculated depths for AM01 and AM04 seismic lines using measured reflection times and the ice and water velocities calculated from G2A seismic and AM03 data. Annotations: A and B: Seafloor depths for 893 ms (AM04NS) that correspond to A and B total ice thicknesses. AM04EW had no ice shelf base reflection time to be used for calculating seafloor depth. The predominant depth of the AM04NS IP times were used, 288 ms, and a travel time calculated from that depth, so that a seafloor depth could be estimated.

AMISOR Depths (m)		**AM01 Line**				**AM04EW**				**AM04NS**			
		South end of line		North end of line		West end of line		East end of line		South end of line		North end of line	
AM04	**AM01**	time (ms)	Depth (m)	time (ms)	Depth (m)	time (ms)	Depth (m)	time (ms)	Depth (m)	time (ms)	Depth (m)	time (ms)	Depth (m)
Base of Meteoric ice (P-wave velocity of ice 3700 ms^{-1})													
396	276	150	277.7	150	277.7	213	394.4	?		217	401.8	213	394.4
						228	422.1	?				237	438.8
Base of Ice Shelf (= Base of Marine Ice) (P-wave velocity of ice 3700 ms^{-1})													
603	479	203	375.9	203	375.9	***288***	***543.7***	***288***	***543.7***	288	533.2	A 288	533.2
												B 305	564.7
Seafloor (P-wave velocity of sea water 1452 ms^{-1})													
1002	841	807	814.4	820	823.8	906	992.4	897	985.9	897	975.4	A 893	972.5
												B 893	991.6

Table 5.2 – Error values for AM01 and AM04 seismic times and depths. Since the AM04EW seafloor depth was calculated from AM04NS ice shelf base depths, its higher error has been introduced to AM04EW's seafloor depth.

			Errors	
Line	**Reflection**	**P-wave velocity (ms^{-1})**	Time (± ms)	Depth (± m)
AM01	Ice	3703	2	3.7
	Seafloor	1452	2	5.1
AM04EW	Ice (MIP)	3703	4	7.4
	Seafloor	1452	2	20
AM04NS	Ice	3703	10	18.5
	Seafloor	1452	2	20

would still not account for such a difference in ice thickness, although Craven et al. (2009) describe that their depth results at AM01 in 2002/2003 were gained from an approximation using a video system (due to instrument failure) and that this value was confirmed by the CHINARE ice core taken a few hundred metres from AM01 that returned a 296 m ice core. If a 20 m change in thickness over a few hundred metres is considered good correlation, then perhaps a larger difference such as that measured from the seismic data is acceptable over the larger distance between the 2002 AM01 drillsite and the AM01 seismic line.

The depth results for AM04 seismic lines compared to the AM04 drill depths show a good correlation for the meteoric-marine ice depth. All the minimum seismic depths for this boundary are within error of the measured drill depth. The seismic profile does show that this boundary may be more irregular than horizontal, with variances on the scale of tens of metres. This may be due to uneven basal melting or non-uniform accretion of marine ice. The accuracy of the seismic depth for the base of the ice shelf is again dissimilar to the AM04 drill depth. The seismic reflection has put the ice base at a depth up to ~70-80 m less than at AM04. Even if we assume the greatest variance in error in favour of correlating the values, the seismic depth is still ~50 m less than that of AM04. The seafloor is ~10-16 m shallower at AM04EW, and 10-27 m shallower at AM04NS than the AM04 seafloor depth, although this is mostly within error of AM04's depth. The seafloor depth of AM04EW is based on assumptions due to the reflection at the ice base being too difficult to pick out of the seismic data. However, AM04EW does

intersect the AM04NS line in the middle of AM04EW at the south end of AM04NS. These values here are similar, yet it must be remembered that the depth at AM04EW was calculated using ice base depths/times from AM04NS, so that may account for the small difference. Both AM04EW and AM04NS do show meteoric-marine reflections and seafloor reflections very close to the same time, so the results are not invalidated by this.

5.2.3 AMISOR CTD data

AMISOR collected seven CTD casts at AM01 in January 2002. CTD Cast 6 was chosen to represent the data from this location. Plots of conductivity and temperature against depth below the surface of the ice shelf (calculated from Appendix 1.3 of the AM01 report (Rosenberg, 2002)) are shown in Figures 5.7 and 5.8, respectively.

One CTD cast was carried out at AM04, on the 9th of January 2006. Plots of AM04 conductivity and temperature versus depth below ice surface (Rosenberg, 2002) are shown in Figures 5.9 and 5.10.

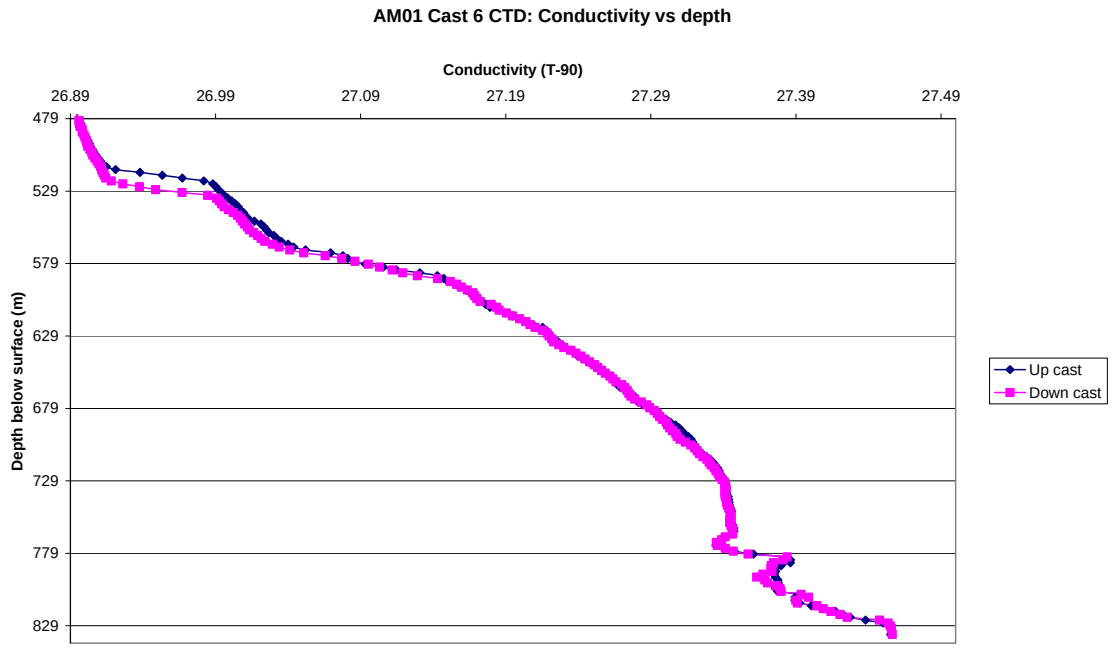

Figure 5.7 – AM01 Cast 6 up- and down-cast CTD conductivity profile between ice shelf base and seafloor

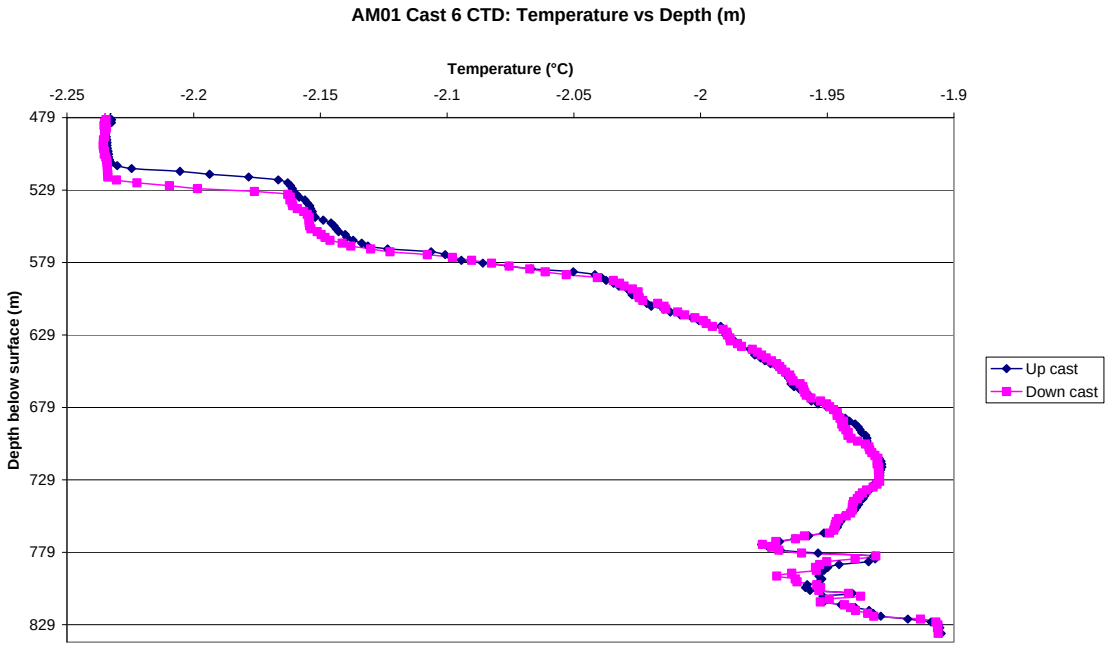

Figure 5.8 - AM01 Cast 6 up- and down-cast CTD temperature profile between ice shelf base and seafloor

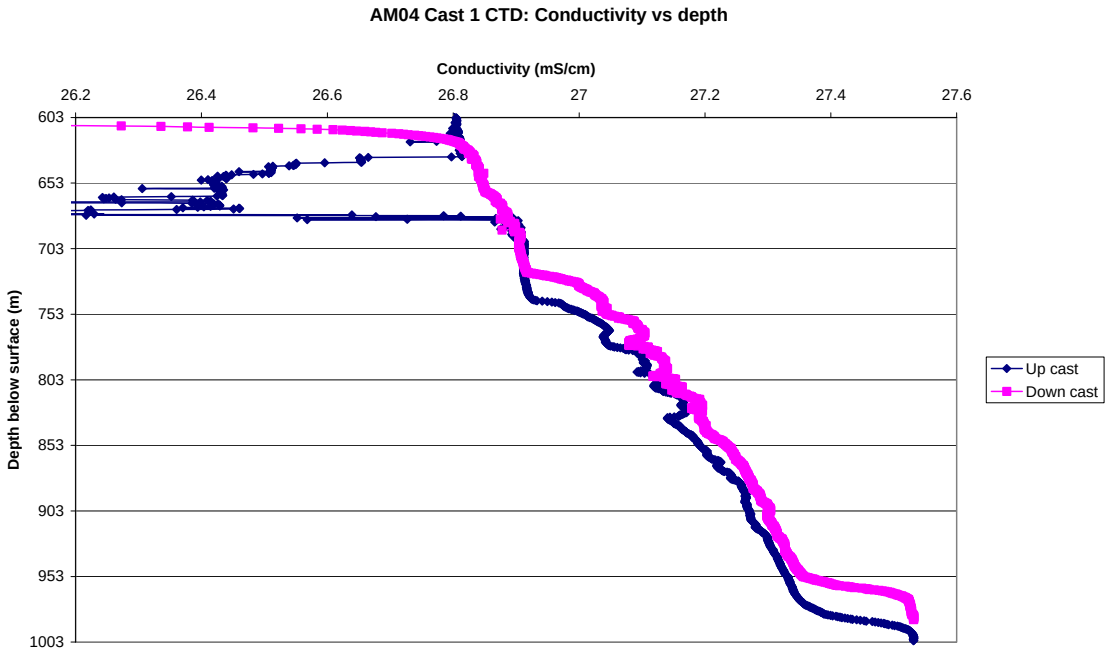

Figure 5.9 - AM04 Cast 1 up- and down-cast CTD conductivity profile between ice shelf base and seafloor

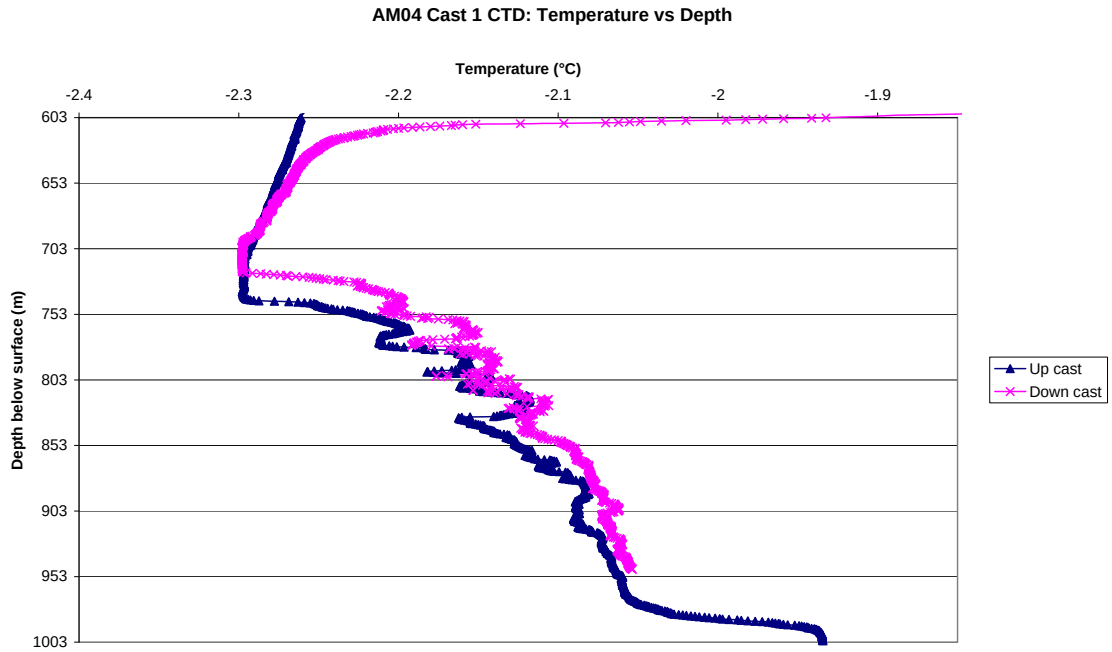

Figure 5.10 - AM04 Cast 1 up- and down-cast CTD temperature profile between ice shelf base and seafloor

In the AM01 CTD data, there is a significant change in gradient at the same depths for both conductivity and temperature. These depths are 773, 783, and 795 m, and are likely candidates to produce a seismic reflection. The rate of increase over 520-531 m would also likely result in reflections, near to the base of the ice shelf.

AM04 CTD Cast 1 displays a profile with varying gradients through the water column; there is not a smooth increase in either conductivity or temperature through the water column. The up-cast for conductivity is particularly erratic in the 80 m below the base of the ice shelf. Taking the depth values from the up-cast for temperature, there are changes in gradient at approximately 735, 773, 796, 831, 914, and 971 m. In general, the AM04 water property profiles could be divided into three layers: 603 (base of ice) to 738 m, 738-971 m and 971 m to the seafloor.

Images of the AM01 and AM04 seismic profiles beside CTD casts from the AMISOR drillholes are shown in Figure 5.11 and 5.12, respectively. Most of the major sharp gradient changes in the AM01 CTD data do not correspond overly well with any feature in the seismic data, with the exception of one at 611 m.

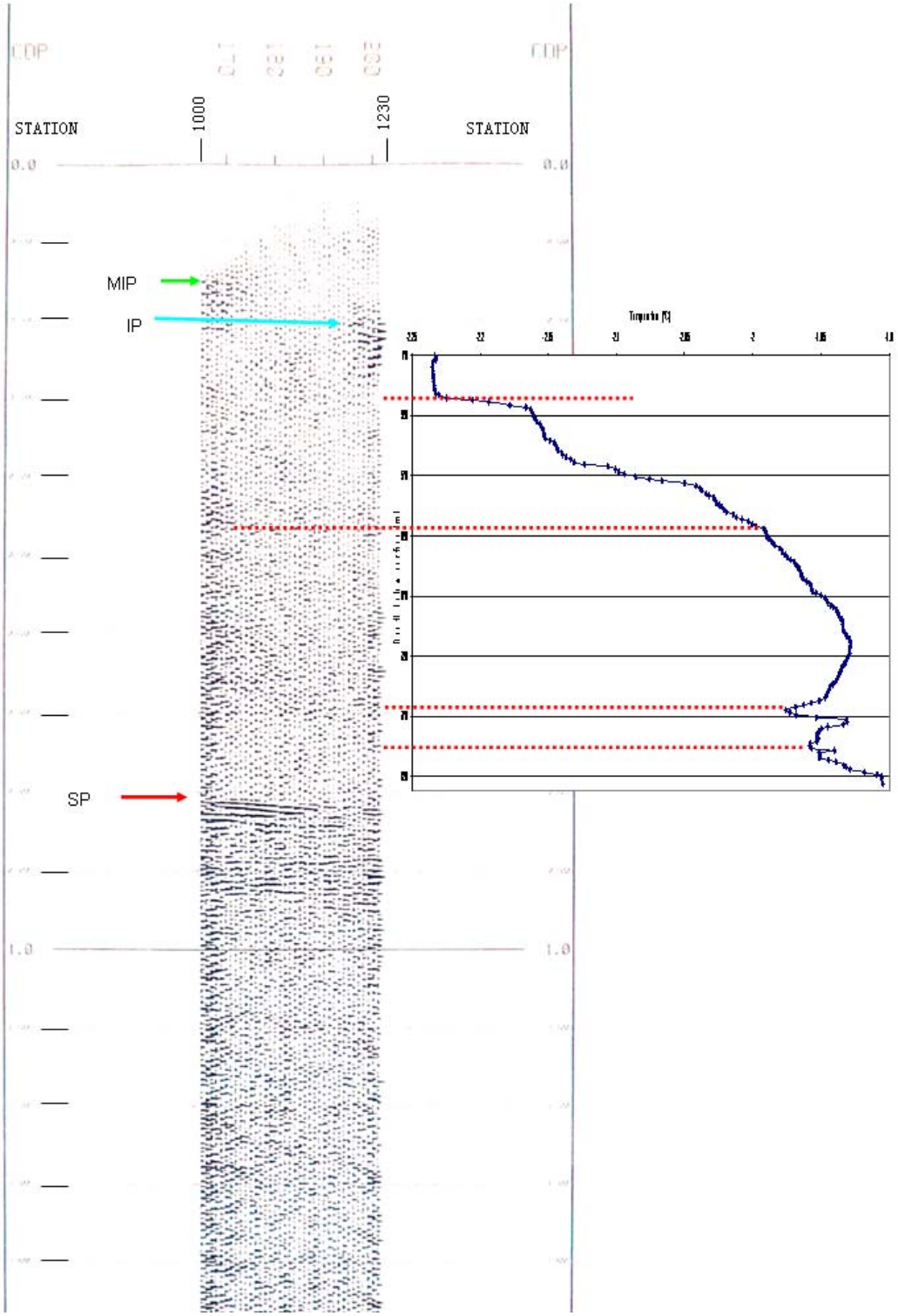

Figure 5.11 – AM01 CDP profile compared to gradient changes in AM01 CTD temperature up-cast profile (red dashed lines indicate possible correlations).

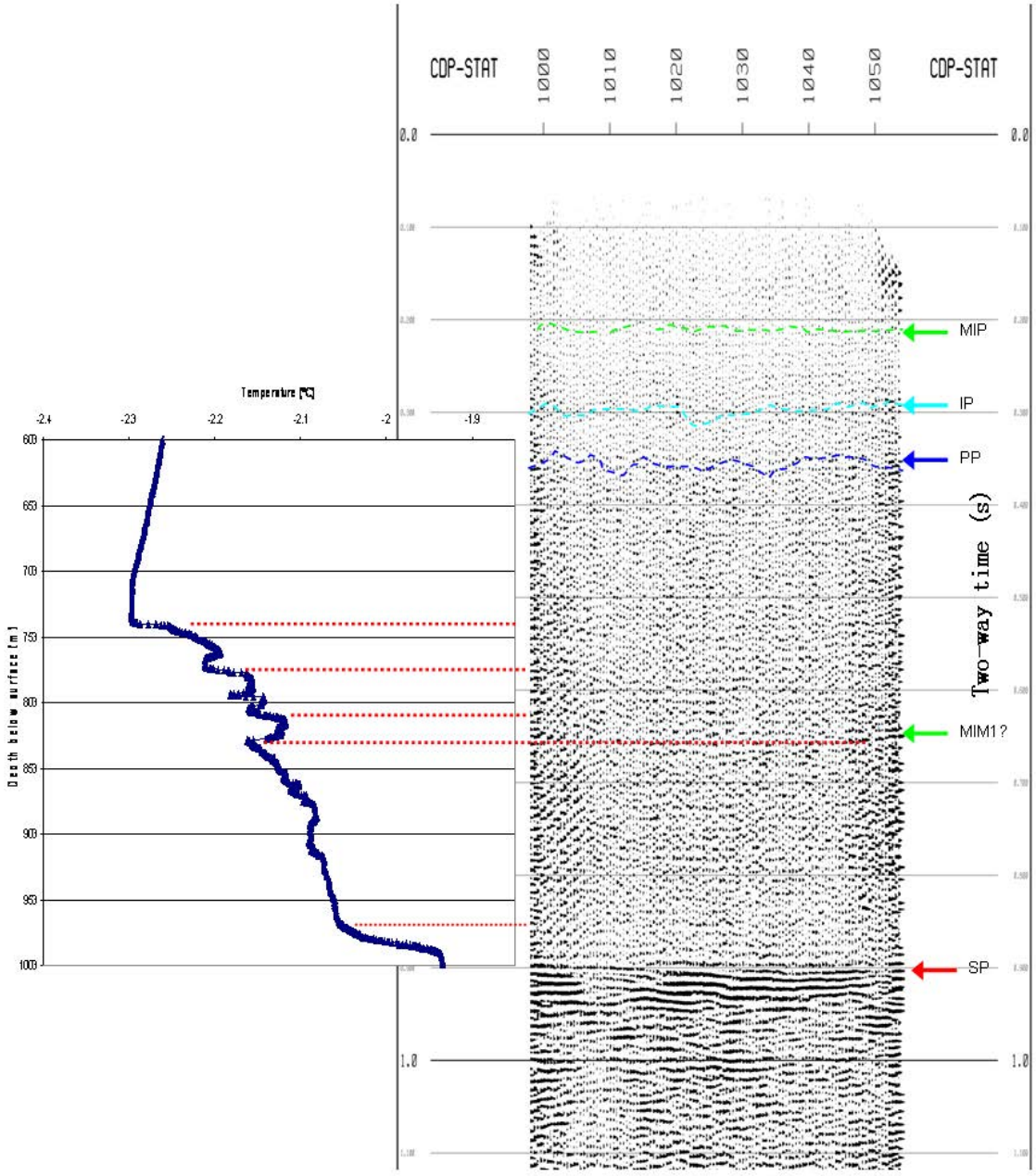

Figure 5.12 - AM04NS CDP profile compared to gradient changes in AM04 CTD temperature up-cast profile (red dashed lines indicate possible correlations).

The seismic and CTD data at AM04 is not so well correlated either, with only one temperature change aligning with the reflection labelled MIM1. Craven et al. (2009) have described the oceanographic data from the AM04 site as showing strong seasonality. This may explain both the variant nature of the CTD profiles and possibly why they still do not correlate well with the seismic data.

5.3 Discussion

The most apparent difference between the AM01 and AM04 seismic data and the G2A0203 and G2A0506 seismic data is the comparative lack of reflections or strong reflections in the AM01/AM04 data, especially with regards to ice and water reflections. Differences are to be expected, considering G2A and AM01/AM04 are situated in different environments in term of the ice shelf-ocean dynamics of the AIS.

AMISOR site AM01 is 70 km directly downstream from AMISOR site AM04 within the Eastern PCMs Flow Unit (as outlined in Figure 2.6 and 3.1). AM01 is ~100 km from the ice shelf front, and AM04 ~170 km. G2A on the other hand, is located in the Lambert Glacier Flow Unit, near to the western margin bounding Mellor Glacier Flow Unit. G2A/AM03 is located approximately 250 km from the ice shelf front near the Loose Tooth, or ~210 km to where the Lambert Unit reaches in the ice shelf front. The greater distance from the ice shelf front means that the ice at G2A/AM03 is thicker and that the seafloor is deeper (see Figure 2.26 for a cross section of the AIS displaying this).

The ocean circulation under the AIS is a controlling factor in the distribution of melt and accumulation of ice at the base of the AIS. Figure 5.13 displays the marine ice distribution under the AIS (Fricker et al., 2001) with the major ocean circulation pattern as described by Hemer & Harris (2003) annotated upon it. Within this pattern, G2A/AM03 are situated neither completely within an area of inflow or outflow, and according to Fricker et al's (2001) map they are in an area of negligible accumulation. This has been supported by the findings of this thesis, and by the AMISOR project (Rosenberg, 2006; pers. Comm., M. Craven, 2006). AMISOR drilling at AM01 and AM04 found the ice basal zone to be within the adjacent region of basal accumulation and circulation outflow (Craven et al., 2009; Treverrow et al., 2010). As such the ice properties vary greatly between these two regions.

As was concluded in Chapter 4 of this thesis, G2A is an area of meteoric ice with sub-ice shelf layers of super-cooled water with a sharp change in water properties within 30-

40 m, perhaps with frazil ice. AM01 and AM04 are within an area of marine ice accretion (Craven et al., 2009; Fricker et al., 2001), and as such the environment at the

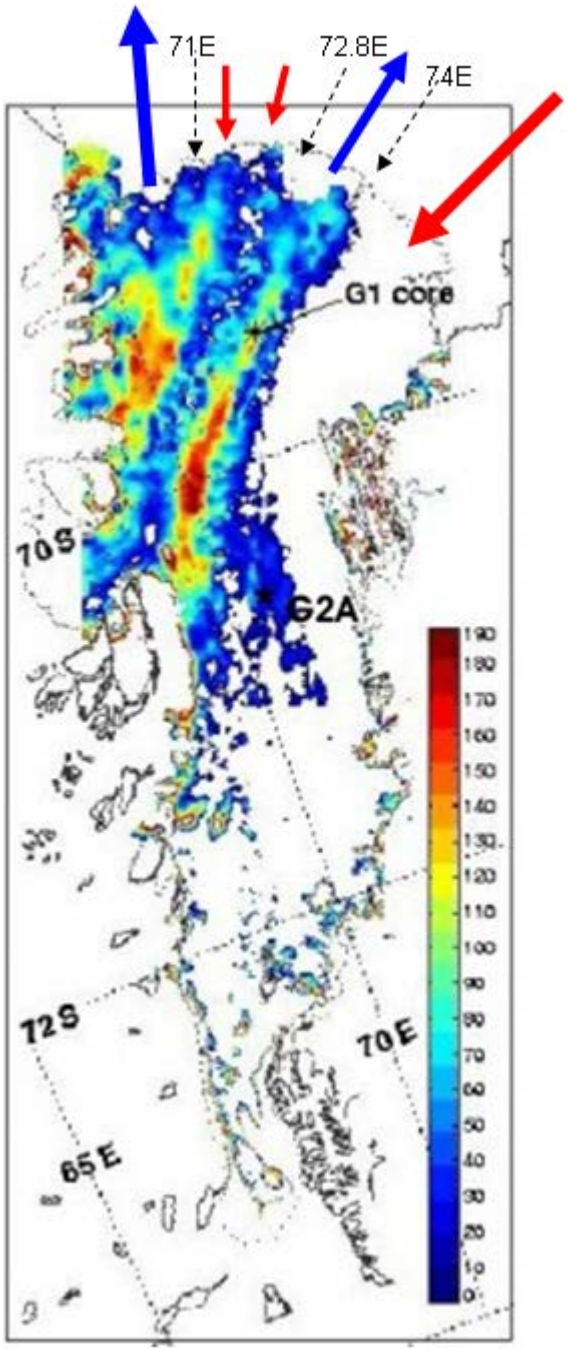

Figure 5.13 – Marine ice distribution under the AIS mapped with diagrammatic indication of the ocean circulation pattern entering and leaving the AIS. Arrows: red indicates warmer Prydz Bay water entering the ice shelf cavity, blue indicates cooled water exiting the ice shelf cavity (the size of the arrows indicates and approximate relative size of water flow.), and black indicates longitude at the ice shelf front (Adapted from (Allison, 2003; Hemer & Harris, 2003)).

base of the ice shelf is quite different. AMISOR have described the presence of a "porous ice/slush layer below the solid ice shelf" (Rosenberg, 2002) since drilling at AM01 in 2001/2002. It was discovered that marine ice had a honeycomb structure (Craven et al., 2007; Craven & others, 2005), where frazil ice formed platelets and with accretion became first porous ice, then bubbly ice when the pores closed due to increasing pressure. These bubbles preserve saline water and debris within the ice, making this ice markedly different to meteoric ice (Eicken et al., 1994; Moore et al., 1994). Refer to Figure 2.21 for an image of the brine inclusions present in marine ice (and for more information refer to Section 2.5.5 and 2.5.6).

In terms of what this marine ice structure means to seismic reflections, let us consider three aspects of the data results:

- ❄ All the seismic lines (AM01, AM04EW and AM04NS) display a reflection that correlates well with the AMISOR measured depth for the boundary between meteoric and marine ice.
- ❄ All the seismic lines show a reflection at a height above the ice shelf base depth measured by AMISOR.
- ❄ All the seismic lines do not display a reflection at the ice shelf base depth measured by AMISOR.

The transition between meteoric and marine ice on the AIS has been discussed by Craven et al. (2005); stating that the transition viewed at AM01b was not a defined sharp boundary (see Figure 5.14), and it was also not strictly horizontal. Craven et al. (2005) describes the boundary as undulating, implying some meso-scale structure to the ice shelf base upstream where the marine ice first began to accrete. The fine structure may be due to the scalloped nature of the original meteoric ice shelf base, as has been seen in overturned icebergs that had begun to accrete frazil ice (Craven & others, 2005).

The transition is clearly visible to the naked eye as displayed in Figure 5.14, and the image shows a defined change in crystal structure. This change has now been shown to be just enough to produce a weak reflection in seismic data.

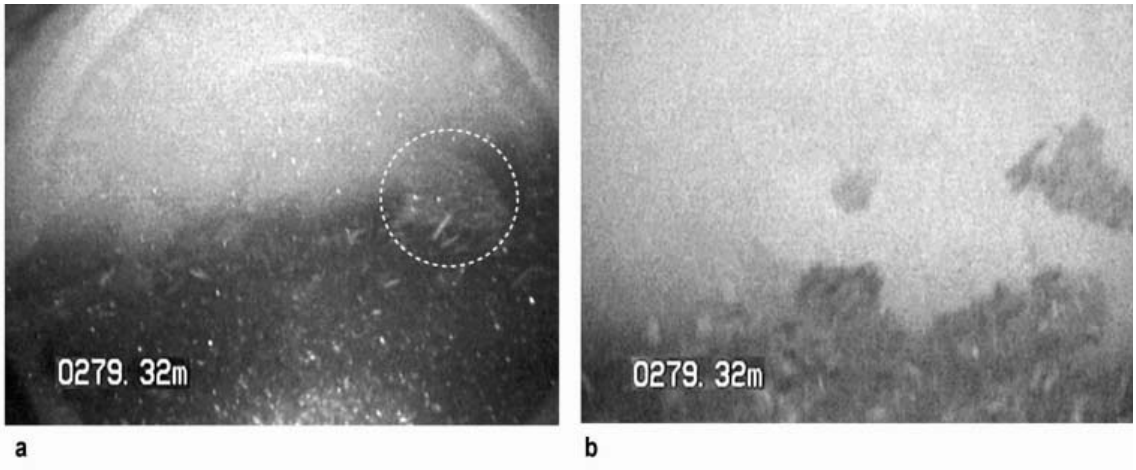

Figure 5.14 - Side-looking images at the meteoric–marine ice transition depth. (a) Tiny platelet crystals (2–5mm across) appear in the dark marine ice immediately below the transition, and a much larger meteoric ice crystal grain projects into the marine ice across the interface (circled). (Note camera lens reflection near top corners of the image.) (b) The two dark patches (centre and middle-right) may be marine ice inclusions within the meteoric ice crystal matrix. (Craven & others, 2005, Fig 4)

In regards to the second and third point about seismic data and marine ice reflections, there is another plausible explanation for the difference in AMISOR depths and seismic-measured values for the base of the ice shelf. Referring back to Figure 2.24 in Chapter 2 - the hydraulic connection depth measured by AMISOR at AM04 was ~530 m and 376 m at AM01. Below this depth the ice is consolidated, but permeable (Craven et al., 2009). The "IP" reflection depth measured on the AM01 Line is 375.9 m, at exactly the same depth as the AM01 borehole. Along the AM04NS Line, the IP reflection varied somewhat but was generally stable around 288 ms. The depth calculated from this value is 533.2 m. Again this is remarkably accurate for the hydraulic connection depth given for AM04.

Video taken down the boreholes by AMISOR at these locations showed that in the bottom 40-50 m of the ice shelf the ice texture had a layered, flaky appearance (Craven et al., 2009) (see Figure 5.15). These ice platelets could be randomly oriented and are filled with seawater-filled connected pores, permeable to the ocean cavity below the ice.

They were described as interconnected cells with channels, akin to firn ice. Craven et al. (2009) state that this permeable layer still retained structural integrity, and was unlike the unconsolidated slush seen elsewhere and under other ice shelves such as the Ronne. However the random orientation of platelet crystals and the large volume of interstitial freely flowing sea water in this type of marine ice could result in no seismic reflected waves at this location. The nature of the connection with the water column in this zone may mean there is an insufficient difference in physical properties over this boundary (or that the properties of the water swamp any measurement of the ice properties, or the ice properties of newly formed marine ice *are* exactly the same as the water they freeze in) to be able to produce a seismic reflection here. In terms of physical measurement by drilling, this layer displays enough consolidation and integrity to be classified as accreted marine ice rather than frazil ice. However, to the seismic technique, this layer appears no different to sea water and the "ice base" boundary is instead measured where the marine ice loses hydraulic connection with the ocean cavity.

From comparison with AMISOR CTD and drill data, we now understand much more about the seismic response at meteoric ice-water interfaces and marine ice-water interfaces.

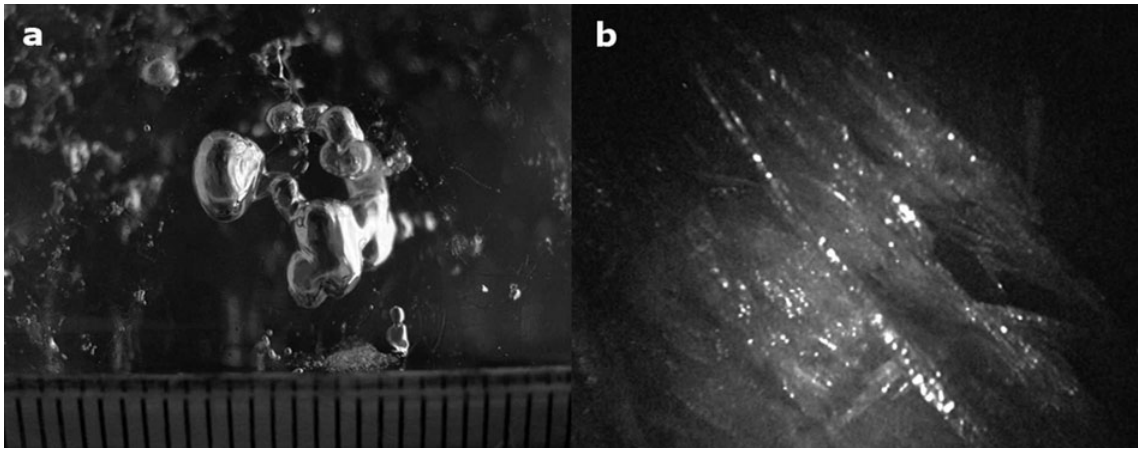

Figure 5.15 - (a) Marine ice sample from 450m depth at AM04 with millimetre size cells (scale with mm gradations across bottom), possibly containing trapped brine. (b) Video image from near the base of the shelf showing thin platelets stacked together, seen largely edge-on. Whilst the exact scale is uncertain, the platelets are probably 10mm or more in diameter. (Craven et al., 2009)

Chapter 6

PYNOCLINES IN THE WATER COLUMN BENEATH THE AIS

> *"Characterising the temperature and density fine structure of the ocean is important for understanding numerous ocean processes, including internal waves, mixing, and thermohaline circulation." (Páramo & Holbrook, 2005, p.1)*

6.1 A brief introduction to the study of oceanography for Prydz Bay and the AIS

For reference throughout this chapter, the following two thesis chapter sections outline the theories and define the terms that are of relevance to this topic.

6.1.1 Oceanographic terms

A **pycnocline** is defined as a layer across which there is a relatively rapid change in water density with depth (Dictionary of Earth Science 2003). In freshwater environments this density change is primarily caused by a change in water temperature. In the open ocean and ice shelf environments where seawater is present, the density change may be due to salinity and/or water temperature changes (Baum, 1997).

Similarly, a **halocline** is a strong, well-defined vertical salinity gradient in oceans and seas (Dictionary of Earth Science 2003; Baum, 1997). In polar regions such as the Southern Ocean where ocean surface waters are colder than deep waters, the halocline helps maintain water column stability – separating and isolating the surface waters from

the deep waters. It also allows for the formation of sea ice and helps to limit the amount of CO_2 that escapes to the atmosphere.

The **Thermocline** is a layer within a water-body or in the air where the temperature changes rapidly with depth. In the open ocean, the sun heats the surface layer, and wind and waves mix the water to produce a warm surface layer. Below that, the temperature drops rapidly, by as much as 20 ºC over 150 m change in depth – this area is the thermocline (Baum, 1997). Temperatures continue to decrease below the thermocline, but at a slower rate.

If referring to the joint activity of salinity and temperature in the oceans, the term **thermohaline** can be applied (Dictionary of Earth Science, 2003). **Thermohaline convection** is the vertical water movement observed when sea water, due to conditions of decreasing temperature or increasing salinity, becomes heavier than the water beneath it (Dictionary of Earth Science, 2003). The impact of this internal mixing upon the oceans include effects on sediment transport, biology (e.g. plankton moving in/out of photic zone), and the large-scale overturning circulation of the world's oceans (Zimmerman et al., 2005).

Waves are the periodic movements of interfaces (Zimmerman et al., 2005). If the water column consists of an upper layer and a denser lower layer, the interface between the layers can undergo wave motion. This motion, which does not affect the surface and is mostly not observable at the surface, is an example of an **internal wave** (Zimmerman et al., 2005). Another way of describing them is as gravity waves that oscillate within, rather than on the surface of, a fluid medium.

Internal waves arise from perturbations to hydrostatic equilibrium, where balance is maintained between the force of gravity and the buoyant restoring force. A simple example is a wave propagating on the interface between two fluids of different densities, such as oil and water. Internal waves typically have much lower frequencies and higher amplitudes than surface gravity waves because the density differences (and therefore the restoring forces) within a fluid are usually much smaller than the density of the fluid itself. They have periods ranging from 10–20 minutes to several hours, compared to surface gravity waves which have periods several seconds to minutes long

(Baum, 1997; Zimmerman et al., 2005). Internal wave motions are ubiquitous in both the ocean and atmosphere. Internal waves at tidal frequencies are produced by tidal flow over topography/bathymetry, and are known as **internal tides**. They manifest themselves in a periodic lifting and sinking of the seasonal and permanent thermocline at tidal rhythm, and are the most common internal waves (Zimmerman et al., 2005).

Waves can occur on the thermocline, causing the depth of the thermocline as measured at a single point to oscillate (usually as a form of seiche - an occasional and sudden oscillation of the water of a lake, bay, estuary, etc., producing fluctuations in the water level and caused by wind, earthquakes, changes in barometric pressure, etc.). Alternatively the waves may be induced by flow over a raised bottom, producing a thermocline wave which does not change with time, but varies in depth as one moves into or against the flow.

In describing these attributes, surfaces of constant density of water are called **isopycnals**. Due to the action of winds and currents, isopycnals are not always level. Figure 6.1 displays a graph of isopycnals against temperature and salinity, showing the world's major oceans, including Antarctic bottom water.

In general, in polar ocean environments, temperature increases with depth, with cooler water sitting above warmer water – this is why ice freezes at the surface of water. Density increases with depth, and is modified by both temperature and salinity, as was displayed in Figures 4.6-4.7 in Chapter 4.

6.1.2 Ocean water bodies in polar regions

Based on differing temperatures, salinities and densities, the waters of the polar and circumpolar regions exist as discernable bodies of water. The area of Prydz Bay has been investigated by Nunes Vaz & Lennon (1996) and Yabuki et al. (2006), who has formed the following explanation of the ocean in Prydz Bay.

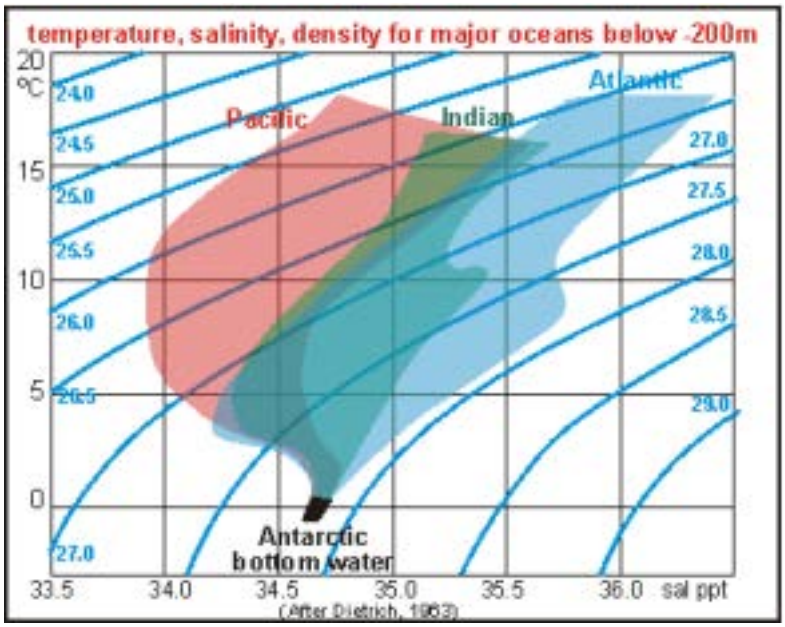

Figure 6.1 - The relationship between temperature, salinity and density is shown by the blue isopycnal (of same density) curves in this diagram. In red, green and blue the waters of the major oceans of the planet is shown for depths below -200 metre. The Pacific has most of the lightest water with densities below 26.0, whereas the Atlantic has most of the densest water between 27.5 and 28.0. Antarctic bottom water is indeed densest, although the Atlantic also has a lot of similarly dense water but at higher temperatures and salinities. (Anthoni, 2000; Dietrich, 1963)

Antarctic Bottom Water (AABW) is the cold, dense water that spreads over the abyssal layer of the world ocean. It is thought to have originated mainly in the Weddell Sea, until Jacobs & Georgi (1977) detected cold, high oxygen water near the bottom of the continental slope near 60°E., with flow to the east, and proposed that one of the sources of AABW came from the Enderby Land/Prydz Bay coast.

According to Yabuki et al. (2006), the hydrographic features in the Prydz Bay region are characterized by relatively warm (temperature $\theta > 0.5$°C) and salty (salinity $S > 34.65$) deep water, called **Circumpolar Deep Water** (CDW) which is distributed outside of Prydz Bay, with **Modified CDW** (MCDW) and cold shelf water, **Ice Shelf Water** (ISW) in the Amery Ice Shelf region (Nunes Vaz & Lennon, 1996).

MCDW is a mixture of low salinity shelf water and intruding CDW, and it is colder and less saline than unmodified CDW. One of the crucial processes of AABW formation is the mixing of MCDW with salty shelf water (Yabuki et al., 2006). The terms **Low Salinity Shelf Water** (LSSW) and **High Salinity Shelf Water** (HSSW) are used to describe water masses characterized in the shelf domain. In the Prydz Bay region, the shelf water has been classified as LSSW (Yabuki et al., 2006) using the definition of Whitworth et al. (1998), although the investigation of Nunes Vaz & Lennon (1996) in the Prydz Bay region revealed the existence of LSSW more saline than 34.6, which they called HSSW. Yabuki et al. (2006) instead calls this "saltier LSSW". When the salinity of the shelf water is over 34.6, the mixing process can make bottom water dense enough to descend the continental shelf slope, called Prydz Bay Bottom Water.

Nunes Vaz & Lennon (1996) and Yabuki et al. (2006) describe a cyclonic clockwise circulation in Prydz Bay, with the water inflow to the bay and clockwise circulation being dominant at 200-500 m depth. Yabuki et al. (2006) identified the water below 200 m as the MCDW; and explain MCDW provides salt for the shelf water and is the main source of the saltier LSSW, mostly by brine rejection associated with ice formation, both as sea ice and as basal accretion under the AIS.

The results of Yabuki et al. (2006) give the thickness of ISW near the front of the AIS to be up to 500 m, decreasing to 200 m by ~68°S, confirming internal cooling of water by the AIS. Higher saline water accumulates in the deeper waters under the AIS due to its higher density, leading to what Yabuki et al. (2006) call saltier LSSW. This water is at near-freezing temperatures and Yabuki et al. (2006) have shown that the bottom water in front of the AIS has a higher salinity than further out in Prydz Bay. In this process, the MCDW that is input into the bay circulation system is modified to saltier LSSW at depths greater than 500 m. Although it has not been directly shown to date, mixing between the saltier LSSW and the unmodified CDW near the continental slope would produce water with properties characteristic of AABW (Yabuki et al., 2006).

6.2 Case study: Camp Tropical

The case study survey for this chapter is the Camp Tropical CDP line (CT Line). The survey's purpose was to investigate whether the seismic technique could image any changes over a major boundary flow line within the AIS. The CT Line was surveyed perpendicular to ice flow in a general E-W direction over a flow line visible on satellite images. This flow line represents the boundary between the Lambert Glacier Flow Unit (on the west) and the Mawson Escarpment Ice Stream (MEIS) Unit (on the east). The aim was to see if there is any discernible difference in the ice of these flow units due to their different source regions (e.g. in ice thickness, properties, seismic velocity, etc). This was the longest seismic dataset collected upon the AIS, totalling 3.34 km in survey length and 3.25 km total CDP profile length. Hence it is the best opportunity presented to date to view changes in features over a larger distance.

Figure 6.2 shows the location of the CT Line with respect to nearby refraction surveys for anisotropy (which will be discussed in Chapter 7), and Figure 6.3 shows the CT line in relation to the Lambert-MEIS flow margin. The boundary as marked intersects the CT Line 1350 m in from the west end of the survey line.

6.2.1 Processing and Results

The same sequence as that used for the improved processing of the G2A0203 seismic line was used to process the CT Line with Disco Focus at Geoscience Australia (refer to Section 4.1.2). The only difference to this sequence was different post-stack filters were applied. For the CT Line, an additional post-stack step of a K-L transform was applied to suppress groundroll noise. The CDP profile produced for CT Line is shown in Figure 6.4.

Upon observing the CT Line profile, certain features other than the apparently horizontal ice-water interface stood out as being more significant, one being a reflection produced in between that of the base of the ice and the seafloor, i.e. from within the ocean water column. The other is the presence of variations in seafloor topography over

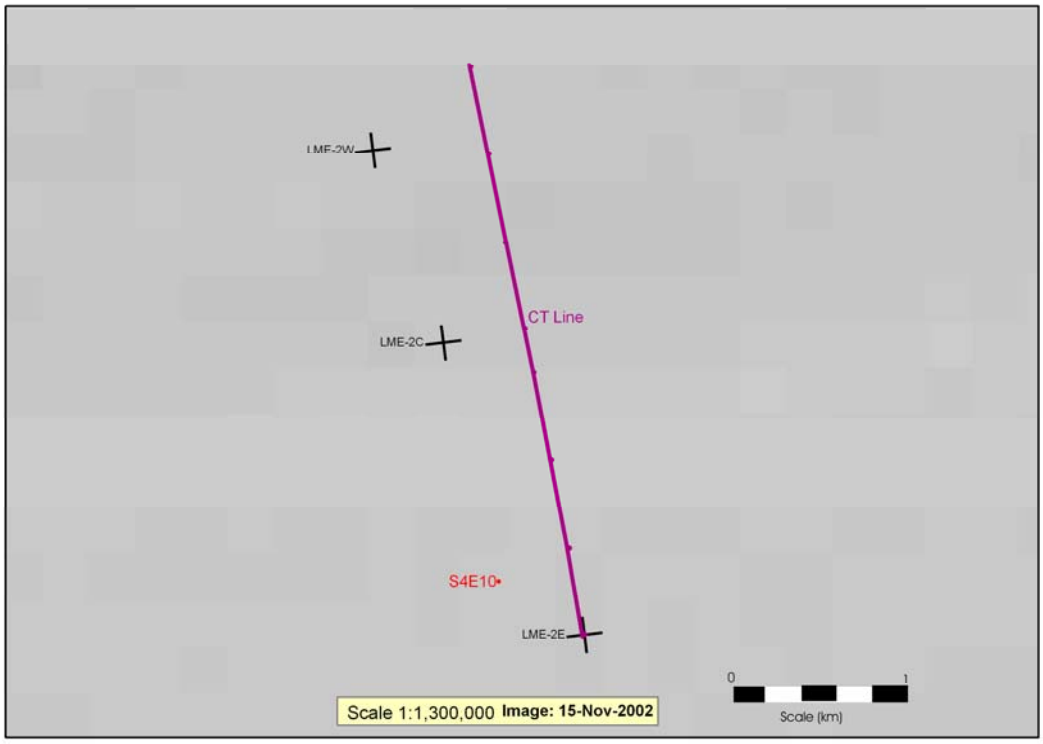

Figure 6.2 – Location of the CT Line and surrounding survey sites

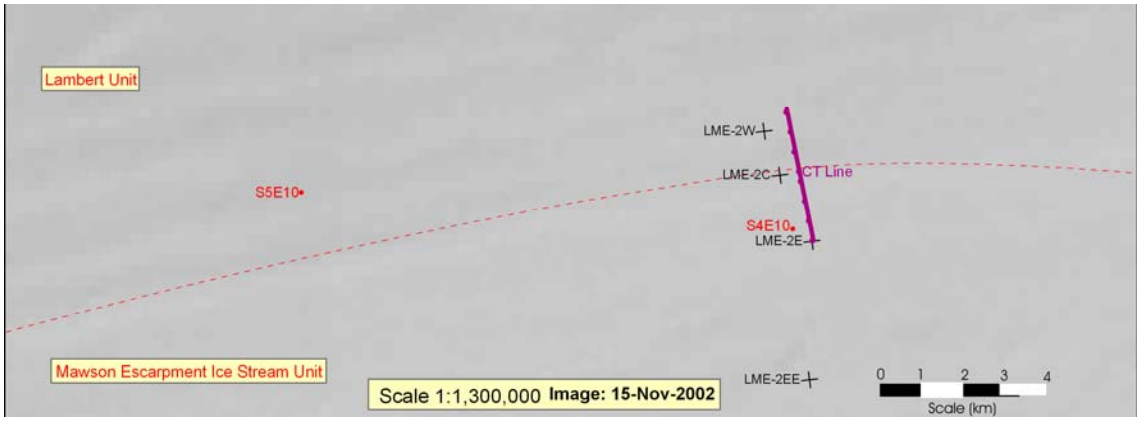

Figure 6.3 – CT Line showing where the Lambert-MEIS Flow Unit boundary passes through it at approximately 1350 m from the west end of the line.

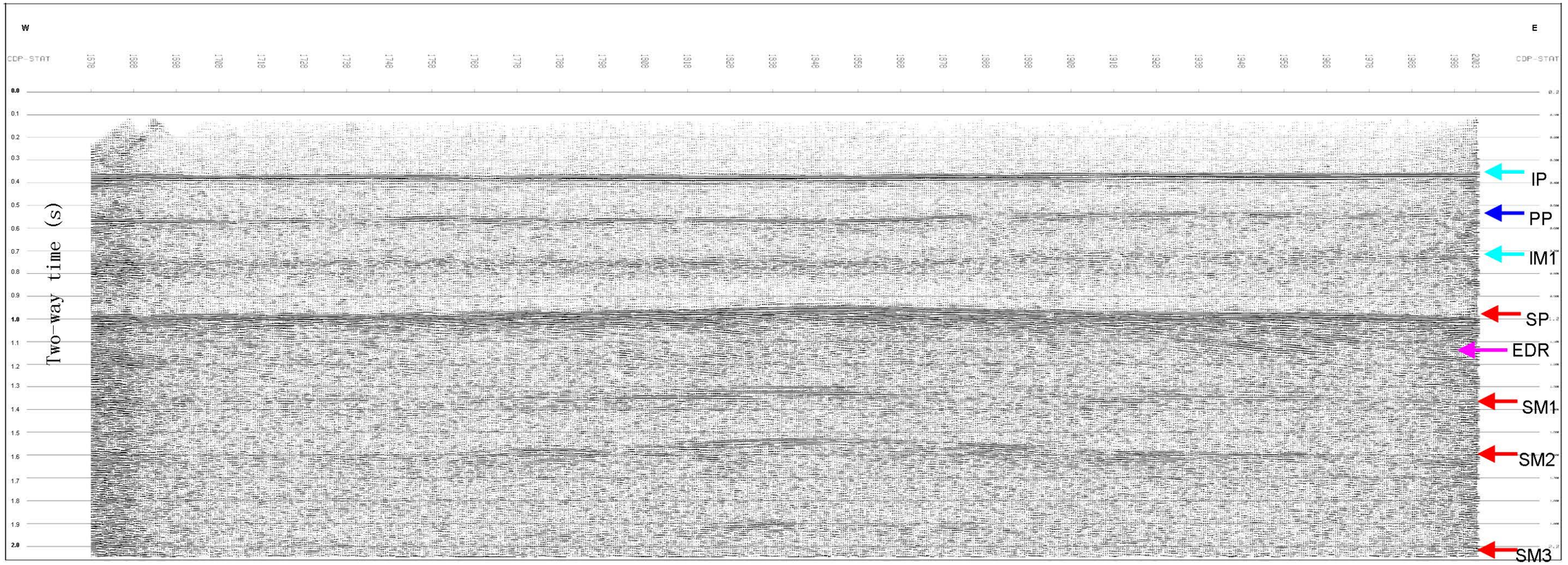

Figure 6.4- CT Line CDP profile. Reflections: IP = Ice Primary (base of ice shelf); PP= Pycnocline; IM1 = IP multiple; SP = Seafloor primary; EDR = East-dipping reflectors (apparent dip angle ~ 10-15°); SM1-3 = SP multiples (SM1 is the ice-seafloor multiple; SM2 is the pycnocline-ice-pycnocline-ice-seafloor multiple; SM3 is the seafloor-seafloor multiple)

this length of the line. Prior to the CT Line, the longest seismic survey on the AIS was the ~1 km G2A0203 Line, and the seafloor was revealed at this and other previous locations to be a flat surface, either horizontal or with an unvarying shallow dip.

There are 3-4 reflections visible at the base of the ice. In the east of the CT Line, the earliest arrival time is 355 ms, and in the west this occurs at 363 ms. The time of these arrivals does not vary more than 1-2 ms until a step from 355 ms to 363 ms is seen at CDP-STAT value 1896 (2180 m from the western end of the line).

Seafloor topography varies, and shows a hillock in the approximate centre of the CT Line, with the peak visible in this line at 929 ms at CDP-STAT 1850-1860 (1720 m to 1820 m from the west end of line, a distance of 100 m). The seafloor dip decreases to the west around CDP-STAT 1781 to the west end of the line, varying between 973 and 980 ms respectively. To the east of the hill, the reflection begins to level out at CDP-STAT 1915, arriving at 968 ms. Eastwards from here, the seafloor arrives at 970 ms at 1988 CDP-STAT, and then the dip appears to increase again as the east end of the CT Line shows this reflection arriving at 998 ms.

An intra-water column feature produces a reflection at ~550 ms in the seismic record. In the west this reflection arrives at 560 ms, varying from 548-565 ms until the reflection appears fairly horizontal at 557 ms from CDP-STAT 1800 to 1853 where the reflection begins to arrive earlier in the record. At CDP-STAT 1896 this arrival time has decreased over this relatively short distance to 533 ms. East of here the reflection again remains fairly horizontal, decreasing slowly to 526 ms at CDP-STAT 1930. From here to the east end of the CT Line, the reflection increases in time to 531 ms at the line's end.

It is interesting to note the rapid decrease in the intra-water reflection time occurs between 1750-2180 m from the west end of the line, spanning 430 m. The western location lines up with the peak of the hill on the seafloor, and the reflection time steadily decreases until it reaches the location of the sharp change in the ice base reflection's arrival time.

A summary of these arrival times, with CDP-STAT values, Station value, position along the CT Line, and calculated depths is given in Table 6.1. The seismic P wave velocities used for these calculations are the same as those used for the seismic CDP lines previously discussed in this thesis: 3703 ms^{-1} for ice, and 1452 ms^{-1} for sea water. It should be noted that depths of reflections have been calculated assuming there are no lateral changes in seismic velocity of ice or water. If there were a lateral change in either ice or water velocity this would of course affect the lateral variation in calculated depths and thicknesses. Further investigation of the ice and water properties at this location would be required to resolve any lateral changes in velocity, therefore no assumptions have been made regarding lateral variation of velocity and the discussion of results hereafter applies to a laterally uniform velocity scenario.

The ice depth varies by 15 m, with the eastern side being thinner than the west. The intra-water reflection varies in thickness by a maximum 9 m in the west part of the line, and then quickly decreases thickness by 18 m from 1750-2180 m along the line. This matches the decrease in the ice thickness at 2180 m within the error of the calculated depths. In the east part of the line, the depth to the intra-ice reflection decreases a further 1-5 m. For the depth to the seafloor, it decreases by 5 m over the first kilometre of the CT Line, then quickly decreases another 32 m to the shallowest part of the seafloor (the peak of the hill) at a depth 37 m closer to the surface than the start of the line, 1.7-1.8 km away. On the east side of the hill, the seafloor sits at a level ~8 m higher that in the west part of the line. In the eastern 150 m of the line, the seafloor deepens by 5 m.

The resulting average calculated thicknesses of these layers are given in Table 6.2. The ice shelf ice and Water Body 1 (the layer under the ice base) show two distinct thicknesses in the west and the east side of the CT Line. The ice thickness has been discussed above. The thickness of Water Body 1 changes from 141 m in the west to 125 m in the east, with a change of 18 m occurring between the seafloor hill and where the ice shelf thins.

Table 6.1 – CT Line Seismic Depths: For various locations along the line for each reflection, giving errors. Depths calculated using ice velocity 3703 ms^{-1} and sea water velocity 1452 ms^{-1}. The change in depth across the CT Line is calculated, giving each reflection a depth of 0 m at the 0 m position (east end of the line).

		Position							
Reflection	**Arrival time (ms) Error ±3 ms**	**CDP-STAT**	**Seismic Line Station**		**Position along line (With station 18960 = 0 m, station 20030 =3250 m)**		**Depth below surface (m)**	**Depth variation (using depths at position 0 m as base value)**	**Depth error (± m)**
Ice shelf base	363	From west to 1896	16780	18960	0	2180	672	0	5.6
	355	From 1896 to east	18900	20030	2180	3340	657	-15	5.6
Pycnocline (intra-water reflection)	560	1678	16780		0		815	0	2.2
	548	1749	17490		710		806	-9	2.2
	565	1760	17600		820		819	4	2.2
	557	1800-1853	18000	18530	1220	1750	813	-2	2.2
	533	1896	18960		2180		796	-20	2.2
	526	1930	19300		2520		781	-25	2.2
	531	1960	19600		2820		785	-21	2.2
Seafloor	980	1678	16780		0		1120	0	2.2
	973	1781	17810		1030		1115	-5	2.2
	929	1850-1860	18500	18600	1720	1820	1083	-37	2.2
	957	1896	18960		2180		1103	-17	2.2
	968	1915	19150		2370		1102	-9	2.2
	970	1988	19880		3100		1104	-7	2.2
	998	2003	20030		3250		1124	13	2.2

Table 6.2 – Thicknesses of layers displayed in the seismic data, given as average layer thicknesses in the east and west, with specific layer thicknesses calculated for the location of the hill and ice-step. The change in thickness measured across the CT Line has been calculated also.

	Lambert Gl. Flow Unit			MEIS Flow Unit
Layer	**West side of line**	**At Hill Peak (~1770 m)**	**At Ice-step (2180 m)**	**East side of line**
Ice	672	672	672/657	657
Water Body 1	141	141	123	125
Water Body 2	304	270	323	328
Total water column	445	411	446	453
Change in thickness from west-CT Line thicknesses:				
Ice	0	0	-15	-15
Water Body 1	0	0	-18	-16
Water Body 2	0	-34	19	24
Total water column	0	-34	1	8

Although the thickness of Water Body 1 has immediately decreased by 3 m where the ice thins, it also decreases by a further ~15 m in the east. The total Water Body 1 decrease in thickness of 18 m is the same as the decrease in the depth of the reflection at the bottom of this layer, which occurs between the hill and the ice-step. This may raise the question of whether Water Body 1 truly decreased in thickness at the ice-step or whether the change in the pycnocline reflection's depth was due to the ice thinning, but the nature of the seismic reflection shows both have occurred. If these changes in depth and thickness were only due to the ice shelf changing depth/thickness, then the seismic profile would show the pycnocline reflection here as a step also, but it is instead a gradual change over hundreds of metres.

The total water thickness (measured from ice base to seafloor) is 8 m thicker in the east compared to the west. Although Water Body 1 has thinned here, the seafloor is ~8 m higher in the east and there must be more water in total to make up the difference. The total water column is thinnest at the location of the seafloor hill. The thickness of Water Body 2 varies across the line, controlled by the seafloor depth and the base of Water Body 1, which follows the base of the ice rather than conforming to the seafloor.

Until recently the only nearby drill site was AM03 at 13 km in the direction 254°, which has an ice thickness 722 m and seafloor at 1339 m. The recent AM06 site, located just west of the northern tip of Gillock Island and within the MEIS Flow Unit (see Figure 1.1 for AM06 and Gillock Island locations, and their proximity to the CT Line), is 38 km from the west end of the CT Line, at a grid bearing 039°. At this location AMISOR measured an ice depth 607 m and the seafloor at 902 m.

From Wen et al.'s (2010) basal melt/freezing rate model, the basal melting rate between CT Line and AM06 can be read to be 0.2-0.5 m a^{-1}. The distance between the sites (based on GPS positions) is ~38±0.5 km, and the surface ice velocity is ~300 m a^{-1} (Young & Hyland, 2002), which would equal a decrease in thickness of ~25-63±1.2 m from CT to AM06 at the given melt rate (Wen et al., 2010). AM06 is situated in the MEIS Flow Unit, hence the eastern end of the CT Line ("CT-east") will be used for the comparison of ice thickness, since this maps in the same ice stream. The measured change in ice basal depth between CT-east and AM06 is 50±5.6 m, however this only accounts for basal ice change. Surface accumulation must be taken into account as well. Figure 2.24 shows an increase in the surface accumulation layer between AM04 to AM01 of 36 to 58 m over the 67.8±0.5 km distance (Treverrow et al., 2010). That is an increase of 22 m, or 0.32 m/km. Similarly, thicknesses given in Craven et al. (2009) indicate an accumulation rate of 0.3 m/km between JP and AM04, and a rate of 0.33 m/km for AM04 to AM01. For the distance from CT to AM06, this would be an increase in this surface layer of 11.4-12.5±0.3 m. The revised decrease in ice thickness between the sites would be 12.7-51.6±1.5 m. The change of 50±5.6 m between CT and AM06 is within the upper part of this range. This suggests the calculated ice thickness at CT-east is within reason, and supports the basal melt value modelled by Wen et al. (2010) in this location may be nearer to 0.5 m a^{-1} than 0.2 m a^{-1} .

6.2.2 Interpretation

The structure of the ice as revealed by the seismic data shows a sharp decrease in ice thickness at 2180 m along the line. No visible differences were observed at the surface in the field. and precise elevations along the CT Line have not been available for

inclusion in this study. The closest sites where GPS elevations have been processed (by Rachel Hurd, data sourced from pers. Comm. B. Galton- Fenzi) are the eastern S5 regional seismic survey sites. These sites cross the Lambert Glacier (LG)-Mawson Escarpment Ice Stream (MEIS) boundary, with S5E10 (Shown in Fig 6.3) on the Lambert Glacier Unit side and S5E15 to S5E25 (sites are 5 km apart) on the MEIS Unit side of the boundary. The elevation, H, at S5E10 is 87.22 m, and 85.18 m, 83.64 m, 81.48 m at S5E15, S5E20, and S5E25 respectively. This shows a 2.04 m, 1.54 m and 2.16 m decrease in elevation from S5E10 to S5E25 between each site. Per kilometre this is a rate of 0.408 m/km, 0.308 m/km, and 0.432 m/km decrease in elevation respectively.

The LG-MEIS boundary occurs between S5E10 and S5E15 (Fig 6.3, Fig 3.1). The boundary intersects the line between these two points ~1.5 km E from S5E10. This distance would equal an interpolated elevation of 86.61 m (to 4 s.f.) at the boundary, using the rate -0.408 m/km elevation change. At 3 km east from S5E10 (an equivalent location for the end of a line the same length as CT Line) the interpolated elevation is 86.00 m (to 4 s.f.). From this point to S5E10 is a difference of 1.22 m.

Equation 6.1 from Renner (1969, Equation 1) can be adapted to find the floating surface ice elevation (h) (Equation 6.2) from ice thickness H, density of water p_w, and density of ice p_i.

$$H = \frac{p_w h}{p_w - p_i} \qquad \text{(Equation 6.1)}$$

$$h = \frac{H(p_w - p_i)}{p_w} \qquad \text{(Equation 6.2)}$$

The closest values for water density are from AM03. CTD calculations give a density range of 1030.75-1033.5±0.5 kg/m^3. Wen et al (2010) give ice density values for sections of the AIS. Using their value range of 903.5-890.5 for the section of the AIS 315 km to the ice shelf front, an interpolated value can be reached for CT/AM03 at the distance 200-200 km from the ice shelf front. This calculated value for p_i is 895.2±0.8 kg/m^3. Using H values of 672 m for LG Unit ice and 657 m for MEIS Unit ice,

Equation 6.2 give values of H of 88.37-89.93 m in the LG Unit, and 86.40-87.92 m in the MEIS Unit. Error in these heights is ±0.24 m. This gives a difference of 1.97-2.01 m, which is 0.75-0.79 m greater than the interpolated elevation results from the S5 line data. The lowest possible elevation change from these calculations (from the errors) is 1.73 m. Assessing whether this elevation change occurs over the CT Line would require the processed kinematic GPS data to be processed and made available. Better estimated of p_w, and p_i would also improve the comparison of data. From this analysis it may be possible that the CT Line shows an elevation change that could support the likelihood of MEIS Unit ice being thinner than LG Unit ice.

In terms of the possible effect of differences in the near surface velocity profiles between LG and MEIS Unit ice, refraction results at anisotropy survey sites LME2 -E and LME2-W can be of use. In comparing the maximum velocities of the combined EW and NS line results (Table 7.1), the LME2-E (MEIS) site shows higher velocities at 40 m depth of 5 m/s EW and 33 m/s NS. Velocity errors as given in Table 7.1 are ±100 m/s, so the difference in the modelled velocities is well within error, and the value of 3703 m/s used for depth calculations is also within the error range. The near surface velocities therefore are effectively equal, and so a comparison of near surface effects on the arrival time of the ice base reflection cannot be justified with the available data.

As mentioned earlier in this chapter, the boundary between the Lambert Glacier Flow Unit and the MEIS Flow Unit passes through Line CT. From the traces made from satellite imagery this margin possibly occurred at 1350 m from the west end of the line. What the CT seismic data shows is that this margin may occur at 2180 m from the west end of the line, 830 m further to the east. This places it between the LME-2C and S4E10 sites as shown in Figure 6.2. This change in ice thickness at the margin can be explained by an initial difference in thickness of the ice units as they joined the ice shelf. The Lambert and MEIS Flow Units have their source in different parts of the AIS hinterland. The Lambert Glacier is extremely thick at its source and at the southern grounding line of the AIS. Figure 2.15 shows a thickness of ice entering the south of the AIS of ~2 km, whereas the ice entering from the east (at the MEIS) is ~1 km thick. It is possible that the ice remaining from the Lambert Glacier would be thicker than that of MEIS ice.

In terms of the seafloor, the hill evident in the seismic data is the largest expression of bathymetry measured as part of this seismic project. It shows that even over a few kilometres there can be a variation of ~40 m in the seafloor depth. The location of the hill relative to the ice flow unit margin is also a matter of interest. It is not in exactly the same location, sitting ~400 m further west, but it may still be related to glacial dynamics. It is a possibility that the hill is a thicker unit of sediments that may be a linear glaciation feature such as a glacial moraine or a drumlin on the seafloor (Larter et al., 2009) – the seismic data shows sub-seafloor sedimentary reflections to a greater depth under the hill as opposed to the sub-seafloor areas away from the hill. A bathymetric relief of ~40 m is not unusual, nor very high, according to Later et al. (2009). The seismic profile also displays east dipping reflectors in the ~200 ms below the seafloor, all with an apparent dip of 10-15° in the profile. The bathymetric high may be due to a harder more prominent layer within these dipping sedimentary layers – that after erosion maintains a higher elevation than the surrounding material. The interpretation of this feature would have to be confirmed by future surveys over different parts of this ice margin, and over other major Flow Unit margins to see whether this is a linear feature associated with major flow unit margins, or whether it is a localised feature.

An intra-water column reflection had not previously been observed in seismic data from the 2002/03 season, however one similar feature had been observed in seismic data collected in the 2003/04 season by Hugh Tassell (then of University of Tasmania) as part of his honours thesis (Tassell, 2004). It was however not observed in such great detail as is seen in the CT Line data, having been described as a “patchy reflector” (Tassell, 2004), with the reflection being discontinuous across the 1 km CDP profile. Tassell (2004) proposed that the reflection corresponded to a thermohaline interface.
A more detailed hypothesis for the reflection has been proposed by Ben Galton-Fenzi (UTas, pers. Comm.). He suggested the reason for this water reflection can be attributed to the presence of a pycnocline (see Section 6.1.1 of this chapter for a definition). In other words, that the reflection is not solely dependant on a temperature change as proposed by Tassell (2004), but may also be due to a salinity change, hence an overall change in water density. The term pycnocline is therefore a more accurate designation.

The two Water Bodies delineated by the seismics at the CT Line can be classified according to the interpretation of Yabuki et al (2006) described in Section 6.1.2. The depth to MCDW is given as 200 m in Prydz Bay, with this water entering the AIS cavity where it is cooled and forms ISW and saltier LSSW, or HSSW according to Nunes Vaz & Lennon (1996). These waters exit to Prydz Bay where the ISW is ~500 m thick.

We can therefore define Water Body 1 as ISW, and Water Body 2 as saltier LSSW or HSSW. To discern which classification Water Body 2 is requires some information about the salinity to make a definition. Any CTD measurements taken at AM06 were not available for discussion in this thesis, however we can compare values to AM03 data. Here the salinity is at a maximum near the seafloor with a value ~34.55. This is close to the 34.6 salinity value Nunes Vaz & Lennon (1996) used to define HSSW, and matches previously sub-ice shelf water body definitions by Holland & Feltham (2005). Therefore Water Body 2 can be defined as HSSW.

Looking at the thicknesses, depths and locations of the water bodies in relation to the changes in the ice and seafloor can reveal some information about what may control these water bodies, and what may be happening in the water column. Although a complete theory of what controls these bodies of water in this area can not be fully completed without information upstream and downstream of the CT Line, the following discussion aims to interpret the available two dimensional data.

As has been discussed in Chapter 5, the prevalent ocean circulation at the front of the ice shelf is a large rate of flow into this eastern half of the ice shelf (Hemer & Harris, 2003). With this being the case, the water under CT would be newer to the AIS cavity compared to water on the western side of the AIS such as at AM01 and AM04. At AM03 the thickness of the ISW was similar to CT, ~140 m, whereas at AM01 (taking pycnoclines seen in Figure 5.4 at 640-670 ms) the ISW is ~277-299 m thick. This would be plausible with the water travelling south from CT undergoing further cooling (thicknening the ISW) and travelling out to the ice shelf front via AM01.

What we can infer from the evidence presented in the CT Line seismic data is that the ISW itself, its layering for instance, is controlled by the ice shelf base more so than

bathymetry. The ISW thins and becomes shallower as the ice does, it does not thin and then thicken once more over the east of the hill. The location of the decrease in the ISW thickness aligning with the location of the local bathymetric high on the seafloor is unlikely to be unrelated. Though the ISW circulation (and therefore perhaps thickness) may be affected by the thinning of the AIS to the east, the seafloor hill would most likely have some effect on local circulation as well.

Looking closely at the pycnocline reflection times in the west, it can be observed the arrival times vary from 560 to 548 to 565 to 557 ms from 0, 710, 820, and 1120 m along the line respectively. The pycnocline arrival time east of 1120 m is affected by the ice thinning and the hill. This change describes a sinusoidal wave form, changing from a nominal zero at 0 m along the line, to -9 m, +4 m then to -2 m. The equation of a line drawn through these points is $y = -5x10^{-6}\chi 2 + 0.0129\chi - 10$ and the amplitude of the wave would be ~7 m, with a wavelength between the troughs of ~200 m. This may be an internal wave travelling along this pycnocline (Baum, 1997; Zimmerman et al., 2005), however the interpretation would benefit from at least one second definite measured peak to either the east or west. The CT line ends before another peak in the west is seen and the hill and ice thinning disrupts this waveform to the east.

6.2.3 Seismics and pycnoclines

The ability of seismics to pick up the difference between two bodies of water with differences in density (differences in temperature and/or salinity) is supported by other marine seismic surveys undertaken in open waters (Holbrook et al., 2003). The marine seismic data in that project was collected over the North Atlantic Current and Labrador Current. It shows reflections from layer boundaries in the water with a reflection coefficient of 0.002, relating to a change in seismic velocity of only 6 m/s (Holbrook et al., 2003).

The water bodies themselves have been defined, and the intra-water reflection itself has been theorised to be a pycnocline. To define whether there could be a pycnocline present under the AIS (and under the CT Line) and to determine which physical

properties have caused this change, and whether they are significant enough to produce this intra-water seismic reflection, further analysis is required. To address this, the seismic data should be compared to measured water properties and the Z and R values derived from them.

6.3 CTD and reflection coefficient data analysis

The nearest sites of AIS water cavity property measuements that can be compared to CT seismic data are the AMISOR sites AM03 and AM04. In the recent 2009/2010 summer season AMISOR also drilled the new site AM06, as mentioned previously, however CTD data for this site has not been made available to this study so AM06 CTD data will not be discussed here.

The sites AM03 and AM04 are both within 15 km of CT. In this section AM03 data only will be discussed in comparison with the CT Line since it is both closer to CT than AM04 and AM03 and CT are located at a similar distance from the southern grounding line. CT and AM03 are also both located where there is no marine ice accretion at the base of the AIS whereas AM04 is a site of marine ice accretion. Comparing sites of a similar environmental setting will produce more significant results.

The data from AM03 was obtained from Ben Galton-Fenzi (University of Tasmania) in the original format and a 2 dbar averaged format. The 2 dbar averaged data is at too coarse a spacing for the purposes of looking for what is possibly only a small change in density, therefore the original unaveraged data were used for calculations. Plots of the salinity and conductivity measured at AM03 have already been shown in Figures 4.5 and 4.6. The entire CTD dataset for AM03 consists of more than 20 000 individual data points. Due to the complexity of the calculations to first find density and seismic velocity from the supplied temperature, salinity and pressure values and then to calculate acoustic impedance (Z) and reflection coefficient (R) from these, an online calculator was used for the first step of the calculations (shown in Appendix B). Even so, a total of 26 000 data points was far too many for a timely analysis of the data, and only sections of interest were chosen to study. Calculations were performed on both the

down- and up-cast data, they were not averaged before calculating; this could be done post-calculation if necessary.

The following processing steps were followed to minimise total processing time:

1. Plot all AM03 CTD data with temperature, salinity and depth (pressure).
2. From the plots, areas of interest were selected – these were sections of data where there appeared to be a significant, or somewhat greater, change in temperature or salinity. These were depths that were most likely to be a pycnocline, and show the greatest acoustic impedance contrast. They were also chosen to include the depths of reflections modelled from the seismic data. Sections of data with constant temperature or salinity change (i.e. that directly related to density) were also highlighted as control comparisons on the pycnocline boundary data.
3. A new abbreviated dataset was created, reducing the total datapoints from 26000 to 530 points.
4. The salinity, temperature and pressure values for each discrete datapoint were entered into a web-based calculator (Appendix B).
5. The data output values from the web-based calculator were recorded – these parameters were density, depth, seismic velocity, and freezing temperature.
6. Acoustic impedances were calculated using Equation 4.1 from the density and seismic velocities.
7. From the calculated Z, reflection coefficients were calculated, as per Equation 4.2. Since a change in density would need to be across a significant distance in depth, R values were calculated not just for adjacent datapoints, but also for the difference between datapoints up to three apart in the CTD dataset, relating to a maximum depth offset of 2 m.

The unprocessed AM03 temperature and salinity values between 840-880 dbar - which covers a range of depths near where the G2A0203 Line pycnocline occurs at an ~860 m calculated depth - are shown in Figures 6.5 and 6.6, respectively. Two areas of interest are highlighted from the profiles where there is a greater rate of change in properties, between dbar 857-861 and 870-875. Over these pressures, temperature displays a greater increase in rate of change than salinity.

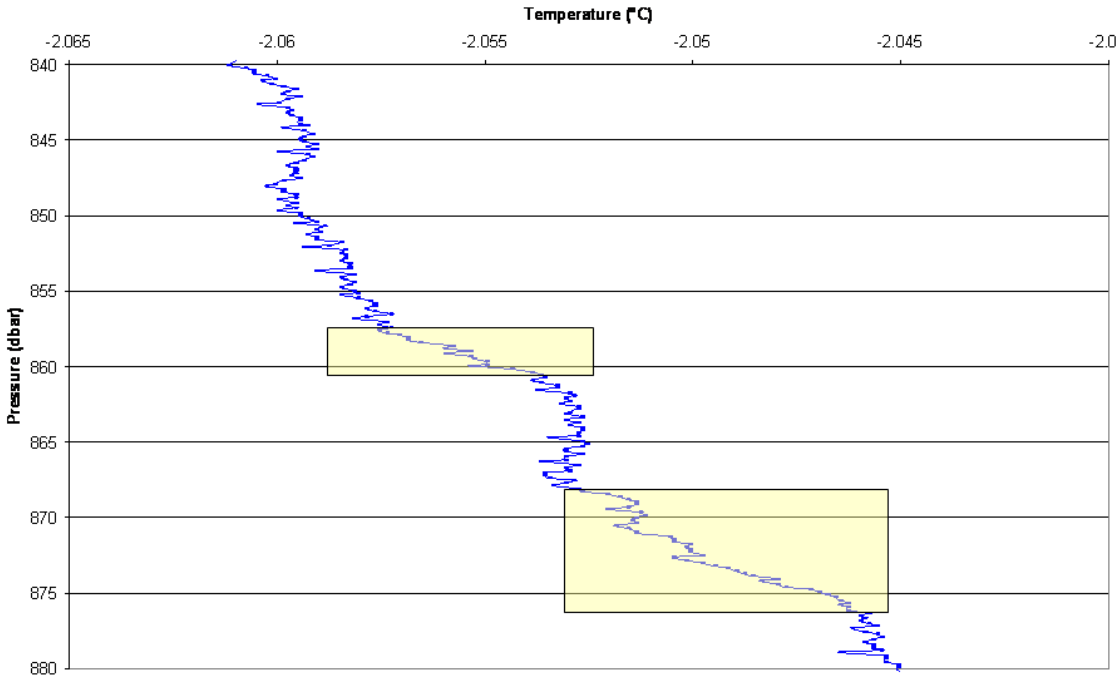

Figure 6.5 – AM03 CTD temperature profile at depths near G2A0203 Line pycnocline depth (860 m). Note: to convert dbar to metres subtract ~10. Yellow highlighted areas indicate zones of a rapid increase in temperature that could lead to a density change.

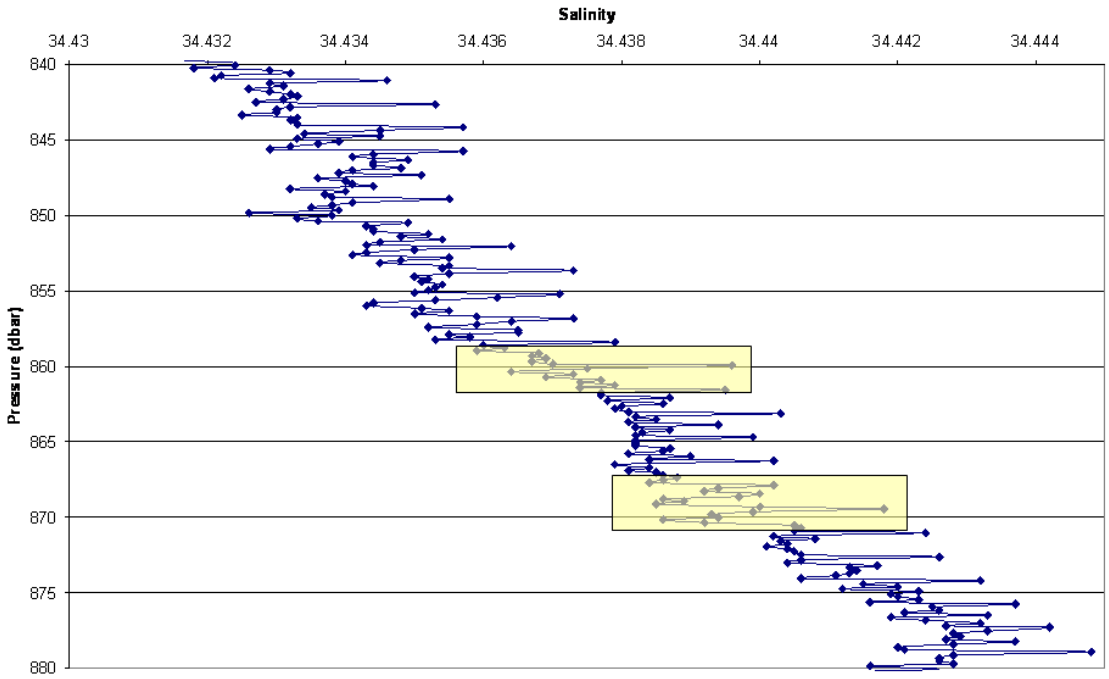

Figure 6.6 – AM03 CTD salinity profile at depths near G2A0203 Line pycnocline depth (860 m). Note: to convert dbar to metres subtract ~10. Yellow highlighted areas indicate zones of less random oscillations of salinity that show a slightly larger spiked increase in salinity.

R values were calculated from the acoustic impedances using a range of depth separation between each acoustic impedance measurement. The CTD data was collected at a spacing of 0.2 m, however the seismic data may not resolve layers this thin, so R was calculated on larger scales of depth differences. For the two zones highlighted in Figures 6.5 and 6.6, the calculated depth range becomes 849-853 m and 862-867 m. From the Z values for these depths, R equals $-8x10^{-5}$ and $1.61x10^{-4}$ respectively. The R values above and below zones of interest are between 5 $x10^{-5}$ to $9x10^{-5}$ for 849-853 m and $2x10^{-6}$ to $2x10^{-5}$ for 862-867 m. So although there is a larger temperature difference over 849-853 m, it shows no significant change in R. However, for 862-867 m the R value increased by 20-100 times the R values calculated above and below this narrow range. This suggests that over this 5 m change in depth there is a significant increase in R, which could produce a seismic reflection. The seismic results at G2A0203 (see Chapter 4) showed a pycnocline at 860 m depth, and at 853-859 at G2A0506. These depths correspond very well with the depths where R is significantly increased. The R value of $1.61x10^{-4}$ is not very large, but it is would seem to be large enough to produce a reflection in the water under the AIS.

A second method of testing this hypothesis that a salinity-temperature dependant density change over a finite distance in water (a pycnocline) may be present in AIS ice shelf cavity water and that it can be imaged with the seismic technique is to use forward modelling to produce synthetic seismograms to compare to the real seismic data. Layer models based on thickness and P wave velocity have been forward modelled in Reflect 1.0 Build 7 software (Craig H. Jones, 2004-2006, based upon the original 1992 ReflectModel and ReflectSolve software by Douglas C. Burger and H. Robert Burger) to produce synthetic seismograms and to give values for the arrival time of these synthetic reflections and other seismic waves such as ground roll, air wave, direct wave and first refraction arrivals.

Input models were based upon the P-wave velocity values for water gained from the analysis of CTD data at AM03, and on the modelled thicknesses and P-wave velocity for ice measured at the G2A sites – as described in Chapter 4 of this thesis and in McMahon & Lackie (2006). Over the depth below surface of 862-867 m (within the water column) where the R difference was significant, the calculated change in P-wave velocity for water is 1451.5 to 1451.7 ms^{-1}. Inputting these values as a simple model of

a 5 m thickness change with these two velocities, and using the survey geometry as employed at G2A of 24 channels at 10 m spacing and a 20 m shot interval, a synthetic reflection is produced (shown in Figure 6.7). As a test, the same thickness model was forward modelled for no change in velocity, resulting in no reflection, and for a change in velocity spanning the minimum and maximum water P-wave velocities calculated from the CTD data at AM03 – 1448.8 ms^{-1} and 1459.9 ms^{-1}. This produced a wavelet with the same apparent amplitude as Figure 6.7. If both velocity variations were introduced into the same input model, as a 1448.8 ms^{-1} to 1450 ms^{-1} change over 5 m (akin to the input for Figure 6.7) and then a change from 1450 ms^{-1} to 1459.9 ms^{-1} over 5 m (after a gap distance of 60 m to make sure any reflections do not interfere with one another in the synthetic seismogram), two synthetic reflections are produced (Figure 6.8). The earlier small amplitude reflection relates to the 0.2 ms^{-1} change in velocity and the later larger amplitude reflection relates to the hypothetical scenario that the entire velocity profile of the AIS cavity water at AM03 occurred over a significantly shorter distance than in reality. Figure 6.8 shows that although the reflection produced by the relatively small velocity change at 862-867 m depth is orders of magnitude smaller than what would be produced by the maximum velocity difference in the water column, it is still significant enough to produce a reflection.

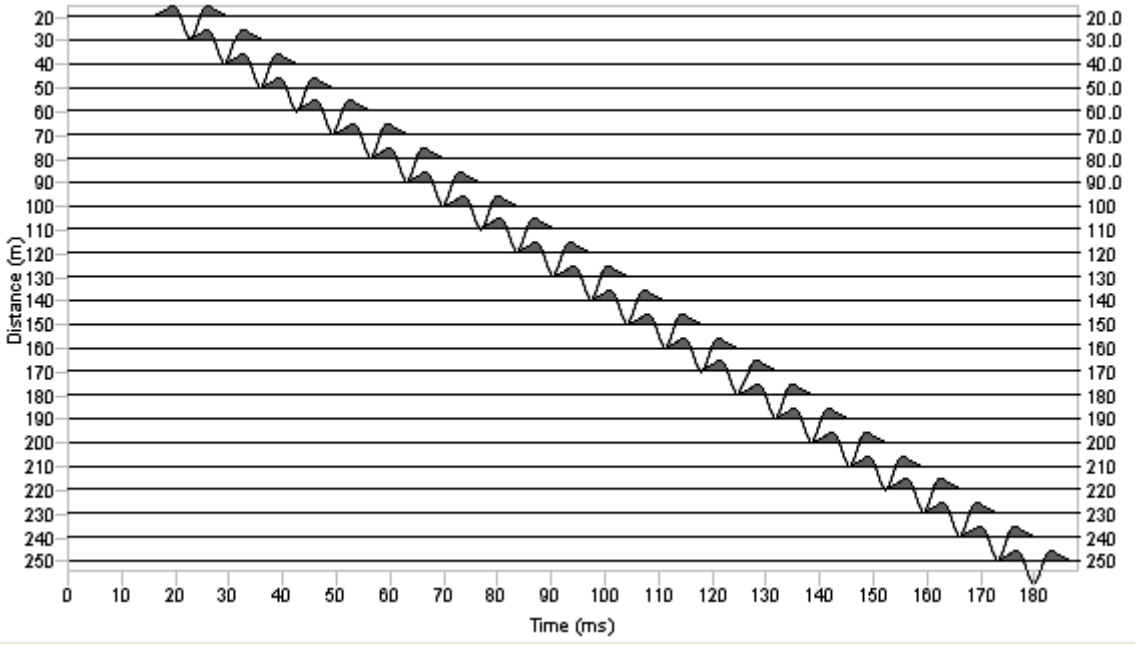

Figure 6.7 – Synthetic seismogram of a reflection resulting from a 0.2 ms^{-1} P-wave velocity change over a 5 m distance.

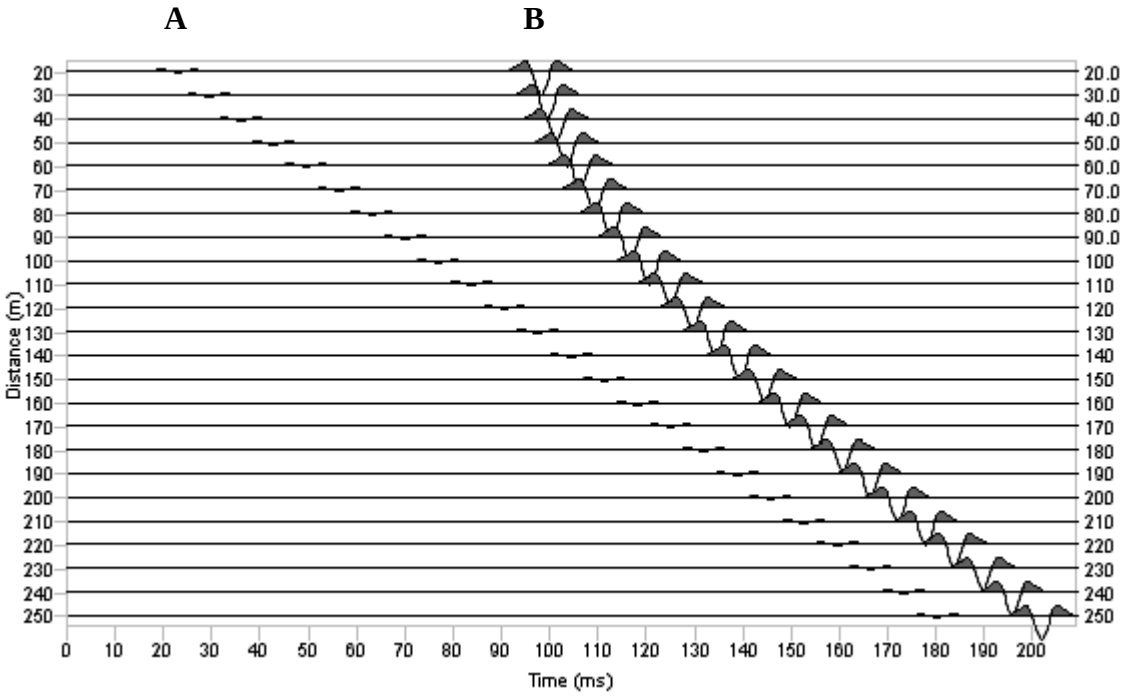

Figure 6.8 – Synthetic seismogram displaying reflections arising from (A) a 0.2 ms^{-1} P-wave velocity change over 5 m in the early record from 20-176 ms; and (B) a 10.1 ms^{-1} P-wave velocity change over 5 m in the late record from 90-195 ms.

As also discussed in Chapters 4 and 5, these intra-water reflections are not only observed at CT but are seen elsewhere in the seismic data from the AIS, with the next best example being displayed in the G2A seismic data from 2002/03 and 2005/06.

6.4 Discussion and implications

The implication of the results discussed in this chapter is that all marine seismic data could potentially hold information on the thermal and salinity profiles of the world's oceans. If seismic data was reprocessed looking at the water response rather than the seafloor and sub-seafloor, this information could provide plentiful data for oceanographers to input into and improve current ocean models. Some work has been started on comparing seismic data to CTD casts in the open ocean (Holbrook et al., 2003), and this would certainly be valuable to continue.

The AIS seismic data discussed in this chapter has shown that the seismic technique is an extremely useful tool for modelling the sub-ice topography, the ocean cavity and changes in ocean water properties under an ice shelf. Seismic data in concert with available CTD data can give scientists a much greater coverage of oceanographic information, and can greatly increase the detail and accuracy of ocean circulation models.

Chapter 7

AZIMUTHAL ANISOTROPY IN AIS STRAINED ICE: An experiment in applying the seismic technique

"Anisotropy resulting from non-random ordering of crystal axes produces effects on seismic wave propagation speeds measurable by both refraction and reflection techniques" (Bentley, 1975, p.113)

Since ice fabrics are closely related to the strain history of the ice, measuring anisotropy is of great potential value to the study of ice dynamics (Bentley, 1975)

7.1 Introduction

In the Antarctic summer season of 2004/05 a series of refraction surveys were carried out with the aim of investigating the anisotropic nature of buried previously-strained ice. Strain rates for the entire AIS have been mapped from surface velocity measurements by Young & Hyland (2002) (see Figure 2.20); this part of the seismic project attempted to investigate the effect of strain on the ice. That is, to discover whether deeper ice showed a preferred crystal orientation and hence a measurable seismic anisotropy that could be attributable to past strain in the ice, generally due to ice streams converging to form the AIS.

A crystal matrix is, in general, expected to be isotropic in nature although exceptions are found often associated with shear stress or flow (Bullen & Bolt, 1985). Bentley (1975) stated that ice fabrics are closely related to the strain history of the ice, and that

measurements of anisotropy are of great value to the study of ice dynamics. Budd (1972) stated that anisotropy appears to have a relation to large-scale flow patterns, and the mean crystal properties at a certain point represent the integral of the history of change along a trajectory from its origin at the surface.

The seismic technique is a suitable method for the investigation of anisotropy. Even during early geophysical work in Antarctica, the link between seismic results and crystal fabric was seen (Budd, 1972; Gow & Williamson, 1976). Anisotropic ice was revealed in ice at Byrd Station after the first ice core to penetrate to the bottom of the ice sheet (total length 2164 m) was completed in 1968. Budd (1972) cited that in the 1971-72 season Charles Bentley confirmed ice crystals may have considerable large-scale average anisotropy, but previous to this discovery anisotropic fabric had not been seen in other glaciers. Anisotropic fabric was observed as a gradual but persistent increase in *c*-axis preferred orientation, with a broad vertical clustering (Gow & Williamson, 1976) (see Figure 2.19).

This process of increased anisotropy with depth should be observable in other glaciers and ice sheets, although seismic evidence as reviewed by Kohnen & Bentley (1973) indicates strikingly different anisotropic patterns in the ice of different regions. Wide-angle reflection measurements have generally revealed that a good proportion of the ice sheet is anisotropic (Bentley et al., 1987).

As Budd (1972) stated, “although the association between the seismic anisotropy and the expected fabric patterns is encouraging, a thorough investigation is still needed of the large-scale seismic anisotropy and crystal orientation fabrics by detailed measurements of both in the same area in the field.” p.94. This project was undertaken for this purpose, and the seismic work we undertook was to be compared to the ice fabric study of AIS ice cores by Adam Treverrow (University of Tasmania, ACE CRC).

Although deviations from the conditions of isotropy are small, their effect on the propagation of seismic waves can be observed and provides important information about the average crystal orientation of the ice (Budd, 1972; Udías, 1999). Because of the properties of seismic body waves travelling through an anisotropic medium,

anisotropy is detected by observations of changes in P wave velocity along two perpendicular directions, and by observations of S wave splitting (Udías, 1999).

Considering there is strain in ice, it should be expected that a preferred orientation is the rule rather than the exception in ice shelf ice, and that it could vary widely with the shelf location (Crary et al., 1962). The work of Young & Hyland (2002) began the modelling of the areas of the AIS that are undergoing strain, and Treverrow et al. (2010) have measured the fabrics of some deep AIS ice. This seismic project aimed to contribute to this research, using seismic results to define anisotropy in certain areas.

7.2 What is anisotropy?

According to the definitions of Bullen & Bolt (1985), by **isotropic** we mean that the elastic behaviour of a medium is entirely independent of any particular direction, and that a material (still taken to be perfectly elastic) is **anisotropic** if it deviates from the directionally regular elastic behaviour of an isotropic material. In other words, "a medium is anisotropic if its intrinsic elastic properties, measured at the same location, change with direction, and it is isotropic if its properties do not change with direction" (Yilmaz, 2001, p.1961). The usual meaning of **seismic anisotropy** is a variation of seismic velocity, which depends on elastic properties, with the direction it is measured in (Yilmaz, 2001).

There are two main types of anisotropy, as defined by (Udías, 1999; Yilmaz, 2001). In a horizontally layered Earth the two cases of anisotropy are:

1. Vertical transverse anisotropy, known simply as **transverse anisotropy**:

   Velocities do not vary laterally, but vary from one direction to another on a vertical plane that coincides with a given lateral direction. For example, horizontal bedding, fracturing parallel to bedding, or horizontal alignment of a structural or mineralogical nature.

2. Horizontal transverse anisotropy, known as **azimuthal anisotropy**:

This is where velocities do vary in lateral directions, i.e. the velocity of the propagation of waves along one trajectory in a particular azimuth is different to that in a direction perpendicular. For example, fracturing in a direction other than the bedding plane, preferential alignment of crystals, cracks or heterogeneities along a particular azimuth.

The type of anisotropy of concern to this thesis is the latter, azimuthal anisotropy.

In terms of ice, "deviations from a random distribution of ice crystal axes in polycrystalline ice produce a dependence of velocities and amplitudes of seismic and electromagnetic waves on direction of polarisation and on direction of propagation through the ice." (Bentley, 1975, p.114)

7.3 Stress and strain rate in glaciers

In glaciology, simple shear is important to study as it is the dominant stress configuration and deformation state in the deeper parts of natural ice masses (Budd & Jacka, 1989; Jun et al., 2000). "Ice core and borehole studies along flow lines in ice sheets show that the ice crystal structure and flow properties evolve together with strain and rotation along the particle paths" (Budd & Jacka, 1989, p.107).

Near the base of the ice sheets large variations in stress and strain rate can occur between ice and bedrock (Budd & Jacka, 1989). Similar stresses and strains can be found in a horizontal rather than vertical direction between two streams of ice that converge together, as in the case of streams or glaciers merging to form an ice shelf. This is the situation occurring on the margins of the AIS; in the south where the Lambert, Mellor and Fisher glaciers and smaller tributaries merge, and also in the numerous ice streams entering from the eastern escarpment into the AIS.

The strain over an ice shelf varies with proximity to stress-causing features. For example, Figure 7.1 displays the pattern of strain rates across the Saskatchewan Glacier,

Canada. The figure shows the variance of strain rate across the glacier, both in direction and magnitude. There is strong shear parallel to the flow directions at the margins of the glacier and this is where the highest strain rate is located. The strain rate varies, becoming a small longitudinal compression at the centre of the glacier (Budd, 1972). The strain rates of the AIS are shown in Figure 2.20 in Chapter 2.

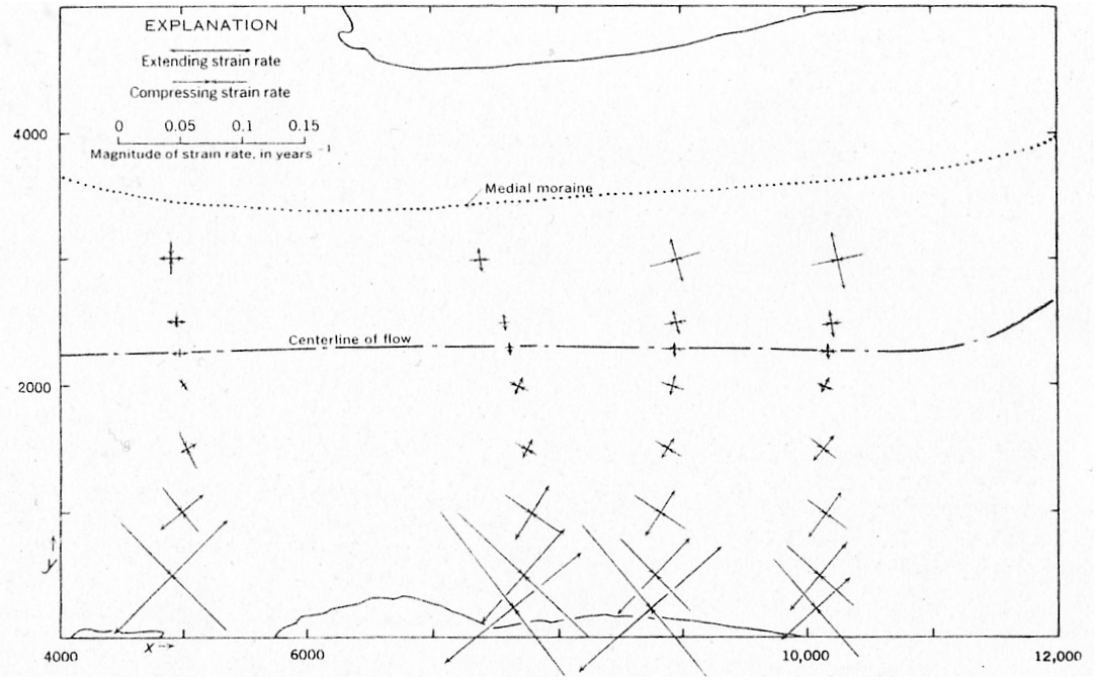

Figure 7.1 – Pattern of rate of strain across the Saskatchewan Glacier. Flow direction is from left to right. The crosses indicate strain rates of extension and compression and their magnitude (Budd, 1972, Fig 2)

7.3.1 Ice crystal fabric, strain and anisotropy

Ice crystal orientation is defined by the crystallographic *c*-axis, which in ice corresponds to the optic axis. Orientations of crystals are readily obtained on the Rigsby Stage, the technique essentially being the same as that for the study of quartz fabrics (Gow & Williamson, 1976).

In the case of a vertical uniaxial situation like an ice dome summit, uniaxial compression (i.e. vertical compression as ice is compacted as more snow/ice

accumulates) provides the rotation of the *c*-axis towards a compression axis. The enhancement of ice deformation caused by the favourable *c*-axis orientation fabric for vertical compression induces further rotation of *c*-axes toward the vertical axis (Azuma, 1999; Budd & Jacka, 1989). This is the basic principle of the formation of anisotropic ice fabric – compression leads to an alignment of *c*-axis orientations. As depth increases, the fabric of the ice changes. At Dome C, ice layering due to variation in surface snow accumulation persists to the depth of the snow-ice transition, but disappears by ~100 m (Gow & Williamson, 1976). Ice from directly below the snow-ice transition shows a random fabric, which is retained in the top 100 m or so of ice. Deeper in the ice a 2-3 maximum pattern occurs, but a preferred *c*-axis orientation gradually develops until a depth of ~1000 m where there are typically 2-3 maxima within 20-40° (Blankenship et al., 1982; Gow & Williamson, 1976).

Theoretical considerations of the development of anisotropic crystal fabric in simple shear deformation scenarios indicate a single-maximum fabric with the *c*-axis concentrated around the direction normal to the shear plane (Jun et al., 2000). In laboratory experiments a two-maxima fabric pattern was typically observed – one maximum with the stronger concentration of *c*-axes developed perpendicular to the shear plane, the second, of weaker concentration, developed several of tens of degrees (depending on strain) away from the shear plane towards the shear direction. This second maximum however disappears at large strains (Budd, 1972; Jun et al., 2000).

In summary, ice crystal *c*-axes can be oriented in the horizontal plane, or the vertical, depending on the mode of crystal growth and the deformation it has undergone. The general pattern for c-axis orientation measurements is two broad unequal maxima, with an angle 50±10° between them. This is the general type of pattern for simple shear in the horizontal direction across vertical planes, which is the strain geometry expected in a shear margin (Jackson & Kamb, 1997), and is the scenario being explored by this project.

Figure 7.2 shows crystal orientation fabrics for ice at 400-500 m depth at AM04. This shows there is a definite alignment of c-axis orientations at these depths, although the direction of this orientation is not constant throughout the ice. This ice fabric is marine ice, and may have undergone a different strain regime than meteoric ice that joined the

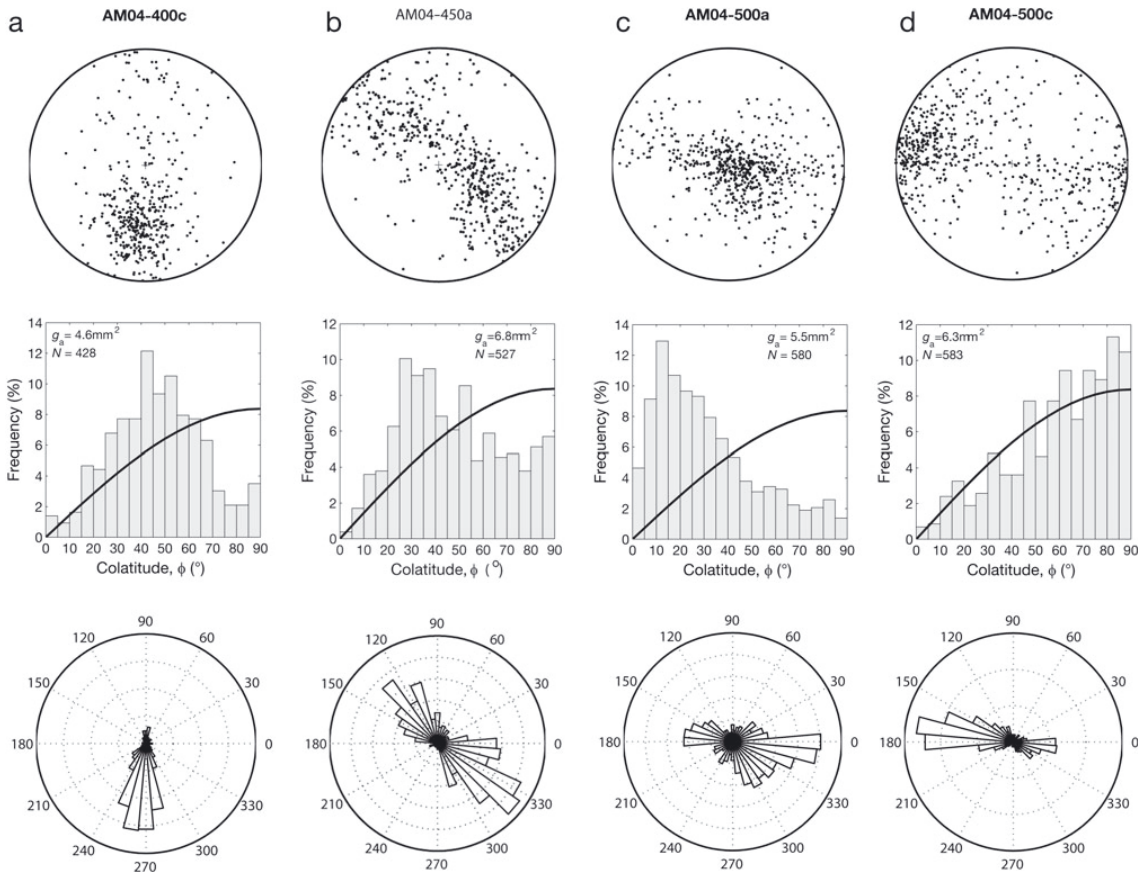

Figure 7.2 –Crystal orientation fabrics for AIS marine ice cores from the AM04 borehole at approximate depths 400, 450 and 500 m. Data are from the (a) horizontal AM04-400c, (b) horizontal AM04-450a, (c) vertical AM04-500a and (d) vertical AMo4-500c thin sections.(Treverrow et al., 2010)

AIS from the continent. Marine ice fabric may display a stress regime and changes in ice fabric akin, but in reverse to, the uniaxial vertical dome summit example, since marine ice accretes and compresses from the bottom up rather than the top down.

7.3.2 Distribution of ice stress and strain rates

Deformation of ice can be used to determine ice flow properties; strain rates can be measured directly and stress can be estimated from the geometry of deformation and the

ice density distribution. Various techniques for a direct measurement of deformation include: measuring borehole tilt, borehole closure, tunnel closure, and surface velocity and strain rates (Budd & Jacka, 1989). Borehole and tunnel closure are a flow response to the ice disturbance of having removed a bore of ice, so are not really representative of in situ flow properties of ice in the natural flow state which is particularly important to anisotropic ice (Budd & Jacka, 1989).

The degree of development of the crystal fabrics depends primarily on total strain and less on strain rate, stress or temperature (Budd & Jacka, 1989). The total strain due to the longitudinal deformation from one position to another can be estimated from the difference in surface velocity (Budd, 1972; Budd & Jacka, 1989), which is the method employed by Young & Hyland (2002). Looking at the strain rate over an ice sheet, the longitudinal strain rates may vary from positive to negative over distances of several ice thicknesses (Budd & Jacka, 1989). The surface velocity varies smoothly, reflecting average basal shear over large scales of many times ice thickness (10-20 times) (Budd & Jacka, 1989).

Surface velocities therefore provide a valuable stable indicator of the integrated shear within the ice, which consists mainly of shear in the basal zone or just above the basal zone. This has been useful in plotting the average strain rate through the ice versus basal shear stress (Budd & Jacka, 1989), as has been done for Law Dome and a summary of results is shown in Figure 7.3. The grey bands of high shear stress in Figure 7.3 could be expected to give rise to crystal anisotropy at depth in grounded ice.

Qualitative experimental evidence for the assumed flow anisotropy gives the extensional strain rate perpendicular to the compression axis as smaller in the direction parallel to the margin planes than in the direction at 45° to the marginal plane (Figure 7.4). Figure 7.5 is the cross section of an Ice Stream B in West Antarctica showing where the areas of marginal strain occur.

Shear Stress (bars)

column:	50	51	52	53	54	55	56	57	58
level									
1	0.27	-0.03	-0.48	0.21	0.24	0.23	0.19	0.13	0.13
2	0.53	0.26	-0.14	0.39	0.44	0.37	0.31	0.28	0.30
3	0.74	0.66	0.38	0.65	0.59	0.48	0.42	0.42	0.49
4	0.90	0.97	0.82	0.88	0.69	0.54	0.49	0.52	0.64
5	1.00	1.20	1.15	1.05	0.74	0.57	0.54	0.58	0.73
6	0.99	1.46	1.54	1.06	0.75	0.60	0.56	0.63	0.78
7	0.97	1.34	1.37	0.97	0.71	0.59	0.58	0.65	0.80
8	0.89	1.21	1.30	0.94	0.66	0.59	0.60	0.67	0.80
9	0.73	1.05	1.22	0.78	0.58	0.62	0.64	0.67	0.77
10	0.46	0.68	0.92	0.49	0.51	0.68	0.71	0.64	0.67

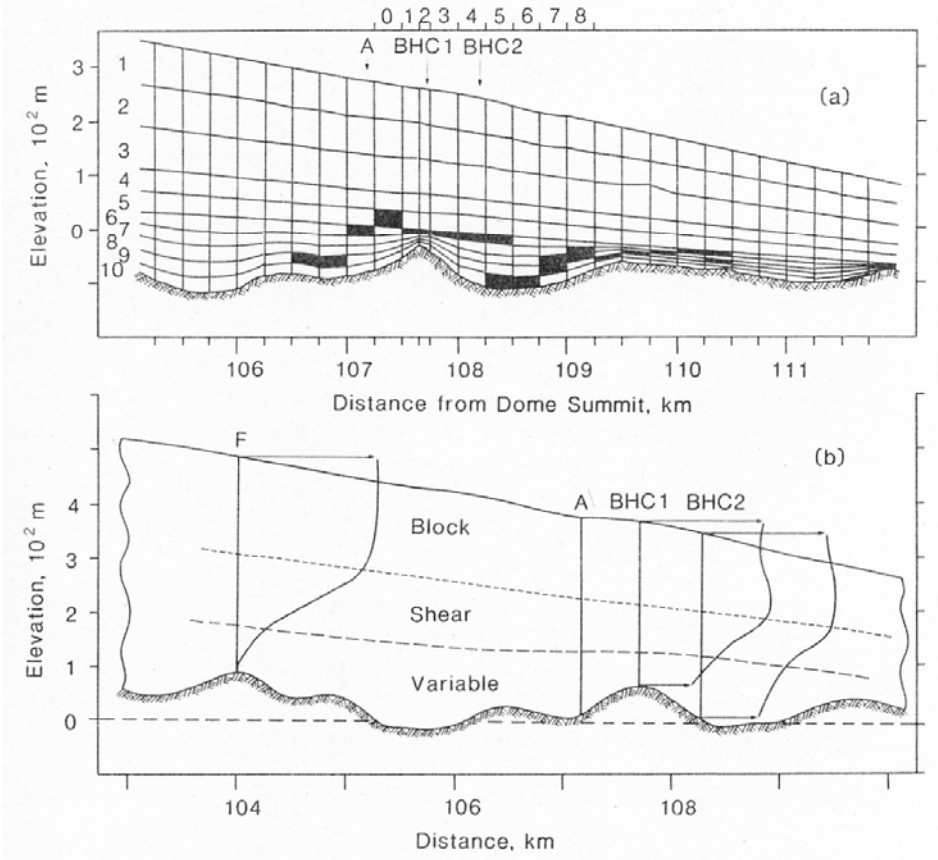

Figure 7.3 – Variable stress and strain rates in ice sheets. (a) Cross-section of Law Dome flowline towards Cape Folger (where three closely spaced borehole data sets are available) has been analysed using finite element analysis (Budd & Rowden-Rich, 1985). For isotropic ice the pattern of development of high shear stress zones is shown by the dark shading with mean values for each element given in the table in bars. The column 0-8 in (a) correspond to 50-58 in the table. (b)The observed velocity profiles (Etheridge & McCray, 1985; Russell-Head & Budd, 1979) show the relative stiff upper zone moving largely as a block over a high shear zone and a highly variable more mobile basal zone (Budd & Jacka, 1989, Fig 13).

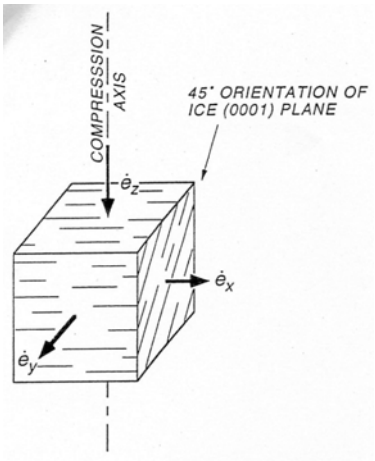

Figure 7.4 - Schematic illustration of a typical test block, with ice (0001) planes of the main maximum of the c-axis fabric dipping 45º relative to the top (z) face of the block, which is perpendicular to the compression axis. The planes of the secondary maximum, not shown, would have the same strike and would dip ~20º in the opposite direction. The strike direction is the core axis, parallel to the x-axis. The heavy arrows depict schematically the shortening strain rate parallel to the z axis ($\dot{e}_z$) and the extensional strain rates parallel to the x and y directions, $\dot{e}_x$ and $\dot{e}_y$ respectively, with $\dot{e}_x < \dot{e}_y$ (Jackson & Kamb, 1997, Fig 7).

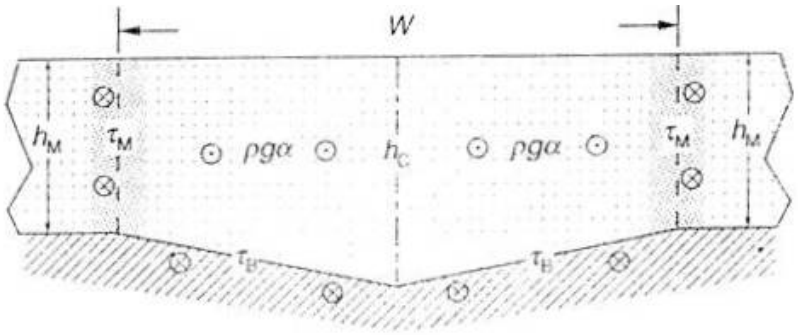

Figure 7.5 – Idealised cross section of Ice Stream B, West Antarctica (not to scale). Ice is dotted area, marginal shear zones are heavily dotted, and the bed is hatched. The ice is taken to be 1200 m thick (hc) at the centre and 900 m thick (hm) at the margins. Gravitational body force acts on ice in downstream direction, perpendicular to cross section, shown by end on "arrow heads" – circles with dot in centre. The shear stress at the bed and margins (drag stress acting upstream on the ice) are "arrow tails" – circles with cross. (Jackson & Kamb, 1997, Fig 9).

7.4 Strain rates of the Amery Ice Shelf

A map of the strain present in AIS ice has been produced by Young & Hyland (2002), using the analysis of two RADARSAT Synthetic Aperture Radar (SAR) images to produce a velocity map over the entire surface of the AIS. This technique improves upon the results of ground-based techniques for velocity determination which give accurate velocities at only discrete points on the AIS.

Two optical satellite images, or two SAR images, can be used to calculate velocity values. One technique for this is to track the displacement of surface features moving with the ice over a period of years. However this limits where you can gain velocity data to where there are visible features to track, leaving most of the ice shelf unknown. Other techniques such as an interferometry analysis of two SAR images depend on other properties, such as micro-wavelengths of snow. This technique can utilise data over short time periods, over days to weeks rather than years.

Young & Hyland (2002) used two RADARSAT SAR images from 24 days apart, collected during Antarctic Mapping Mission 24 Sep - 18 Oct 1997. Young resampled the images to give a velocity every 1 km on the surface. A precision of 1 pixel leads to an error 8 m a^{-1} along-track and 26 m a^{-1} across-track. Vertical displacement due to tidal motion becomes an apparent across-track displacement. Overall, there is a velocity average over an 8 km distance. Velocity estimates for the AIS were generated and these velocities were then used to generate the horizontal strain-rate components, resolved with respect to local flow direction. The map of strain rate over the AIS is given in Figure 7.6.

Young & Hyland (2002) describe the strain rates varying systematically across and along the AIS. The pattern of transverse shear strain rate clearly identifies shear margins, where values are greater than 0.1 a^{-1} in the southern part of the ice shelf. There are also longitudinal bands of enhanced shear strain rate containing ice with strong fabric of preferred crystal orientation caused by shear margins upstream (Young & Hyland, 2002).

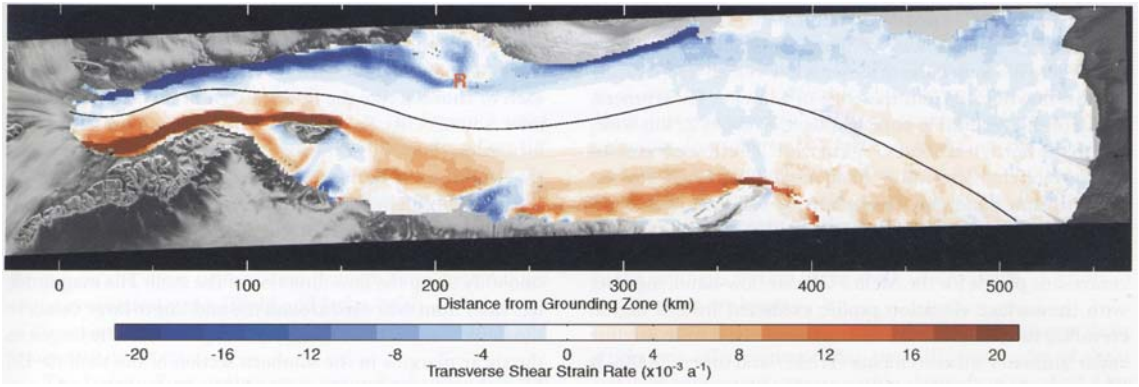

Figure 7.6 – Spatial distribution of transverse shear strain rate over the AIS, resolved with respect to flow direction (Young & Hyland, 2002, Fig 3). Colour scale has been constructed to show detail at low strain rate values, with increments selected to give a resolution above the error estimate.

Horizontal components of longitudinal and transverse strain rates and the transverse shear strain rate were produced. The value of the transverse shear strain rate (Figure 7.6) is positive (red) where velocity increases to the left looking downstream (north) – meaning the rate is typically positive on the right (eastern) side of a stream, decreasing toward the centre of the stream. Since the AIS is oriented in the along-track direction, it is implied that precisions for the longitudinal and transverse shear strain rates are better than 1×10^{-3} a^{-1} and the precision of the transverse strain rate is ~ 1-2 $\times 10^{-3}$ a^{-1}.

These strain rates, along with the geometry of the shelf, allow for a characterisation of the flow pattern, and an inference of some of its deformation properties. The transverse shear strain rate varies across the flow direction, but tends to vary slowly and smoothly along the direction of flow of the shelf. Values sometimes exceed 100×10^{-3} a^{-1} along the eastern margin of the southern part of the ice shelf. The strongest values occur in the west beside Jetty Peninsula – which is upstream of the AM01 and AM04 sites (Craven et al., 2009; Treverrow et al., 2010) – and on the east in a narrow band passing the north end of Gillock Island.

High strain values in the south imply a dissipation of energy as strain heating through the ice shelf, this raises the temperature of the core of the shear margins and results in horizontal temperature gradients out of these areas (Young & Hyland, 2002). Ice within

these margins accumulates large strains as it is carried downstream. The strain accumulated depends on the strain rate and the velocity of the ice through a strained area. In general, 20% strain is accumulated within 2-10 km, and 80% within 10-30 km. This is more than enough to establish a strong crystal fabric alignment, consistent with simple shear in a vertical plane along the margin (Budd & Jacka, 1989). With other flow bands joining the shelf further downstream, these bands of deformed ice are incorporated into the shelf and protected well away from the outer margins.

The longitudinal strain rate is significant in the northern part of the AIS, and is larger than the transverse shear strain rate in this region of the ice shelf except at the margins (Young & Hyland, 2002). Where the longitudinal strain rate starts to decrease toward the ice shelf front, the transverse shear strain rate becomes significant and increases to the front. If there is preferred crystal orientation within the central core part of the AIS, it is likely to counter rather than enhance shear deformation (Young & Hyland, 2002).

Spatial patterns of strain show evidence that two modes of shear strain occur within the AIS. One is related to the presence of ice with a strong preferred crystal orientation fabric with simple shear parallel to ice flow direction. Ice within narrow bands has been carried downstream from the origin of the shear margins where it initially developed the strong fabric (Young & Hyland, 2002). These are the areas of the ice shelf that are of interest to a seismic study for azimuthal anisotropy.

7.5 Seismic body waves and anisotropy

Body wave velocities, for both primary (P) and secondary (S) waves, are affected by anisotropy. In anisotropic media, body waves travelling in different directions produce different waves and velocities. According to an explanation given by Udias (1999), referring to the diagram in Figure 7.7, propagation in the χ_3 direction (the principle axis) leads to both P and S waves with differing velocities. When propagation occurs in the χ_1 direction, there are three different waves with three different corresponding velocities – the P wave, and two S waves. The S wave has two different displacements perpendicular to the direction of propagation, one with displacement in the χ_2 direction and the other with displacement in the χ_3 direction.

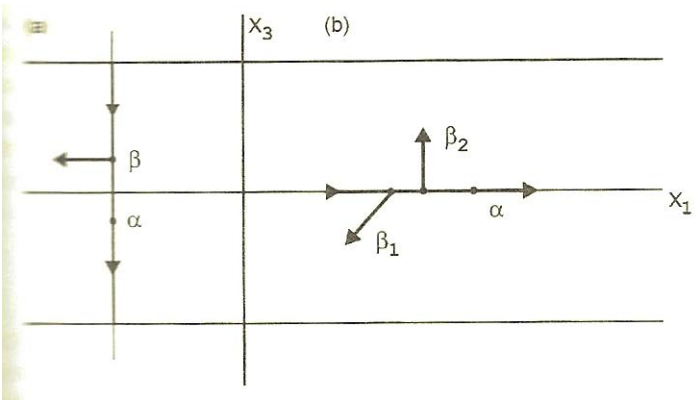

Figure 7.7 – The propagation of P (α) and S (β) waves in a medium with hexagonal symmetry and the principle axis in the χ_3 direction: (a) waves in the χ_3 direction; and (b) waves in the χ_1 direction, SH waves have velocity β_1 and SV waves have velocity β_2. (Udías, 1999)

The conclusion can be drawn that in an anisotropic medium with hexagonal symmetry, P waves propagate with different velocities along the principle axis of symmetry (χ_3) and along a direction normal to it (χ_1) (Udías, 1999). In general, for any type of anisotropy there are always three types of waves propagating with three different velocities: quasi-P, quasi-SH and quasi-SV. The velocities for the three types of waves change according to the type of symmetry present in the medium. Because of these properties, anisotropy is detected by observations of changes in P wave velocity along two perpendicular directions and by observations of S wave splitting (Bentley, 1975; Udías, 1999).

The effect this has upon measurable seismic velocities in terms of azimuth is shown in Figure 7.8. The faster velocity is in the direction of the major axis, while the slow velocity in the direction of minor axis (Yilmaz, 2001).

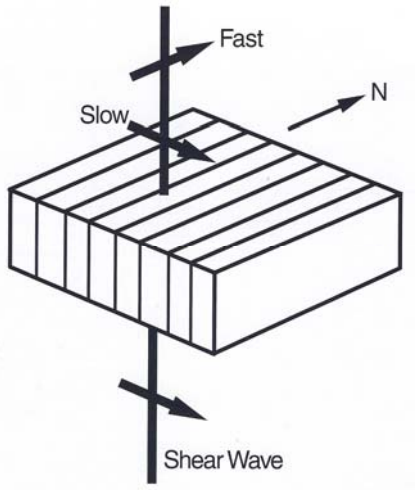

Figure 7.8 – the physical aspects of seismic wave propagation in anisotropic medium (Yilmaz, 2001, Fig 11.7-31)

7.5.1 Relating seismic P waves to crystal orientations

Correlating P wave velocity to crystal orientation, Bentley & Clough (1972) conducted measurements of ultrasonic P-wave velocity in the Byrd Station drill hole. Conducted only to a depth of 1540 m due to a blockage, this study confirmed the existence of strong vertical c-axis orientation, as shown in Figure 7.9. There is a sharp initial increase in velocity in the top 200 m of ice, due largely to the increasing ice density. After that, virtually all increase in velocity is consistent with the pattern of crystal fabric changes and transitions (Gow & Williamson, 1976). According to Figure 7.9, the seismic velocity due to anisotropy reaches a maximum of approximately 4000 ms^{-1} at ~1280 m depth where there is a strong c-axis alignment. This indicates that P wave velocity increases in anisotropic ice with a strong ice fabric orientation.

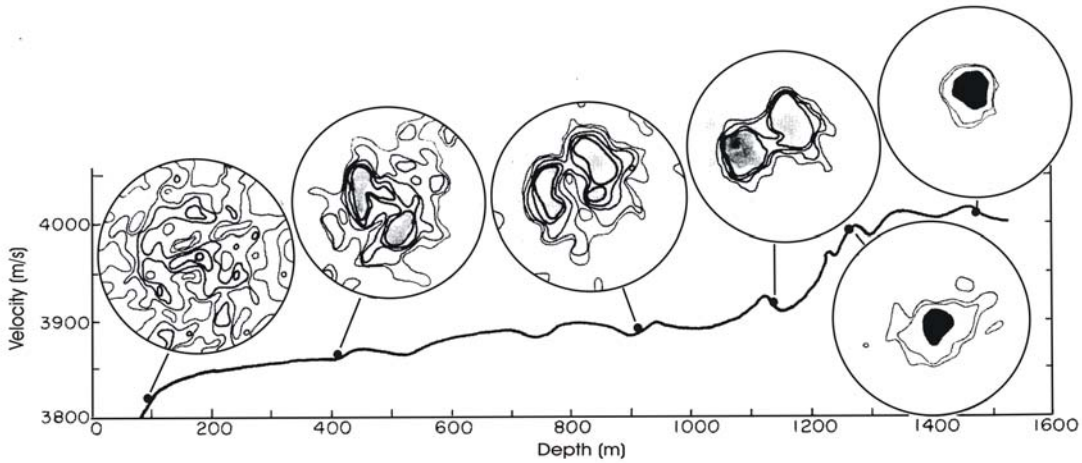

Figure 7.9 – Correlation of ice fabrics (fabric distribution as a contoured density) and P wave velocity from the Byrd Station drill hole. Peak velocity corresponds with vertical c-axis fabric (Gow & Williamson, 1976, Fig 7).

7.5.2 The P wave velocity variation in anisotropic ice

From various studies, definitions have been made of the usual velocity variation in ice. Bentley (1975) states that wave velocities vary 3.5% over the 60°C range of temperatures found in glaciers and ice sheets. The variance of velocity with temperature has been well defined by Robin (1958), while Kohnen (1974) determined the temperature coefficient for P wave velocity to be -2.30 ± 0.17 ms^{-1} degrees. However, work on the Ross Ice Shelf also suggests a P wave velocity 5% higher than what is expected for isotropic ice, but it is appropriate for propagation parallel to the *c*-axis in strongly oriented ice (Bentley, 1975).

The maximum deviation from isotropic mean is ~5% for P wave velocity (Bentley, 1975) – see Figure 7.10. This could apply to a polycrystalline region in which the *c*-axes were perfectly aligned. In reality, perfect alignment will not occur, although strongly oriented polycrystalline ice will show diminished but still detectable velocity variations in field measurements.

In the case of S waves, analysis of S-wave reflected and converted P to S waves on a wide angle profile along flow direction shows the inversely polarised S waves (SH

waves) travel 1-2% faster than waves polarised in the plane of the profile (Bentley et al., 1987). A 2% difference was also seen in the shear wave velocity of different polarisations generated by micro-earthquakes at the base of an ice stream (Bentley et al., 1987).

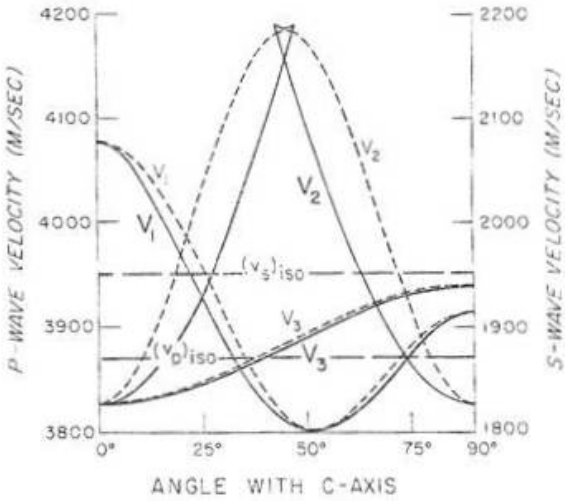

Figure 7.10 – P wave velocity curve with isotropic polycrystalline averages (Bentley, 1975, Fig 1). Phase velocities (dashed lines) and wave velocities (solid lines) in a single crystal of ice at -10°C as a function of direction of propagation. V1 = P wave; V2 = extraordinary S wave; V3 = ordinary S wave. Upper and lower horizontal line represent S-wave and P-wave velocities, respectively, in isotropic polycrystalline ice.

7.6 Amery Ice Shelf seismic anisotropy data

Refer to Section 3.2 of this thesis for an explanation and map of the anisotropy survey geometry and locations on the AIS strain map. Figure 7.11 shows all the surveys in relation to Flow Units.

7.6.1 Data processing

Figures 7.12 display an example shot record of the anisotropy refraction data collected for this survey (viewed in SeisImager Pickwin). The refraction data collected was processed using SeisImager© software, which is made up of two modules: Pickwin

version 2.85 (March 1, 2004) for data viewing and first arrival time picking, and Plotrefa version 2.67 (December 22, 2003) for layer assignment and time-term inversion. These model results gave initial model parameters for processing using Rayinv in Seismic Unix (Zelt & Smith, 1992), this allowed for velocity gradients to be applied and ray tracing to match the input models to the real data. Ray inverse trace modelling has been successfully used previously in seismic investigations of polar regions to apply step velocity-depths functions to 2D velocity models with an iterative approach to modelling (Engen et al., 2009; Schijns et al., 2009).

Models were iterated to improve the fit of the ray inverse model to the data. This methodology was chosen to allow for discrete maximum velocities to be calculated at the maximum model depths, followed by ray tracing which allows for smooth velocity gradients to be applied throughout the model and for changes in velocity gradients over different depth ranges of the model.

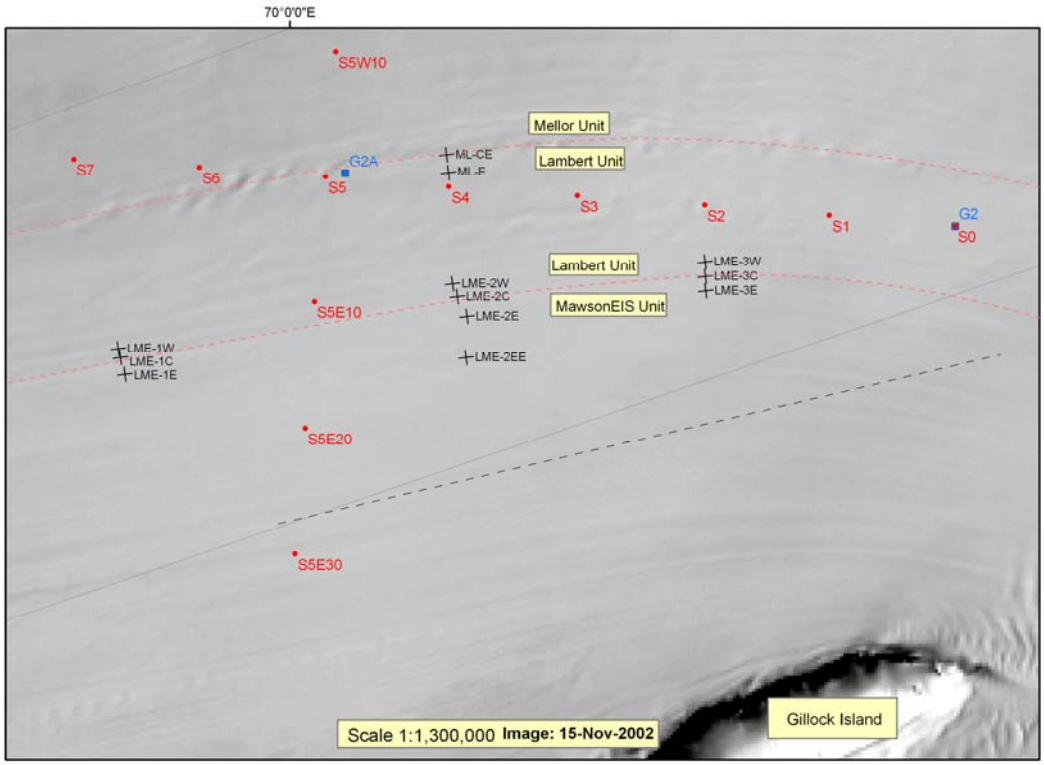

Figure 7.11 – Map of anisotropy surveys (+) and regional seismic sites with major ice boundaries shown (- - -) and the line of safe work (- - -).

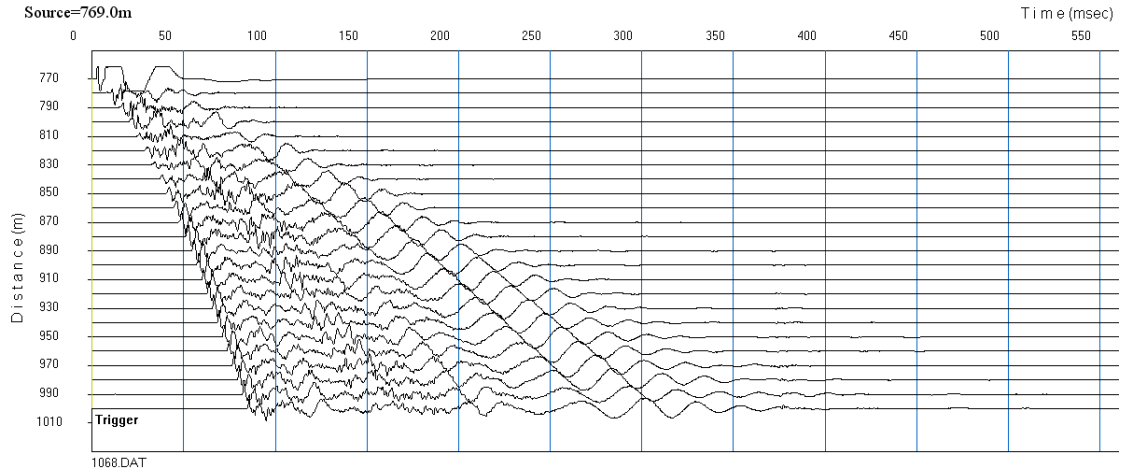

Figure 7.12 – Raw shot record from site LME-2W

7.6.2 SeisImager discrete layer models

Models were produced with three or four layers where possible. All lines could be processed with three layers, but some produced more realistic results when assigned four layers. For some lines no fourth layer could be discerned from the data.

Both three- and four-layer models have validity for representing what is happening in the shallow subsurface of the AIS. The shallow material of the ice shelf can be divided into three major layers: snow, firn (semi-compacted snow) and solid ice. The snow layer occupies the first few metres, and it quite distinct. However, it is generally not as simple for the boundary between firn and ice. The reason why a fourth layer may be interpreted in some data, and why it is acceptable, is the lack of a distinct boundary between firn and ice. In reality, this change occurs gradually with depth, as the natural process of firn compacting to solid ice. Hence there can be a velocity gradient between firn and ice as opposed to a distinct change in velocity over a small change in depth. Because of this it can be interpreted that there really is only two layers - snow and the second firn-ice layer, which has a steep velocity gradient at shallow depths. Being required to assign distinct layers then can cause a distortion of the modelled results. Using four layers if

possible helps to reduce that distortion, allowing for a greater outline of average velocity values over smaller layer thicknesses. An example of layer assignation is shown in Figure 7.13. The discrete-layer models for the same anisotropy group, LME-2, are given in Figure 7.14 and 7.15. The remainder of the discrete layer models for other anisotropy groups is included in Appendix C.

7.6.3 Ray inverse tracing models – velocity gradients applied

The data was processed in Rayinv using initial model values (layer thicknesses and velocities) gained from the SeisImager models, trialling both three and four layer models with varying gradients and depths being applied to the layers. An example ray trace for the LME-2W site is given in Figures 7.16 and 7.17 (the remainder of the Rayinv plots are included in Appendix C), showing thicknesses and upper and lower defined velocities for each layer, and the resulting ray trace comparison to the real seismic data. At LME-2 a three layer model worked best. This ray inverse trace matches the data well, and the extra benefits of this analysis include being able to apply velocity gradients, which match the reality of the ice shelf ice properties better than discrete modelling can.

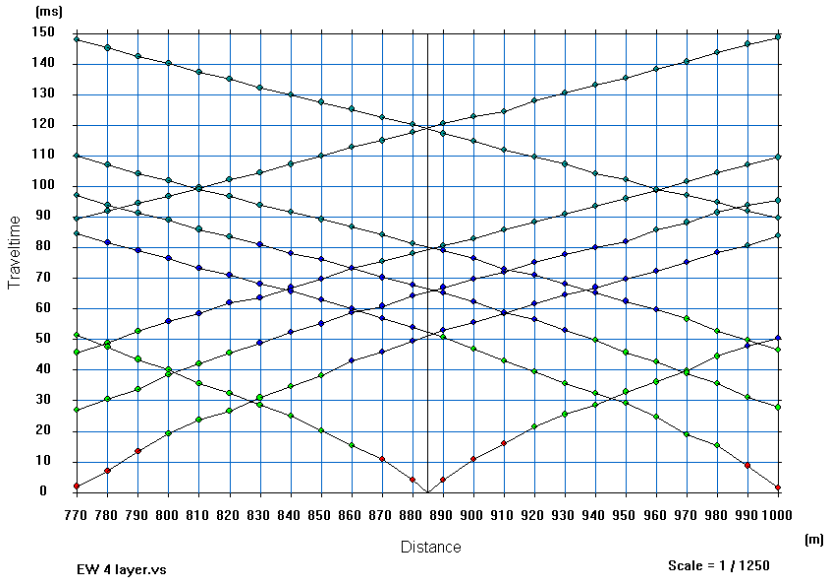

Figure 7.13 – LME-2W EW line layer assignation, showing four layers

7.6.4 Results

The SeisImager discrete layer models model the ice to a depth ~60-70 m. A summary of the SeisImager velocity results is given in Table 7.1. This gives the modelled velocities for each site's three layer model, for the EW and NS lines. Surveying for anisotropy is about measuring differences in this velocity with direction. Table 7.1 gives the changes in velocity for the same layer from EW to NS, for the same layers from the central (anisotropic?) site to the east and west sites (isotropic?) of the group.

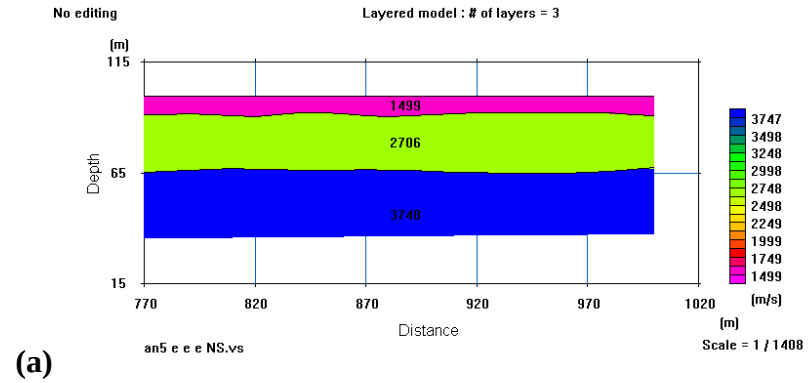

(a)

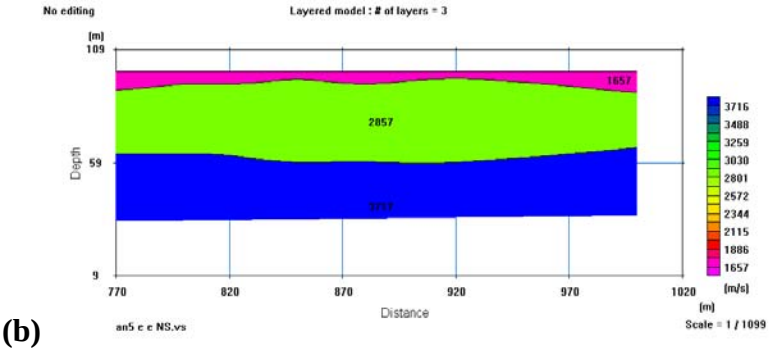

(b)

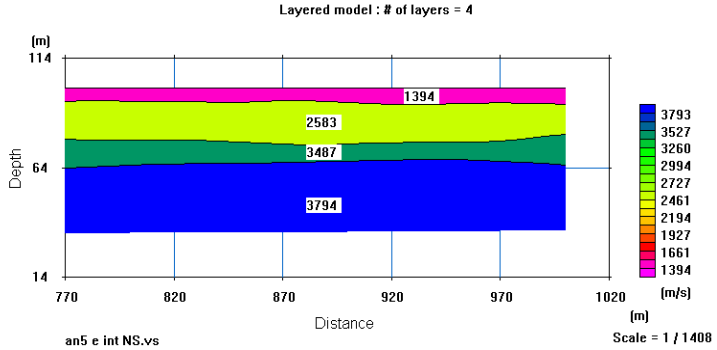

(c)

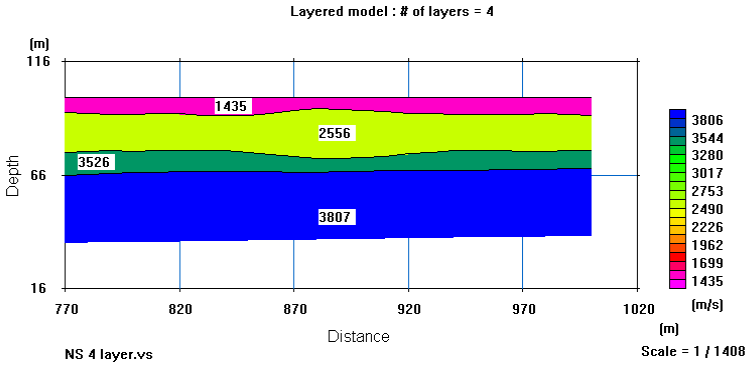

(d)

Figure 7.14 - 2D Seismic refraction profiles for the LME-2 group; NS profile lines. At locations (a) LME-2EE, (b) LME-2Ee, (c) LME-2Ct, (d) LME-2W

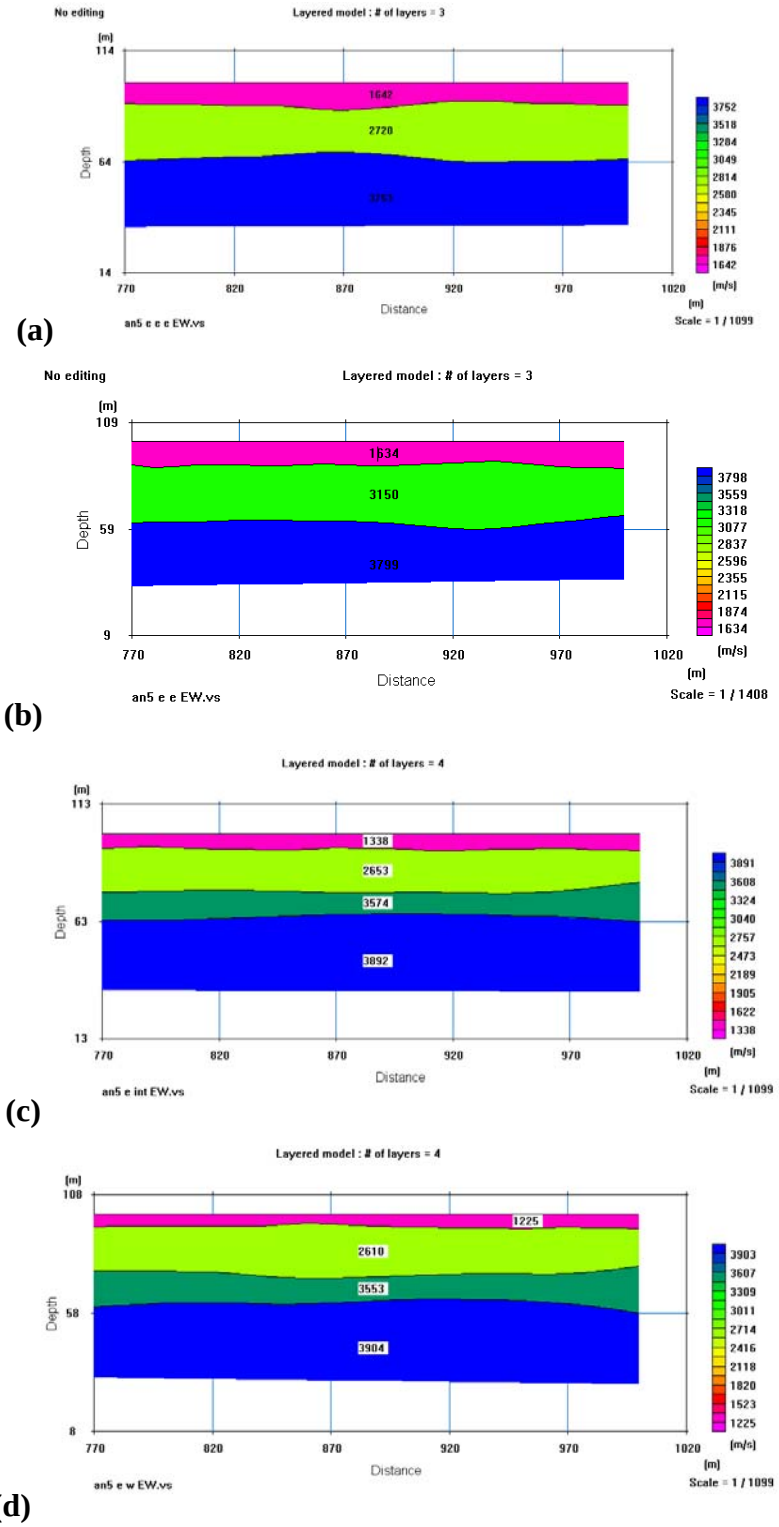

Figure 7.15 - 2D Seismic refraction profiles for the LME-2 group; EW profile lines. At locations (a) LME-2EE, (b) LME-2Ee, (c) LME-2Ct, (d) LME-2W

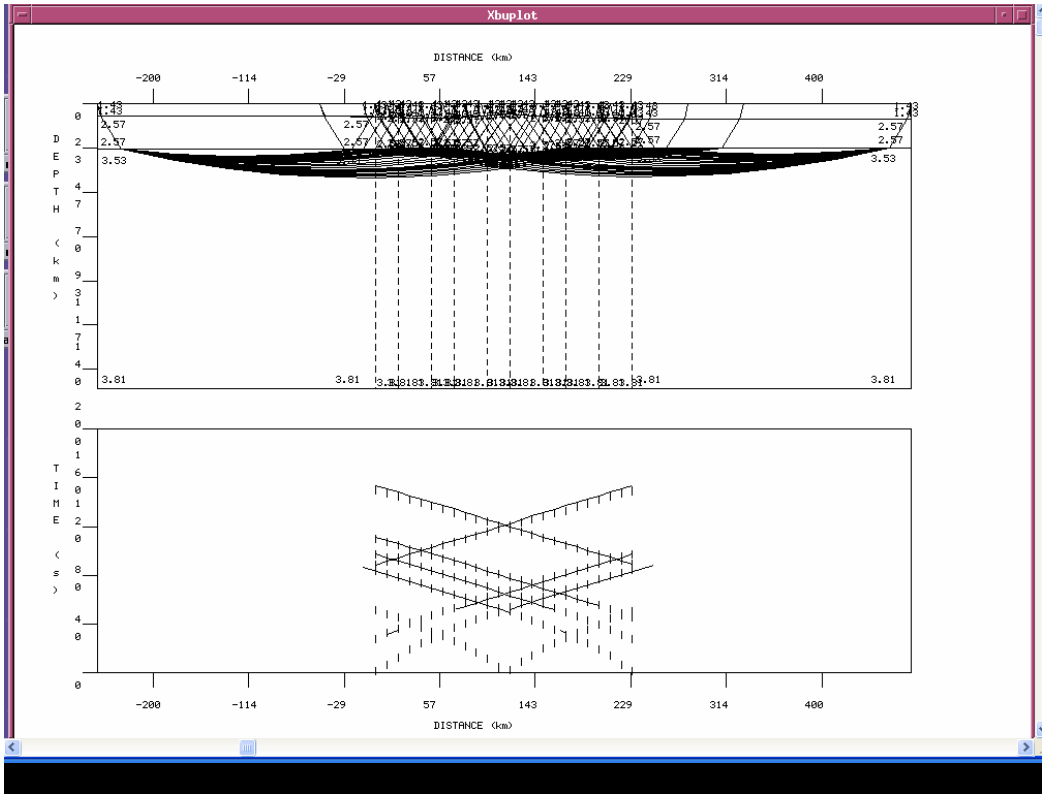

Figure 7.16 – Ray inverse tracing model for LME-2W NS line, with a three layer model. Depths are in km and velocities in km/s.

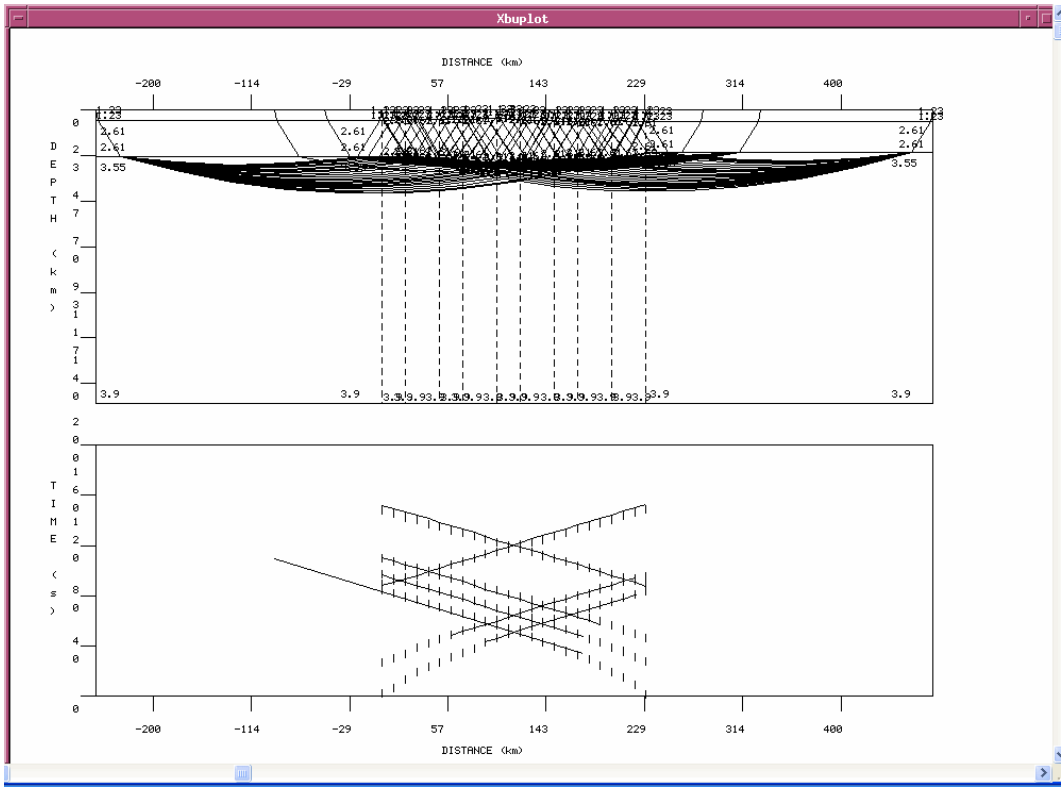

Figure 7.17 – Ray inverse tracing model for LME-2W EW line, with a three layer model. Depths are in km and velocities in km/s.

Table 7.1 – Summary of refraction P wave velocity results for all anisotropy lines, as modelled in SeisImager, errors ±100 m/s (continued on next page)

				Velocities (m/s)				Velocities (m/s)		
Line	**Latitude**	**Longitude**	**Orientation**	**layer 1**	**layer 2**	**layer 3**	**Orientation**	**layer 1**	**layer 2**	**layer 3**
LME1-E	-70.76089	70.58077	EW	1160	2972	3803	NS	1532	2751	3808
LME1-C	-70.75989	70.54394	EW	1574	2764	3870	NS	1765	3113	3727
LME1-W	-70.75932	70.52383	EW	1566	2685	3869	NS	1303	2737	3709
LME2-EE	-70.52833	70.78851	EW	1642	2720	3753	NS	1499	2706	3748
LME2-E	-70.51815	70.70628	EW	1634	3150	3799	NS	1657	2857	3717
LME2-C	-70.51991	70.65972	EW	1236	2585	3775	NS	1394	2672	3743
LME2-W	-70.52003	70.63011	EW	1128	2542	3804	NS	1425	2652	3750
LME3-E	-70.35218	70.82097	EW	1200	3100	3800	NS	1458	3112	3711
LME3-C	-70.34892	70.79228	EW	1184	2643	3711	NS	1461	2652	3704
LME3-W	-70.34551	70.76324	EW	1312	2667	3782	NS	1240	3047	3695
ML-E	-70.49647	70.40471	EW	1323	2734	3738	NS	1467	2571	3703
ML-CE	-70.49349	70.368	EW	1254	2671	3771	NS	1348	2687	3753
			Average layer velocity:	1351.1	2769.42	3789.58		1462.4	2796.4	3730.7
LME1-E			**Velocity difference to central site:**	414	-208	67		233	362	-81
LME1-C				0	0	0		0	0	0
LME1-W				8	79	1		462	376	18
LME2-EE				-406	-135	22		-105	-34	-5
LME2-E				-398	-565	-24		-263	-185	26
LME2-C				0	0	0		0	0	0
LME2-W				108	43	-29		-31	20	-7
LME3-E				-16	-457	-89		3	-460	-7
LME3-C				0	0	0		0	0	0
LME3-W				-128	-24	-71		221	-395	9
ML-E				-69	-63	33		-119	116	50
ML-CE				0	0	0		0	0	0
			Average variation in layer velocity to central site:	-41	-111	-8		33	-17	0

LME1-E	-372	221	-5	**Δ difference to central site:**	181	-570	148
LME1-C	-191	-349	143		0	0	0
LME1-W	263	-52	160		-454	-297	-17
LME2-EE	-23	293	82		-135	-380	-50
LME2-E	-158	-87	32		0	1	2
LME2-C	-297	-110	54		139	23	-22
LME2-W	143	14	5		-420	-23	2
LME3-E	-258	-12	89		-19	3	-82
LME3-C	-277	-9	7		0	1	2
LME3-W	72	-380	87		-349	371	-80
ML-E	-144	163	35		50	-179	-17
ML-CE	-94	-16	18		0	1	2
Velocity difference EW vel compared to NS vel (Δ):							
Average layer velocity difference EW to NS:	-111	-27	59				
LME1-E	-32.1	7.4	-0.1		-24.3	8.0	-0.1
LME1-C	-12.1	-12.6	3.7		-10.8	-11.2	3.8
LME1-W	16.8	-1.9	4.1		20.2	-1.9	4.3
LME2-EE	-1.4	9.3	2.2		-1.5	10.8	2.2
LME2-E	-12.8	-3.4	0.8		-9.5	-3.0	0.9
LME2-C	-26.3	-4.3	1.4		-21.3	-4.1	1.4
LME2-W	8.7	0.5	0.1		10.0	0.5	0.1
LME3-E	-21.5	-0.4	2.3		-17.7	-0.4	2.4
LME3-C	-23.4	-0.3	0.2		-19.0	-0.3	0.2
LME3-W	5.5	-14.2	2.3		5.8	-12.5	2.4
ML-E	-10.9	6.0	0.9		-9.8	6.3	0.9
ML-CE	-7.5	-0.6	0.5		-7.0	-0.6	0.5
Layer velocity difference as a % of layer velocity:							
Average % NS velocity is of EW velocity	-9.8	-1.2	1.5		-7.1	-0.7	1.6

7.7 Discussion

The maximum P wave velocity of AIS ice that has been used in this thesis for calculating the thicknesses of ice, water and seafloor depths is 3703±78 ms^{-1}. This is an average total ice thickness velocity that includes the near surface snow and firn layers velocities – these account for the top ~25±6 m or ~24±5 ms of seismic data at average measured AIS P-wave velocities of 1200±200 ms^{-1} for snow and 2690±220 ms^{-1} for firn. Comparing this average velocity to the Layer 3 velocities gained from the anisotropy refraction surveys in Table 7.1, we see three NS lines modelled almost exactly this velocity – LME-1W NS, LME-3C NS and ML-E NS. In total, 7 NS lines and 2 EW lines showed Layer 3 velocities in the low 3700s, while another 3 lines showed values 3750-3780 ms^{-1}. The LME-1 EW-oriented lines are the only group to have Layer 3 velocities all above 3800 ms^{-1}.

The averages of all lines are 3790 ms^{-1} for EW lines and 3731 ms^{-1} for NS lines. This is a difference of 59 ms^{-1} or 1.6% in P wave velocity. At sites on the Ross Ice Shelf (RIS), Robinson (1968) (cited in Bentley, 1975) found major differences in three out of four sites, with 15-20% anisotropy in the firn gross structure. The AIS anisotropy velocities for Layer 2 (~firn) range between ~3-14%.

From measurements of constants of a single ice crystal by Jona & Scherrer (1951) (cited in Robin, 1958) P-wave velocity differs by 4% along its principal axes. Bentley (1975) measured a P wave anisotropy on the Ross Ice Shelf of 5%. Since this value is for Antarctic ice shelf ice, it is the most reasonable to use to define anisotropy in the AIS ice (Layer 3).

The only measured P velocity difference > 4% is 4.3% at LME-1W. This is one of the southern-most surveys in this investigation, and as such this ice underwent strain more recently than the ice at LME-2 and LME-3 downstream. The strained ice would be preserved closer to the surface and hence more likely occur within the depth of investigation of the refraction anisotropy surveys. This is not to say that anisotropic fabric might not be present within the ice downstream of LME-1, it would just be deeper due to the continued accumulation of snow at the surface, adding to the total ice

thickness and perhaps taking the anisotropic ice deeper than what could be measured with the survey geometry that was employed. If we assume the Layer 3 P wave velocity may increase further below the ~80 m of the model, then variations in P wave velocity > 5% may be reached north of LME-1 also.

The amount of deepening of the ice from LME-1 to LME-2 and LME-3 can be estimated using the method discussed in Chapter 6 (Section 6.3.1). If we use the surface accumulation rate of 0.32 m/km then the surface ice at LME-1 would be at 9 m depth at LME-2 and 15.4 m at LME-3. The Ray inverse models for LME-1W (Appendix Figures C13 and C14) modelled the velocity from the discrete layer model to a depth of 140 m instead of the 60 m in SeisImager. If this depth increases to 69-149 m at LME-2 and ~75-155 m at LME-3, then this anisotropic ice of LME-1W may be measurable at LME-2 models at the shallowest possibility, but is definitely below the depth of investigation by LME-3.

Plotting these percentage changes on the map of the site location (Figure 7.18) gives a clearer picture of what changes are occurring. Note that as revealed in Chapter 6 of this thesis, the boundary of the Lambert-MEIS Flow Units is located between LME-2C and LME-2E.

To discuss the differences between sites, the differences in each sites EW and NS velocities, and their difference to adjacent sites' differences, may tell us more about the AIS in these locations. If we look at the Layer 3 velocity % changes for each line (refer to bottom section of Table 7.1) the differences in this velocity are from 0.1% to 4.3%, with an overall average of 1.5% difference. If we average the east, central and west sites' percentage differences (placing LME-2C in the west basket from Chapter 6 results and excluding ML sites since they are on a different ice boundary), the resulting differences are a 1.3%, 1.9%, and 2.0% change in velocity with direction. These values show that on average the west and central sites are almost identical in average azimuthal variation, and vary a little more then the velocity in the east sites. This may indicate there is a slight difference in the ice fabric of the MEIS ice as compared to the Lambert Glacier ice. This is possible, since the two units of ice are different ages and thicknesses (as shown in Chapter 6) and have undergone different strain regimes as they joined the AIS.

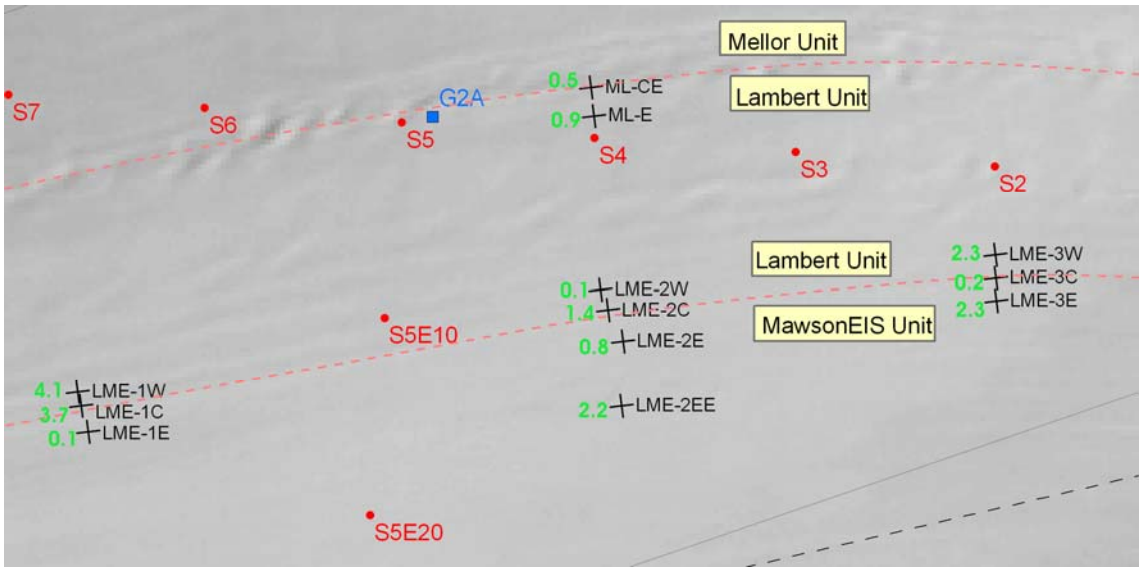

Figure 7.18 – Location of anisotropy survey sites on modis map, annotated in green the % difference between Layer 3 (solid ice) P wave velocities in the EW and NS direction (perpendicular and parallel to flow) (Distance between red regional locations is 10 km)..

If we look at the individual groups of anisotropy cross-line surveys, then the LME-3 group of sites vary oppositely to what would be expected if the centre site was anisotropic. Instead, LME-3C shows a tiny 0.2% azimuthal anisotropy whereas the west and east sites show a change of 2.3%. LME-1 shows a small difference of 0.1% for LME-1W, whereas LME1-C and LME1-E have the largest differences shown in this dataset of 3.7-4.1%. LME-2 values change from 0.1-1.4% on the west side of the ice boundary, to 1.8-2.2% on the east side.

The ML sites, only half of the group of sites that were intended to be surveyed, show a small rate of change of 0.5-0.9 %. This boundary between the Mellor and Lambert Glacier Flow Units displays a lower strain rate than the Lambert-MEIS boundary, according the model of Young & Hyland (2002). The sites were also located further from the location where the two ice streams merged into the AIS, hence any previously strained ice may be preserved deeper in the ice here, perhaps below the depth the seismic refraction data could model to. This may be true for all these refraction surveys here.

The data seems to show that sites that are closest to the boundary of the ice flow units show lower azimuthal differences in P wave velocity than other east and west sites ~1 km away. This is shown in LME-3 and LME-2 (once the actual boundary was positioned between LME-2C and LME-2E). If we line up this low trend from LME-3C to LME-2E it would be likely these would connect to LME-1E, making these locations the "closest" to the ice flow unit boundary. An explanation for why azimuthal differences in velocities are greater 1-2 km away from the boundary may be shown by Figure 7.3 and 7.5 scenarios – where the strain actually occurs a distance in from the margin rather than at the margin, be it the base of the glacier or at the margins of a moving ice stream. Perhaps as the ice units entered the AIS and merged, the zone of maximum strain was not at the boundary but at a short distance away from the boundary, and this would explain the distribution of the variance in P wave velocities.

The varying values of P wave velocity difference with azimuth may also be due to the stage of anisotropy that the ice has reached at the modelled depth of the refraction data. See Figure 7.9, the ice fabric displayed at Byrd Station in the top few hundred metres (although in a different setting to the AIS) shows no anisotropic fabric until around 400 m depth, a depth well beyond the depth of investigation of these refraction surveys. In the study by Treverrow et al. (2010), meteoric ice samples at 240 m and 255 m depth at AM01 displayed distinct fabric alignments. These fabric patterns are typically encountered below the high shear layer (Gow & Williamson, 1976; Treverrow et al., 2010), indicating a depth of ~200 m or more should be measured to gain information about anisotropy within ice. With no aligned c-axis orientation to measure at the shallower depths modelled in this investigation, the response and the % difference of the P wave velocities may be random small scale differences.

Chapter 8

CONCLUDING REMARKS

> *"To complete the story that the Amery Ice Shelf and environs have to tell us though, we need to launch other major deep field projects, for example, a full seismic survey for the true bathymetry of the southern half of the shelf." (Craven et al., 2007, p.33)*

This research aimed to undertake a multipurpose seismic study of the Amery Ice Shelf with the goal of expanding glaciological knowledge and measurements of the structure of the AIS. The results shown and discussed in this thesis show this goal has been achieved, and the knowledge gained from this study has increased our understanding of the Amery Ice Shelf - how it is formed and how it changes, what the seismic technique is capable of measuring, how these results compare to models of rates of accretion or melt such as the work of Wen et al. (2010) and the AMISOR group's findings, and what can be achieved in the future with further seismic investigation of the Amery Ice Shelf and its environs.

8.1 Key findings:

- At G2A, 3-4 reflectors occur in close succession at the base of the ice shelf. The actual reflector for the ice shelf base is the earliest faint (yet still visible) reflection. The next two reflections are stronger, and correspond to changes in water properties in the AM03 CDT data. This shows there is a cool fresh layer of water hugging the base of the ice shelf in the top 18-24 m of the water column.
- The ice thickness at G2A does not seem to have varied greatly between the seismic survey in 2002/03 and that in 2005/06, varying from 712-722 m

thickness across the surveys. Neither do the seismic results show there is an abnormal rate of melt at this location over the three years. This case study does not seem to support the proposition that global warming-affected changes in ice-ocean interaction have had a significant impact at this particular location during the period of the survey.

- The seismic P wave velocity for AIS ice shelf ice is 3703 ms^{-1}. The P wave velocity for sea water in the AIS cavity is 1452 ms^{-1} – discovered from the comparison of seismic data with AMISOR depths and CTD data.
- At AM01 and AM04 the boundary between the meteoric ice and marine ice can be observed in the seismic data, although the reflection is not strong.
- The seismic data collected in these locations revealed reflections occur at the hydraulic connection depth as opposed to at the base of the ice shelf where the marine ice layer opens up to the ocean cavity. This may be due to the randomly oriented plate crystals, which is how the marine ice accretes, or due to the absence of a seismically measurable difference between the marine ice and the sea water that flows through this permeable ice layer.
- The CT Line reveals the location of the ice shelf base boundary between the ice of the Lambert Glacier Flow Unit and the Mawson Escarpment Flow Unit, showing the MEIS Unit ice to be 15 m thinner than the Lambert Unit ice.
- The seismic data from the CT Line reveals information about water bodies under the ice shelf and possible circulation features. The upper water body was defined as ISW and measured to ~140 m below the ice shelf base; the water body below this was labelled as HSSW.
- The CT Line shows the largest seafloor variation seen in any recent seismic data, revealing a hill ~450 m to the west of the basal ice flow unit boundary. This hill may be a bathymetric expression of glacial processes from when the ice was grounded in this location.
- The refraction surveys for investigation of anisotropy have given P wave velocity parallel to the flow and perpendicular to the flow across all the surveys, showing a difference of 0.1-4.3% between these orientations.
- LME-1W is the only site that may show distinct anisotropy outside of the range of velocity errors, with the variation in velocity of 4.3%.

- The ice that the LME-1W response is gained from (at ~60 m depth in the discrete layer model) will likely occur at a greater depth (at ~70-85 m) in the ice below the downstream LME-2 and LME-3 sites, due the accumulation at the surface and subsequent deepening of the surface ice. These depths at LME-2 and LME-3 were beyond the depth of investigation using a 230 m length seismic line with maximum 250 m offset shots.
- The distribution of variations in velocity with orientation may reveal the location of strained ice at ~1-2 km away from the ice flow unit boundaries

8.2 Recommendations:

- In terms of seismic CDP investigation of the AIS, it would be advantageous to survey a location with surface seismic investigations prior to AMISOR drilling. This would gain data from exactly the same location, and over as short a period of time as possible. That way, there would not be the need to survey ~1.5 km away from the drillsite to avoid the negative effect of noise from AMISOR downhole equipment.
- It would be interesting to return and resurvey the exact same locations some years from now and see if there is a variation over a longer period of time, or at different times of the summer season – at the beginning coming out of winter compared to at the end of summer. The same location at the surface should be surveyed, and also the same ice should be surveyed – i.e. calculate where the ice that was surveyed in 2002/03, 2004/05 or 2005/06 has travelled to and survey there. This would show what changes occur in a specific section of the AIS over a period of time and also any variance in the rates of basal melt or accumulation in the area.
- In terms of the comparison of seismic data with CTD data, more calculations could be carried out with the CTD data. The shear volume of data and difficulty of the transform from CTD values to densities and P wave velocities makes this a daunting task. A logical next step would be to explore whether a script/macro can be written or has been written since this analysis was undertaken to run

these calculations in a more optimised and efficient manner to gain values for density, velocity, acoustic impedance and reflection coefficients.

- Once profiles of these properties for every AMISOR drill site were produced in the highest detail from the unaveraged data, the changes in properties of the water column for the use of seismic analysis could be mapped across the majority of the northern part of the AIS. Seismic ray tracing or seismic simulations could be run on this data to show what reflections would occur from the effect of the physical water properties only.
- The seismic data may also be investigated in terms of amplitude. This is another way of calculating acoustic impedance and reflection coefficient, and results from this line of investigation could be compared to the values calculated from CTD data. If there is a difference, then it could be discerned whether there are other factors besides water temperature and salinity that affect the observed reflections. Simulated seismic profiles from the CTD-derived reflection coefficients could be correlated with the real seismic data, and the seismic difference could be imaged.
- Hot-water drill holes produced by AMISOR (and before their moored equipment gets placed and secured down them) could be surveyed using a downhole seismic technique. This would give seismic response and properties in a continuous profile down through the AIS and would be very useful in comparing to AMISOR data and surface seismic results. For example, use of a vertical seismic profiling (VSP) tool (with a 3 component geophone) down a borehole would give information about anisotropy as well as reflection and transmission properties. This would be a good way to look at the ice shelf, and a good way to co-utilise field operations.
- Further investigation into the best processing software and processing sequence to use for AIS reflection data should be made to find what will optimise the signal in the data while removing multiples and noise
- For seismic surveys in areas of marine ice accretion, a revised survey method should be employed to increase fold coverage and increase the size of the shots to produce more energy to improve the amplitude of the reflections, that would more clearly image the meteoric-marine ice interface and the base of the ice shelf.

- The seismic technique could easily be employed in the western AIS to find the depth to the meteoric-marine ice transition and to map the depth of the hydraulic connection of the marine ice with the AIS ocean cavity water.
- For improvements in the seismic geometry and methodology employed – the AIS could and should be the site of a large-scale seismic survey expedition. The amount of data to be gained from the seismic technique supports making a concerted effort to improve the coverage and productivity of the seismic surveying. Using long towed geophone streamers with a mobile seismic recording and shot station would increase both the area and speed of coverage of the AIS surface. For difficult areas, e.g. areas with crevassing nearby, suitable vehicles/methods for safe travel should be used or suitable safe paths of travel should be outlined. Using radio geophones and setting up surveys with aerial support would overcome some problems with land access and having a safe working environment.
- With a seismic program on this scale, a greater breadth of seismic data covering the AIS from east to west and south to the grounding line would be possible. A continuous seismic survey of this kind could reveal information about the variations over/between different ice streams of the AIS, and the areas of accretion or basal melting, as well as mapping the boundary between ISW and HSSW throughout the ocean cavity.
- In terms of anisotropy investigations, again it would be beneficial to increase the scale of the seismic surveys. Deeper ice needs to be imaged, and longer refraction surveys with farther offset shots are required. This is also another situation where radio geophones would be highly useful, since the seismic cabling length limits the length of survey.
- The geometry of the anisotropy survey should be improved, with the first step to trial multiple intersecting lines at more orientations about the centre point. At least four lines at orientations 45° apart should be measured. The site for the survey should be where strained ice is more likely to occur. i.e. further east and south than this project's surveys that were carried out to investigate shear margin controlled strain, or surveying where marine ice is present (such as near AM04) to investigate anisotropy of marine ice (a vertical uniaxial compression

regime) at target depths such as 400-500 m (akin to the depths of ice fabric study by Treverrow et al. (2010)).

- A control survey with the same geometry should be carried out near the eastern front of the AIS (away from major crevassing). This would be where there is no marine ice complicating the situation, since the ice in this part of the ice shelf is mostly derived from snow that has accumulated on the shelf surface and compacted to form ice, rather than sourced from the continent where it would have undergone strain at some on the way to and way into the ice shelf. In this situation the variation of P waves at different orientations should be as random as is possible on the ice shelf.
- Another method of investigating anisotropy involves measuring the arrivals and properties of S waves rather than P waves. Some studies and trials of this could be made in conjunction with a program of P-wave investigation.

The seismic technique has proved that it is invaluable in the exploration of the Amery Ice Shelf. The CDP reflection profiles and refraction surveys have provided a wealth of information about the structure and dynamics of the AIS ice, ocean cavity and seafloor, and the value of the information is only enriched when combined with the AMISOR program of hot-water drilling, ice coring and ocean cavity investigation. Data from this seismic research has already been coupled into ice shelf-ocean models that predict the patterns of melting and freezing at the base of the shelf and the modifications to water masses circulating below the shelf (Craven et al., 2007). Further seismic investigation can undoubtedly assist in deepening our understanding of the Amery Ice Shelf system, and in answering the AAD's Ice Ocean Atmosphere and Climate program's key question of what role the Antarctic cryosphere plays in the global climate system, and how the AIS and its cavity water interact with the waters of the continental shelf and beyond.

References

ALLISON, I. (1979). The mass budget of the Lambert Glacier drainage basin, Antarctica. *Journal of Glaciology* **22**: 223-235.

ALLISON, I. (2001). Peephole through the ice: the AMISOR project. Australian Antarctic Magazine, Australian Antarctic Division. **1:** 20-21.

ALLISON, I. (2002). Why are we so interested in the Amery Ice Shelf? Australian Antarctic Magazine, Australian Antarctic Division. **3:** 27-28.

ALLISON, I. (2003). The AMISOR project: ice shelf dynamics and ice-ocean interaction of the Amery Ice Shelf. Forum for Research into Ice Shelf Processes (FRISP Report). **14**.

ANTHONI, J. F. (2000). Oceanopgraphy index. Retrieved 13/08/2011, 2011, from <http://www.seafriends.org.nz/oceano/oceans2.htm#properties>

ARMSTRONG, R. (2011). National Snow and Ice Data Center: All about glaciers. N. C. Group.

AZUMA (1999). Textures and fabrics in Dome F (Antarctica) ice core. *Annals of* ***Glaciology*****:** 163-168.

BASSIS, J., R. COLEMAN, H. A. FRICKER and J. B. MINSTER (2005) Episodic propagation of a rift on the Amery Ice Shelf, East Antarctica. Geophysical Research Letters **32**, L06502 DOI: 10.1029/2004GL022048

BAUM, S. (1997, 20/01/1997). Glossary of Oceanography and the Related Geosciences with References. Texas Centre for Climate Studies, Texas A&M University. Retrieved 13/08/2011, 2011, from http://stommel.tamu.edu/~baum/paleo/paleogloss/node4.html.

BEAUDOIN, B. C., U. S. TEN BRINK and T. A. STERN (1992). Characteristics and processing of seismic data collected on thick, floating ice: Results from the Ross Ice Shelf, Antarctica. *Geophysics* **57**(10): 1359-1372.

BENTLEY, C. R. (1975). Advances in geophysical exploration of ice sheets and glaciers. *Journal of Glaciology* **15**(73): 113-135.

BENTLEY, C. R. and J. W. CLOUGH (1972). Antarctic subglacial structure from seismic refraction measurements. Antarctic Geology and Geophysics. R. J. Adie, International Union of Geological Science**:** 683-691.

BENTLEY, C. R., S. SHABTAIE, D. D. BLANKENSHIP, S. T. ROONEY, D. G. SCHULTZ, S. ANANDAKRISHNAN and R. B. ALLEY (1987). Remote sensing of the Ross ice streams and adjacent Ross Ice Shelf, Antarctica. *Annals of Glaciology* **9**: 20-29.

BLANKENSHIP, D. D., R. M. GASSETT and C. R. BENTLEY (1982). Seismic investigations of the firn-ce structure at Dome C, East Antarctica. *Annals of Glaciology* **3**: 339 (Abstract only).

BLINDOW, N. (1994). The central part of the Filchner-Ronne Ice Shelf, Antarctica: international structure revealed by 40 MHz monopulse RES. *Annals of Glaciology* **20**: 365-371.

BUDD, W. F. (1966). The dynamics of the Amery Ice Shelf. *Journal of Glaciology* **6**(45): 335-358.

BUDD, W. F. (1972). The development of crystal orientation fabrics in moving ice. *Zeitschrift fur Gletscherkunde und Glazialgeologie* **8**(1-2): 65-105.

BUDD, W. F., M. J. CORRY and T. H. JACKA (1982). Results from the Amery Ice Shelf Project. *Annals of Glaciology* **3**: 36-41.

BUDD, W. F. and T. H. JACKA (1989). A review of ice rheology for ice sheet modelling. *Cold Regions Science and Technology* **16**: 107-144.

BUDD, W. F., I. H. LANDON-SMITH and E. WISHART, Eds. (1967). The Amery Ice Shelf. Physics of Snow and Ice. Sapporo, Japan, Institute of Low Temperature Science.

BUDD, W. F. and R. J. M. ROWDEN-RICH (1985). Finite element analysis of two-dimensional longitudinal section flow on Law Dome. *ANARE Research Notes* **28**: 153-161.

BUDD, W. F. and R. C. WARNER (1996). A computer scheme for rapid calculations of balance-flux distributions. *Annals of Glaciology* **23**: 21-27.

BULLEN, K. E. and B. A. BOLT (1985). An introduction to the theory of seismology, Cambridge University Press.

COOPER, A., H. STAGG and E. GEIST (1991). Seismic stratigraphy of Prydz Bay, Antarctica: implications from Leg 119 drilling. Proceedings of the Ocean Drilling Program, Scientific Results. J. Barron, J. Enderson, J. Baldauf and B. Larsen. **119:** 5-25.

CRARY, A. P., E. S. ROBINSON, H. F. BENNETT and W. W. BOYD (1962). Glaciological studies of the Ross Ice Shelf, Antarctica, 1957-1960. IGY Glaciological Report. New York, N.Y., IGY Data Centre A: Glaciology, American Geographical Society. **Number 6:** 43-70.

CRAVEN, M., I. ALLISON, H. A. FRICKER and R. C. WARNER (2009). Properties of a marine ice layer under the Amery Ice Shelf, East Antarctica. *Journal of Glaciology* **55**(192): 717-728.

CRAVEN, M., I. ALLISON and M. RIDDLE (2007). Fauna flourish under honeycomb ice. Australian Antarctic Magazine, Australian Antarctic Division. **12:** 32-33.

CRAVEN, M. and OTHERS (2004). Initial borehole results from the Amery Ice Shelf hot-water drilling project. *Annals of Glaciology* **39**: 531-539.

CRAVEN, M. and OTHERS (2005). Borehole imagery of meteoric and marine ice layers in the Amery Ice Shelf, East Antarctica. *Journal of Glaciology* **51**(172): 75-84.

Dictionary of Earth Science (2003). Dictionary of Earth Science. U.S.A., McGraw-Hill.

DIETRICH, G. (1963). General Oceanography: An Introduction, John Wiley & Sons.

DONG, Z. (2003). National Report of Chinese marine sciences in the southern oceans. Shanghai, Polar Research Institute of China.

DREWRY, D. J., Ed. (1983). Antarctica: Glaciological and Geophysical Folio, Scott Polar Research Institute, Cambridge.

EHRMANN, W. U. (1991). Implications of sediment composition on the southern Kerguelen Plateau for paleoclimate and depositional environment. Proceedings of the Ocean Drilling Program, Scientific Results. J. Barron, J. Enderson, J. Baldauf and B. Larsen. **119:** 185-210.

EICKEN, H., H. OERTER, W. G. MILLER and J. KIPFSTUHL (1994). Textural characteristics and impurity content of meteoric and marine ice in the Ronne Ice Shelf, Antarctica. ***Journal of Glaciology*** **40**(135): 386-39**8.**

ENGEN, Ø., J. A. GJENGEDAL, J. I. FALEIDE, Y. KRISTOFFERSEN and O. ELDHOLM (2009). Seismic stratigraphy and sediment thickness of the Nansen Basin, Arctic Ocean. *Geophysical Journal International* **176**: 805-821.

ENGLEHARDT, H. and J. DETERMANN (1987). Borehole evidence for a thick layer of basal ice in the central Ronne Ice Shelf. *Nature* **327**(6210): 318-319.

ETHERIDGE, D. M. and A. P. MCCRAY (1985). Dynamics of the Law Dome ice cap from borehole measurements. *ANARE Research Notes* **28**: 10-17.

FEDEROV, L. V., G. E. GRIKUROV, R. G. KURININ and V. N. MASOLOV (1982). Crustal structure of the Lambert Glacier from geophysical data. Antarctic Geoscience. C. Craddock, J. K. Loveless, T. L. Vierima and K. Crawford, Madison (University of Wisconsin Press)**:** 931-936.

FERRIGNO, J. G., J. L. MULLINS, J. A. STAPLETON, P. S. J. CHAVEZ, M. G. VELASCO, R. S. J. WILLIAMS, G. F. J. DELINSKI and D. A. LEAR (1996). Satellite image map of Antarctica. United States Geological Survey Miscellaneous Investigations Series Map I-2560.

FRICKER, H. A., I. ALLISON, M. CRAVEN, G. HYLAND, A. RUDDELL, N. YOUNG, R. COLEMAN, M. KING, K. KREBS and S. POPOV (2002a). Redefinition of the Amery Ice Shelf, East Antarctica, grounding zone. *Journal of Geophysical Research* **107**(B5): 2092.

FRICKER, H. A., G. HYLAND, R. COLEMAN and N. W. YOUNG (2000a). Digital elevation models for the Lambert Glacier-Amery Ice Shelf system, East Antarctica, from ERS-1 satellite radar altimetry. *Journal of Glaciology* **46**(155): 553-560.

FRICKER, H. A., S. POPOV, I. ALLISON and N. YOUNG (2001). Distribution of marine ice beneath the Amery Ice Shelf. *Geophysical Research Letters* **28**(11): 2241-2244.

FRICKER, H. A., R. C. WARNER and I. ALLISON (2000b). Mass balance of the Lambert Glacier-Amery Ice Shelf system, East Antarctica: a comparison of computed balance fluxes and measured fluxes. *Journal of Glaciology* **46**(155): 561-570.

FRICKER, H. A., N. W. YOUNG, I. ALLISON and R. COLEMAN (2002b). Iceberg calving from the Amery Ice Shelf, East Antarctica. *Annals of Glaciology* **34**: 241-246.

FRICKER, H. A., N. W. YOUNG, R. COLEMAN, J. N. BASSIS and J. B. MINSTER (2005) Multi-year monitoring of rift propagation on the Amery Ice Shelf, East Antarctica. Geophysical Research Letters **32**, L02502 DOI: 10.1029/2004GL021036

GALTON-FENZI, B. K., C. MARALDI, R. COLEMAN and J. HUNTER (2008). The cavity under the Amery Ice Shelf, East Antarctica. *Journal of Glaciology* **54**(188): 881-887.

GIOVINETTO, M. and C. R. BENTLEY (1985). Surface balance in ice drainage systems of Antarctica. *Antarctic Journal of the United States* **20**: 6-13.

GOLYNSKY, A. V., V. N. MASOLOV, V. S. VOLNUKHIN and D. A. GOLYNSKY (2006). Crustal provinces of the Prince Charles Mountains region and surrounding areas in the light of aeromagnetic data. Antarctica: Contributions to global earth sciences. IX International Symposium of Antarctic Earth Sciences 2003. D. K. Fütterer, D. Damaske, G. Kleinschmidt, H. Miller and F. Tessensohn. Potsdam, Germany, Springer-Verlag**:** 83-94.

GOW and WILLIAMSON (1976). Rheological implications of the internal structure and crystal fabrics of the West Antarctic ice sheet as revealed by deep core drilling at Byrd Station. *Geological Society of America Bulletin* **87**: 1665-1677.

HAMBREY, M. J. (1991). Structure and dynamics of the Lambert Glacier-Amery Ice Shelf system: implications for the origin of Prydz Bay sediments. Proceedings of the Ocean Drilling Program, Scientific Results. J. Barron, J. Enderson, J. Baldauf and B. Larsen. **119:** 61-74.

HAMBREY, M. J., W. U. EHRMANN and B. LARSEN (1991). Cenozoic glacial record of the Prydz Bay Continental Shelf, East Antarctica. Proceedings of the Ocean Drilling Program, Scientific Results. J. Barron, J. Enderson, J. Baldauf and B. Larsen. **119:** 77-132.

HAMBREY, M. J. and B. MCKELVEY (2000). Neogene fjordal sedimentation on the western margin of the Lambert Graben, East Antarctica. *Sedimentology* **47**: 577-607.

HEMER, M. A. and P. T. HARRIS (2003). Sediment core from beneath the Amery Ice Shelf, East Antarctica, suggests mid-Holocene ice-shelf retreat. *Geology* **31**(2): 127.

HEMER, M., J. HUNTER and R. COLEMAN (2006). Barotropic tides beneath the Amery Ice Shelf. *Journal of Geophysical Research* **111**.

HOLBROOK, W. S., P. PÁRAMO, S. PEARSE and R. W. SCHMITT (2003). Thermohaline fine structure in an oceanographic front from seismic reflection profiling. *Science* **301**: 821-824.

HOLLAND, P. R. and D. L. FELTHAM (2005). Frazil dynamics and precipitation in a water column with depth-dependent supercooling. *Journal of Fluid Mechanics* **530**: 101-124.

HUNTER, J., M. HEMER and M. CRAVEN (2004). Modeling the circulation under the Amery Ice Shelf. Forum for Research into Ice Shelf Processes (FRISP) Report No. 15**:** 67-72.

JACKSON and B. KAMB (1997). The marginal shear stress of Ice Stream B, West Antarctica. *Journal of Glaciology* **43**(145): 415-426.

JACOBS, S. S. and D. T. GEORGI (1977). Observations on the southwest Indian/Antarctic Ocean. A voyage of discovery (Deep-Sea Research). M. Angel. **24:** 43-84.

JANSSEN, V. (2009). Horizontal strain rate distribution on an active ice shelf rift from in-situ GPS data. *Journal of Global Positioning Systems* **8**(1): 6-16.

JANSSEN, V. and R. HURD (2008). Spatial Sciences on Ice: 50 years of Australian activities on the Amery Ice Shelf, East Antarctica. *Australian Geographer* **39**(4): 389-408.

JENKINS, A. and A. BOMBOSCH (1995). Modeling the effects of frazil ice crystals on the dynamics and thermodynamics of Ice Shelf Water plumes. *Journal of Geophysical Research* **100**(C4): 6967-6981.

JUN, L., T. H. JACKA and W. F. BUDD (2000). Strong single-maximum crystal fabrics developed in ice undergoing shear with unconstrained normal deformation. *Annals of Glaciology* **30**: 88-92.

KIERNAN, R. (2001). Ice sheet surface velocities along the Lambert Glacier basin traverse route. Hobart, Australia, Antarctic CRC.

KIRBY, S. H. (2007). Experimental geoscience in a freezer: Ice and icy compounds as useful educational analogues for teaching earth and planetary materials science and the physical sciences. 11th International Conference on the Physics and Chemistry of Ice, Bremerhaven, Germany, The Royal Society of Chemistry Publishing.

KOHNEN, H. (1974). The temperature dependence of seismic waves in ice. *Journal of Glaciology* **13**(67): 144-147.

KOHNEN, H. and C. R. BENTLEY (1973). Seismic refraction and reflection measurements at "Byrd" Station, Antarctica. *Journal of Glaciology* **12**(64): 101-111.

KURININ, R. G. and G. E. GRIKUROV (1977). Crustal structure of part of East Antarctica from geophysical data. Antarctic Geoscience. C. Craddock, J. K. Loveless, T. L. Vierima and K. Crawford. Madison, University of Wisconsin Press**:** 895-901.

LEFFANUE, H. and M. CRAVEN (2004). Circulation and water masses from current meter and T/S measurements at the Amery Ice Shelf. FRISP Report 15**:** 73-79.

LIMA (2010, 8/2/2010). Landsat Image Mosaic of Antarctica Project: LIMA Antarctica Overview Map. Retrieved 25/6/2011, from http://lima.usgs.gov/documents/LIMA_overview_map.pdf.

LYTHE, M. B., D. G. VAUGHAN and T. B. CONSORTIUM (2000). BEDMAP - bed topography of the Antarctic. 1:10 000 000 scale map. BAS (Misc) 9. Cambridge, British Antarctic Survey.

MANSON, R., R. COLEMAN, P. J. MORGAN and M. A. KING (2000). Ice velocities of the Lambert Glacier from static GPS observations. *Earth, Planets and Space* **52**(11): 1031-1036.

MCINTYRE, N. F. (1985). A re-assessment of the mass balance of the Lambert Glacier drainage basin, Antarctica. *Journal of Glaciology* **31**: 34-38.

MCMAHON, K. (2003). Seismic reflection studies of the Amery Ice Shelf, East Antarctica. Department of Earth and Planetary Sciences, Macquarie University, Sydney. **Honours**.

MCMAHON, K. and M. LACKIE (2006). Seismic reflection studies of the Amery Ice Shelf, East Antarctica: Delineating meteoric and marine ice. *Geophysical Journal International* **166**: 757-766.

MEIER, W. (2011). National Snow and Ice Data Centre: Sea Ice.

MIKHALSKY, E. V., J. W. SHERATON, A. A. LAIBA, R. J. TINGEY, D. E. THOST, E. N. KAMENEV and L. V. FEDEROV (2001). Geology of the Prince Charles Mountains, Antarctica, AGSO - Geoscience Australia: Canberra.

MIZUKOSHI, I., H. SUNOUCHI, T. SAKI, S. SATO and M. TANAHASHI (1986). Preliminary report of geological geophysical surveys off Amery Ice Shelf, East Antarctica. Proceedings of the Sixth Symposium on Antarctic Geosciences, 1985: National Institute for Polar Research Special Issue Japan.

MOORE, J. C., A. P. REID and J. KIPFSTUHL (1994). Microstructure and electrical properties of marine ice and its relationship to meteoric ice and sea ice. *Journal of Geophysical Research* 99(C3): 5171-5180.

MORGAN, V. I. (1972). Oxygen isotope evidence for bottom freezing on the Amery Ice Shelf. *Nature* **238**(5364): 393-394.

MORGAN, V. I. and W. F. BUDD (1975). Radio-echo sounding of the Lambert Glacier Basin. *Journal of Glaciology* **15**(73): 103-111.

MUSSETT, A. E. and M. A. KHAN (2000). Looking into the earth: An introduction to geological geophysics, Cambridge University Press.

NUNES VAZ, R. A. and G. W. LENNON (1996). Physical oceanography of the Prydz Bay region of Antarctic waters. *Deep Sea Research Part I: Oceanographic Research Papers* **43**(5): 603-641.

O'BRIEN, P. E., A. K. COOPER, C. RICHTER and A. OTHERS (2001). Proceedings of the Ocean Drilling Program, Initial reports. **188**.

PÁRAMO, P. and W. S. HOLBROOK (2005) Temperature contrasts in the water column inferred from amplitude-versus-offset of acoustic reflections. Geophysical Research Letters **32**, L24611 DOI: 10.1029/2005GL024533

PARTINGTON, K. C., W. CUDLIP, N. F. MCINTYRE and S. KING-HELE (1987). Mapping of Amery Ice Shelf, Antarctica, surface features by satellite altimetry. *Annals of Glaciology* **9**: 183-188.

PETTIT, E., E. WADDINGTON, P. JACOBSON, T. THORSTEINSSON and G. LAMOREY (2005). Anisotropy in the deep ice at Siple Dome. WAIS Workshop, Algonkian Regional Park, West Virginia U.S.A.

RAVICH, M. G., D. S. SOLOVIEV and L. V. FEDEROV (1984). Geological Structure of MacRobertson Land (East Antarctica), Washington (National Science Foundation) and New Delhi (Amerind Publishing).

RAWLINSON, N. Body Waves, Australian National University.

REN, J. W., I. ALLISON, C. D. XIAO and D. H. QIN (2002). Mass balance of the Lambert Glacier basin, East Antarctica. *Science in China Series D - Earth Sciences* **45**(9): 842-850.

ROBIN, G. D. Q. (1958). Glaciology III. Seismic shooting and related investigations. Oslo, Norsk Polarinstitutt.

ROBIN, G. D. Q. (1983). Coastal sites, Antarctica. Climatic Record in Polar Ice Sheets. G. d. Q. Robin. Cambridge, Cambridge University Press**:** 118-122.

ROSENBERG, M. (2002). AMERY ICE SHELF BOREHOLE AM01 CTD DATA, 2001/2002 SEASON - DATA PROCESSING AND QUALITY Amery Ice Shelf Experiment (AMISOR), Marine Science Cruises AU0106 and AU0207 - Oceanographic Field Measurements and Analysis Hobart, Tasmania, ACE-CRC Report: 1-119.

ROSENBERG, M. (2005). Amery Ice Shelf borehole microcat and CTD data, Season 2000/2001 to 2004/2005 - Data processing and quality. ACE CRC unpublished report, June 2005. Hobart, ACE CRC.

ROSENBERG, M. (2006). **A**MERY ICE SHELF BOREHOLE MICROCAT AND CTD DATA, 2005/2006 SEASON - DATA PROCESSING AND QUALITY. Hobart, Tasmania, ACE-CRC**:** 1-15.

RUSSELL-HEAD, D. S. and W. F. BUDD (1979). Ice sheet flow properties derived from borehole shear measurements combined with ice core studies. *Journal of Glaciology* **24**(90): 117-130.

SCHIJNS, H., S. HEINONEN, D. R. SCHMITT, P. HEIKKINEN and I. T. KUKKONEN (2009). Seismic refraction traveltime inversion for static corrections in a glactiated sheild rock environment: a case study. *Geophysical Prospecting* **57**: 997-1008.

SEA-BIRD_ELECTRONICS (2011, 23/05/2011). MicroCAT C-T (P optional) Recorder: SBE 37-IM (Inductive Modem). Retrieved 22/01/2012, from http://www.seabird.com/products/spec_sheets/37imdata.htm.

STAGG, H., D. C. RAMSAY and R. WHITWORTH (1983). Preliminary report of a marine geophysical survey between Davis and Mawson stations, 1983. Antarctic Earth Sciences, Australian Academy of Science. R. L. Oliver, P. R. James and J. B. Jago**:** 527-532.

STAGG, H. M. J. (1985). The structure and origin of Prydz Bay and MacRobertson Shelf, East Antarctica. Geophysics in the Polar Regions: Tectonophysics. E. S. Husebye, G. L. Johnson and Y. Kristoffersen. **114:** 315-340.

STODDART, M. D., (Ed.) (2008). Australia's contribution to Antarctic climate science. Australia's Antarctic Science Program, Australian Antarctic Division.

SWITHINBANK, C. W. M. (1988). Satellite Image Atlas of the World: Antarctica. U.S. Geological Survey Professional Paper 1386B, US Government Printing Office, Washington.

TASSELL, H. (2004). Seismic investigation into the ice thickness and seabed topography beneath the Amery Ice Shelf, East Antarctica. Hobart, University of Tasmania. **Honours**.

TAYLOR, J., M. J. SIEGERT, A. J. PAYNE, M. J. HAMBREY, P. E. O'BRIEN, A. K. COOPER and G. LEITCHENKOV (2004). Topographic controls on post-Oligocene changes in ice-sheet dynamics, Prydz Bay region, East Antarctica. *Geology* **32**(3): 197-200.

TINGEY, R. J. (1982). The geologic evolution of the Prince Charles Mountains - an Antarctic cratonic block. Antarctic Geoscience. C. Craddock (Ed.). Madison, University of Wisconsin Press**:** 455-464.

TREVERROW, A., R. C. WARNER, W. F. BUDD and M. CRAVEN (2010). Meteoric and marine ice crystal orientation fabrics from the Amery Ice Shelf, East Antarctica. *Journal of Glaciology* **56**(199): 877-890.

TREVERROW, A. and S. DONOGHUE (2010). Hot water drilling on the Amery Ice Shelf - an overview of the 2009-2010 AMISOR field season, Australian Antarctic Division Presentation series, June 3, 2010.

UDÍAS, A. (1999). Principles of Seismology, Cambridge University Press.

USGS, United States Geological Survey.

VAUGHAN, D. G., J. L. BAMBER, M. GIOVINETTO, J. RUSSELL and A. P. R. COOPER (1999). Reassessment of net surface mass balance in Antarctica. *Journal of Climate* **12**(4): 933-946.

WAKAHAMA, G. and W. F. BUDD (1976). Formation of the three-layered structure of the Amery Ice Shelf, Antarctica. *Journal of Glaciology* **16**(74): 295-297.

WEN, J., Y. WANG, W. WANG, K. C. JEZEK, H. LIU and I. ALLISON (2010). Basal melting and freezing under the Amery Ice Shelf, East Antarctica. *Journal of Glaciology* **56**(195): 81-90.

WHITWORTH, T. I., A. H. ORSI, S.-J. KIM, W. D. NOWLIN JR. and R. A. LOCARNINI, Eds. (1998). Water masses and mixing near the Antarctic Slope Front. Ocean, Ice, and Atmosphere: Interactions at the Antarctic Continental Margin, Antarctic Research Series. Washington DC, AGU.

WILLIAMS, M. J. M., K. GROSFELD, R. C. WARNER, R. GERDES and J. DETERMANN (2001). Ocean circulation and ice-ocean interaction beneath the Amery Ice Shelf, Antarctica. *Journal of Geophysical Research* **106**(C10): 22383-22399.

WILLIAMS, M. J. M., R. C. WARNER and W. F. BUDD (2002). Sensitivity of the Amery Ice Shelf, Antarctica, to Changes in the Climate of the Southern Ocean. *Journal of Climate* **15**(19): 2740-2757.

YABUKI, T., T. SUGA, K. HANAWA, K. MATSUOKA, H. KIWADA and T. WATANABE (2006). Possible source of the Antarctic Bottom Water in the Prydz Bay region. *Journal of Oceanography* **62**: 649-655.

YILMAZ, Ö. (2001). Seismic data analysis: Processing, inversion, and interpretation of seismic data. OK, USA, Society of Exploration Geophysicists.

YOUNG, N. W. and G. HYLAND (2002). Velocity and strain rates derived from InSAR analysis over the Lambert Glacier-Amery Ice Shelf system. *Annals of Glaciology* **34**: 228-234.

ZELT, C. A. and R. B. SMITH (1992). Seismic traveltime inversion for 2-D crustal velocity structure. *Geophysical Journal International* **108**: 16-34.

ZIMMERMAN, J., C. VETH, H. VAN AKEN, L. MAAS, H. VAN HAREN, T. GERKEMA, U. HARLANDER, F.-P. LAM, A. MANDERS, P. HOSEGOOD and A. SWART (2005, Last update: 4 April 2005). Processes near continental slopes: internal waves and mixing. Retrieved 17 November, 2010, from http://www.incois.gov.in/Tutor/IntroOc/notes/lecture10.html.

Appendix A

McMahon & Lackie (2006), Seismic reflection studies of the Amery Ice Shelf, East Antarctica: Delineating meteoric and marine ice, *Geophysical Journal International* **166**: 757-766.

Geophys. J. Int. (2006) **166,** 757–766 doi: 10.1111/j.1365-246X.2006.03043.x

Seismic reflection studies of the Amery Ice Shelf, East Antarctica: delineating meteoric and marine ice

Kathleen L. McMahon and Mark A. Lackie

Department of Earth and Planetary Sciences, Macquarie University, North Ryde, NSW, 2109 *Australia. E-mail: kmcmahon@els.mq.edu.au*

Accepted 2006 April 20. Received 2006 April 11; in original form 2004 November 15

SUMMARY

A detailed seismic reflection survey has been performed, utilizing a 24-channel spread with a 10 m geophone spacing, giving a maximum fold coverage of six, with the aim of revealing a detailed view of the subsurface structure of the Amery Ice Shelf, showing meteoric and marine ice thicknesses, water column thickness and sediment structure. The survey has successfully delineated the subhorizontal meteoric and marine ice layers, with average thicknesses of 754 and 20 m, respectively. The water column is 595 m thick, placing the seafloor at a depth of 1369 m below the ice surface. A 55 m thick, subhorizontally layered sedimentary unit can be seen, below which are deep features, at approximately 2225 m below the surface. These features could reveal the presence of dykes, a broken bedrock surface or glaciologically derived clasts that are sufficiently large enough to show up within the data.

Key words: Amery Ice Shelf, East Antarctica, ice shelf, marine ice, reflection seismology, refraction seismology.

INTRODUCTION

The Amery Ice Shelf (AIS) is located on the east coast of Antarctica, at approximately 70°S, 70°E (Fig. 1). It is the third largest embayed shelf in Antarctica, and the largest in East Antarctica (Allison 2003), and as such is one of the largest glacier drainage basins in the world. Due to this, and its thermal isolation, the AIS plays an important role in the global climate system (Allison 2003; Passchier *et al.* 2003). Knowing the structure of the AIS is important to studies of the impact of global warming on present-day ice shelves and the subsequent effect on global ocean circulation and climate (Allison 2003; Hemer & Harris 2003; Passchier *et al.* 2003). Understanding the structure of the AIS can also provide tighter control in mass balance calculations of the shelf and in ocean circulation models beneath the ice cover.

To date, the bathymetry, and hence the water column thickness, under the ice shelf is poorly known. What limited information there is available comes from about 80 seismic observations taken by the Soviet Antarctic Expedition (SAE) in the 1970s, none of these being taken south of 71°35′S (Hunter *et al.* 2004; Allison 2003). These gave the earliest indications of the depth of the ocean floor (Allison 2003), and presumably this Russian data has been used to help produce the bathymetry image and vertical section of the AIS as displayed in Hunter *et al.* (2004).

More recently, airborne ice radar data have been collected over the shelf (Allison 2003), but the results for these surveys are limited. Marine ice thicknesses for the AIS have been calculated using a digital elevation model (DEM) and airborne radio-echo soundings (RESs), assuming hydrostatic equilibrium for the shelf (Fricker *et al.* 2001). Due to the high absorption of electromagnetic energy by marine ice, ice radar will not penetrate into it (Blindow 1994), and hence ice radar is only useful to map the thickness of meteoric ice. Two ice cores have been taken on the front of the shelf as part of the Amery Ice Shelf Ocean Research (AMISOR) project (Craven *et al.* 2003), a project which aims to quantify the interaction between the ocean and the AIS, to determine the implications of this for the discharge of grounded ice and water mass modification, and to derive the long time record of the variability of this interaction (Allison 2003). The ice-radar method is based on indirect observations/data, and the hot-water drilling takes one expeditionary season to complete a single hole, since drilling through the ice shelf is only one step of a series of experiments they undertake. In reality, another quick, direct surveying technique is required to accurately map sections of the AIS.

The seismic geophysical technique is a powerful tool for surveying the thickness and structure of the subsurface, and this makes it suitable for the investigation of the structure of the AIS. A vast amount of data can be relatively quickly acquired, to reveal a complete picture of the subsurface in terms of ice, water and sediments.

Using seismic refraction and a detailed reflection survey, the main aim of the study was to map the thickness of both the ice and water column, hence depth to the seafloor, and most importantly to see if a delineation could be made between meteoric and marine ice. Meteoric and marine ice have different physical properties, such as density and elastic properties, meaning a seismic survey, if detailed enough, should be able to delineate the two boundaries. Such a survey may also reveal structure within the sediments, adding to knowledge of possible seafloor processes.

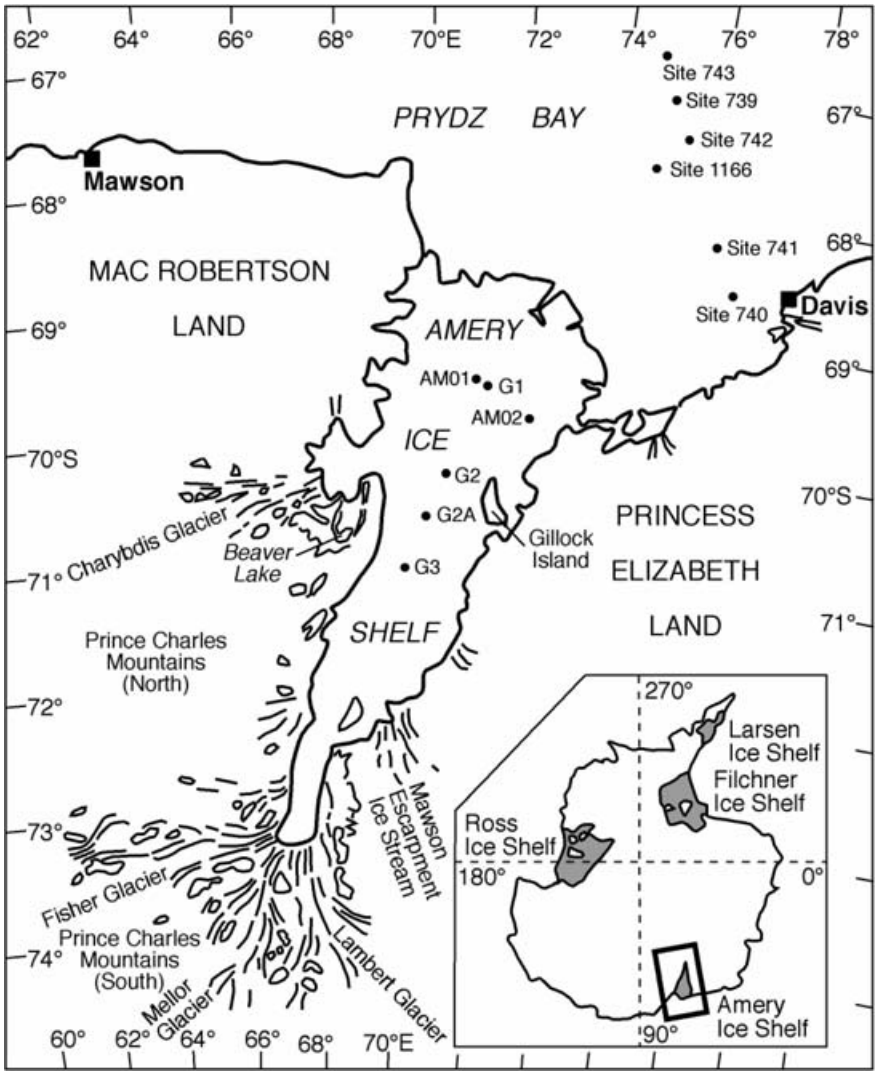

Figure 1. Map of the Amery Ice Shelf, East Antarctica. Inset: Map of Antarctica showing the major ice shelves.

GLACIOLOGY

The AIS is formed from the convergence of the Lambert, Mellor, Fisher and Charybdis Glaciers, and the Mawson Escarpment Ice Stream (Fig. 1). It extends for approximately 550 km north of its grounding zone at 73.2°S (Fricker *et al.* 2002), and is bounded by the Prince Charles Mountains (PCMs), draining through the Lambert Graben, and emptying into Prydz Bay. The Lambert Glacier drainage basin is quite well defined by ice surface contouring. Flowlines that determine the surface slope were obtained using RES (Drewry 1983), showing the ice funnelling into the Lambert Graben.

The Lambert Graben is quite well defined by both seismic (Stagg 1985; Federov *et al.* 1982) and magnetic (Federov *et al.* 1982) data. It is about 100 km wide and extends south for approximately 700 km, displaying a bedrock relief of up to 3500 m, which is mainly overlain by ice (Federov *et al.* 1982). Magnetic data shows depressions in the basement, up to 5 km in depth, filled with nonmagnetic rocks.

Ice thickness is variable and tends to smooth the underlying topography (Hambrey 1991). Ice is thinnest at the coast, with a thickness less than 500 m and some areas of bare rock being exposed. It is also thin in areas of higher elevation, such as the PCMs, where rock is exposed as nunataks. In the Lambert Graben below the Mawson Escarpment ice is 2500 m thick, the thickness decreasing with distance north to about 900 m at the AIS's grounding line and 270 m at the shelf front. In all other areas, the ice becomes thicker inland to a maximum of about 3000–3500 m at the margins of the drainage basin.

The topography of the floor of Prydz Bay is characterized by a deepening coastward from about 500 m at the continental shelf break to over 1000 m in some places near the coast, forming what is known as the Amery Basin (Hambrey 1991). This is also known as the Amery Depression (Phil O'Brien, private communication, 2005), being a depression which sits on top of the Prydz Bay Basin, a sedimentary basin. From the front of the AIS, the Amery Basin deepens progressively to the south under the ice shelf and the Lambert Glacier, reaching a depth of at least 2500 m below sea level (Hambrey 1991).

Previous glaciological research sites where detailed data were acquired on the AIS are G1 (69.5°S, 71.5°E) about 60 km from the shelf front, G2 and G3 (Fig. 1). At these sites, ice cores, density and temperature data, as well as ice velocity measurements were collected and ice thickness was found using radar (Allison 2003).

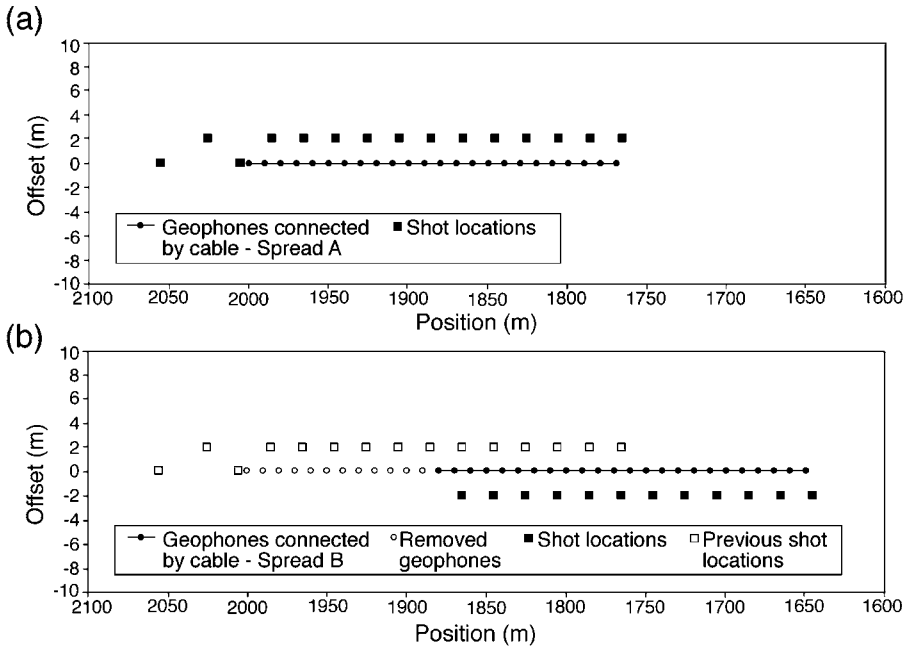

Figure 2. Method employed for shifting the reflection survey: (a) Geometry of the first spread (south end of line); (b) Geometry of the second spread. Seven of these overlapping spreads were surveyed in total. The orientation of the line was 083° magnetic.

GEOLOGY

In MacRobertson Land and Princess Elizabeth Land (Fig. 1) nearby the AIS, exposed rock are widespread in the PCMs. Geochronological investigations by Australian geologists suggested lower grade rocks exposed in the southern PCMs to be of Archaean age and the highest grade rocks to be of late Proterozoic age (Tingey 1982).

The Archaean crystalline basement underlies an area of about 130 000 km^2 of the AIS–PCM region, and is up to 20 km thick (Ravich & Federov 1977). Proterozoic metasedimentary rocks occupy an area approximately 200 km by 100 km in the southern PCMs, with a thickness of 7 to 8 km (Tingey 1972).

After the Early Palaeozoic Pan-African orogeny (Mikhalsky *et al.* 2001), tectonic activity in the area was dominated by crustal-block movement, resulting in a longitudinal system of horsts and narrow depressions. One of these is the Beaver Lake graben, where Permian coal-bearing, flat lying deposits are preserved. They directly overly the strongly eroded crystalline basement (Ravich 1974), having a total area of outcrop of 450 km^2 (Hambrey 1991) and an observable thickness of 1300 m (Ravich & Federov 1977). Despite the relatively small outcrop of Permian and younger rocks, Hambrey (1991) believed much of the AIS region is underlain by such sediments, especially in the complex Lambert Graben structure under the Lambert Glacier–AIS system.

METHODOLOGY

The surveys were carried out near G2A (Fig. 1) in the middle of the AIS, the southern-most geophone of the line being located at 70°33.5′S, 70°20.6′E. A 24-channel spread was used with a 10 m geophone spacing, the line oriented at bearing 083° magnetic (010° true), to orientate the line approximately parallel to the direction of flow. A Geometrics Strataview R48 seismograph was used, located at the centre of the spread. Groups of four 14 Hz geophones were used for every channel, to improve the signal-to-noise ratio (SNR). These were placed in ∼30 cm deep holes to keep them out of the wind and snow drift, and were spaced up to 10 cm apart, in the cross-line direction. For the reflection survey, the source consisted of two Pentex H boosters (150 g) and a single Nobel 35 g primer. The source depth was 2 m, which was cored using a Polar Ice Coring Office (PICO) corer. For the refraction survey, the exterior shots utilized a Nobel 35 g primer and the centre shot an Orica No 8 electrical detonator. The source depth was 1 m for the primers and 10 cm for the detonators.

Refraction survey

This survey was carried out to detail the shallow surface structure and to find a seismic velocity for ice near the surface. Two refraction surveys were completed at the southern and northern ends of the detailed reflection survey line. Shot locations for the refraction surveys were at 25 m and 1 m exterior to the line, and also a central shot. All were on-line with the spread, using an explosive source.

Reflection survey

The detailed reflection line was surveyed in between and inclusive of the refraction lines. We could not perform a roll-along reflection survey, since we did not have suitable cables, so to overcome these limitations, geophone spreads were moved in sections to maintain fold coverage, maximum six, over the entire line. Walk on shots were taken at 55, 25 and 5 m exterior to the spread, and interior shots were taken every 20 m (Fig. 2a). The 25 m exterior shot was offset 2 m since that online location had already been used for a refraction shot. The spread was moved north by 12 geophones so that the new Channel 1 was at the old Channel 13 location (Fig. 2b). Shots needed to be repeated at the same locations, so for different spreads shots were offset 2 m alternatively to the east or west of the line. In total, seven spreads were completed. Using this method, 89 shots were taken in total to cover a line distance 1.06 km.

PROCESSING

Refraction data were processed using the Seismic Refraction Interpretation Programs (SIP) v4.1 (Rimrock Geophysics) and RAYINVR (Zelt & Smith 1992) programs. A three-layer model was plotted to represent snow, semi-compacted snow and ice. Reflection data were processed using two software packages—Seismic Unix (SU) (Colorado School of Mines) and GLOBE Claritas© v3.3.0 (Claritas©) (New Zealand Institute for Geological and Nuclear Sciences).

The raw reflection data were of an overall good quality, with high-amplitude refraction data dominating the upper part of the records, persisting until approximately 400 ms in the data. All reflections appear as approximately horizontal reflections, arriving at approximately 400, 800, 1250, 1650 and 2030 ms.

The data were first converted to SU seg-y format then to Claritas© seg-y format. All 89 shot records were formed into a single file and field geometry was applied. Data quality was improved by trace editing, including front muting to remove refracted arrivals, and trace deletion to remove individual noise traces. Ranges of maximum frequency gained from performing a spectral analysis were used to construct a bandpass frequency domain filter to remove high-frequency noise.

A preliminary velocity analysis gave a velocity of 2500 m s^{-1} for a pre-stack NMO correction. The data were then sorted according to common depth point (CDP) number (numbered 100–301 going from south to north), and the CDP geometry file was applied. The CDP sorted data were then stacked. True stacking velocities (using a simple three-layer model representing ice, water and sediments) were found to be 3300 m s^{-1} for the ice/water reflection set and 3080 m s^{-1} for the water/sediment reflection set. Automatic gain control (AGC) and balancing were performed on the data, however, they produced no improvement in the data, and in the case of the AGC, made interpretation more difficult, and so neither were used for the final stack.

RESULTS

Refraction

The refraction data revealed a three-layer structure of snow, semi-compacted snow (firn) and ice. An example of a SIP time–depth conversion model from the refraction data is shown in Fig. 3(a). The surface snow layer varied from 3–5 m thick and the firn displayed a variable thickness, but had an average of about 20 m. This variability of the firn/ice boundary may be due to the change not being such a definite boundary, but more gradational. The average seismic velocity of the ice layer taken from nearby surface refraction surveys is 3545 $\pm$ 158 m s^{-1}, and the highest measured value is 3710 m s^{-1}. When a model with a gradational increase in density (and hence seismic velocity) of the firn layer is undertaken using ray tracing (Fig. 3b), then the thickness of the firn layer is about 40 m with a seismic velocity increasing from $\sim$2100 m s^{-1} at the top of the layer to $\sim$3700 m s^{-1} at the bottom.

Reflection

The stacked reflection data (Fig. 4a) clearly show two major reflection sets. The first shows two definite reflections at 397 ms and 404–411 ms, with multiples of these occurring at 390 ms intervals. The upper reflector can be interpreted as the base of the meteoric ice, and the lower reflector as the base of the marine ice (Fig. 4b). The thickness in two-way time (TWT) of the marine ice layer becomes 12 ms at CDP 100, decreasing to 7 ms between CDP 125 and 301. The time difference locally increases to about 10 ms around CDP 175.

The second reflection set is from the water/sediment boundary. The sediments show at least four persistent reflection boundaries, starting at approximately 1240, 1276, 1306 and 1337 ms taken from the reflection times at CDP 100. The earliest reflection time in the record for the first sediment reflection is 1227 ms. This reflection set has multiples at 387 ms intervals down the record (Fig. 4a). The primary sediment reflection boundaries all occur at $\sim$30 ms intervals, which implies that the lower three reflections are more likely reverberations from internal reflections than true primary reflections, meaning they are intrabed multiples. The reverberations appear to be exact copies of the first arrival sediment reflection. The duration of the true primary sediment reflection within the record is, therefore, 26 ms.

Well below the sedimentary layering in the stack, discrete hyperbolic reflections can be seen (Fig. 4a). Referring to these hyperbolae by the CDP number of their uppermost point, the five hyperbolae occur at CDP 107, 130, 137, 225 and 267. The earliest arrival is 1679 ms at CDP 107, and the latest is 1955 ms at CDP 225.

DISCUSSION

The seismic data shows two major reflection sets; the ice/water boundary and the water/sediment boundary. There are two reflections in the ice/water boundary; the upper reflection is interpreted as the base of the meteoric ice, and the lower as the base of the marine ice.

The ice/water boundary reflections seem similar in the record, both in time arrival and the time difference between them. This leads to the question of whether the lower reflection is simply a ghost from the free surface of the upper reflection. Hand picking the times for the meteoric/marine–ice boundary and the marine–ice/water boundary shows that the two reflections are parallel for 46 per cent of the CDP values and show inverse (reverse polarity) characteristics for 54 per cent of the CDP traces. Assuming a ghost would turn up as a reflection of reverse polarity, this would show that the entire reflection is not a ghost. Time differences in the parts of the gather that show reverse polarity are not constant, compared within or between these areas of reverse polarity. Since all shot depths were the same, this also does not concur with ghosting. If the second reflection was a ghost, it would be expected the average of the arrival times be a straight line between the two. This is not the case, and so the second reflection by all indications seems to be a true reflection and not simply a ghost of the first.

Refraction surveys at the ends of the detailed line give velocities for the top 3 m of snow of 851 $\pm$ 19 m s^{-1} for the south end, and 1094 $\pm$ 288 m s^{-1} for the north. Taking account of errors, the maximum range of velocity for snow on the line is 806–1382 m s^{-1}. Similar velocities were also found from refraction lines surveyed 500 m to the south of the detailed line. Over a distance of 2 m for a shot, these velocities for snow would add a time delay of 2.8–4.8 ms to the reflection arrival. For a depth of 2.5 m (the maximum shot-depth possible) the time delay added is 3.6–6.2 ms. With the measured time difference between the first and second reflection generally being 7–13 ms, and the average being 9.8 ms, these calculated delay times are well below what is seen in the data. If we use this actual time difference of 9.8 ms with the known shot depth to calculate a

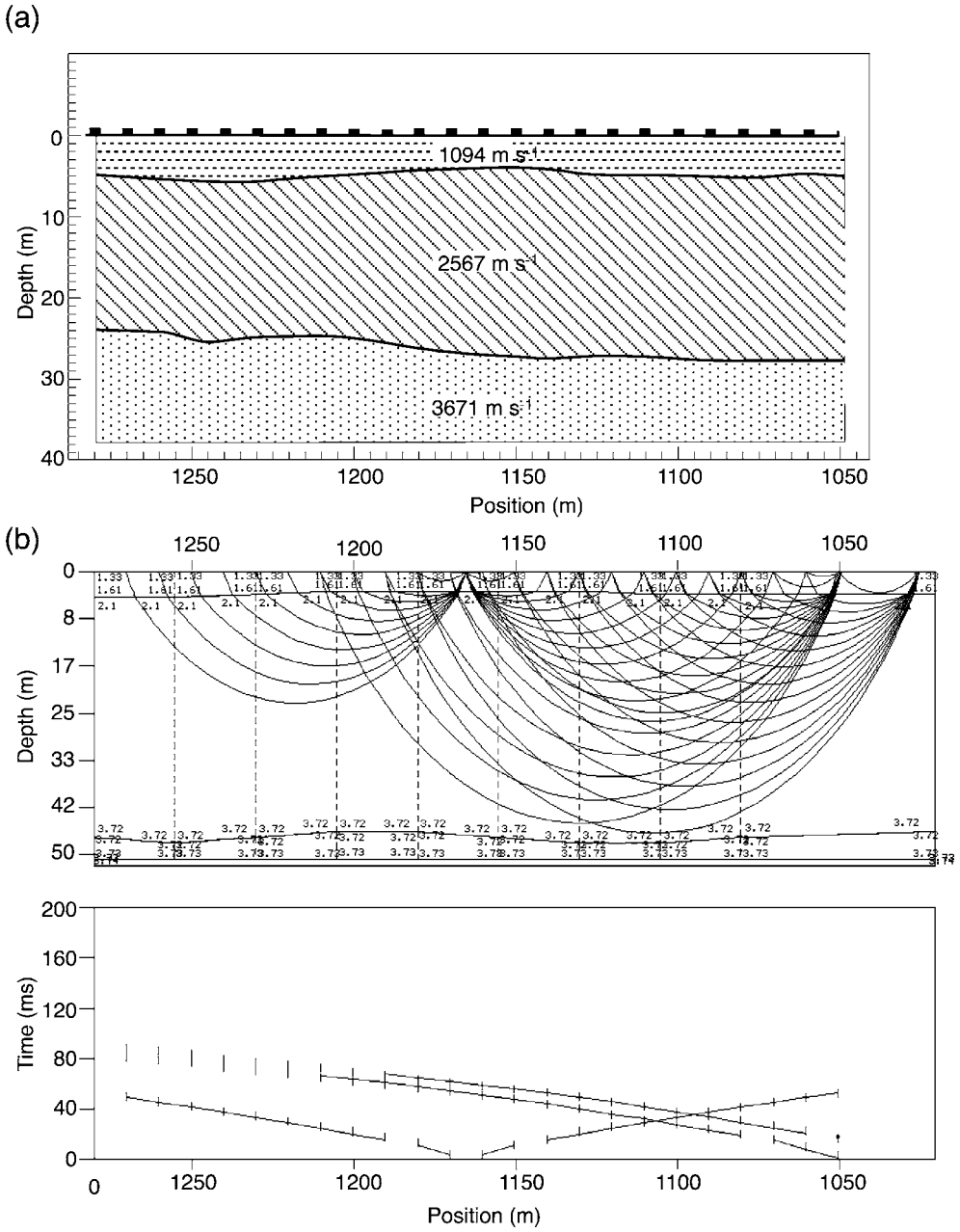

Figure 3. (a) Time–depth conversion of the refraction data from the northern end of the detailed reflection line. Geophone locations are shown on the top of the image. Velocities are given within the layers in m s^{-1}. (b) Inverse ray-tracing model of the same line. Internal upper and lower boundary velocities are given in km s^{-1}.

velocity, the velocity of the surface layer would have to be as low as 408–510 m s^{-1} for the signal to be a ghost, which is below the lowest velocities found from refraction processing of all data in the area. All this suggests the reflections are not ghosting, but actual reflections of two definable boundaries.

In order to compare these results with previous studies, the arrival times of reflections were converted into depths (Fig. 5). Reasonable near-surface seismic ice velocities were gained from the seismic refraction data. Seismic ice velocities can also be calculated using the density and temperature of the ice (Robin 1958, cited in Thiel & Ostenso 1961). The closest density and temperature readings of the ice shelf is at G1, located about 130 km downstream (to the north) of G2A, where temperature and density profiles have been taken (Budd *et al.* 1982; Mike Craven, private communication, 2003). In other Antarctic ice shelves, seismic ice velocities have also been calculated, for example, the maximum velocity of ice of the Ross Ice Shelf (RIS) is 3839 m s^{-1} (Thiel & Ostenso 1961). Considering the calculations from density and temperature, and the refraction results, a seismic velocity that could represent the entire ice layer is 3800 m s^{-1}. This was used to calculate the thickness of both the glacial and marine ice, with a maximum error of $\pm$ 50 m s^{-1} in the velocity. The error of picks for the time arrivals is up to 2 ms. However, this is the maximum error, and in most cases the arrivals could be picked to within 0.5 ms accuracy. The thickness of the meteoric ice, therefore, is 754 $\pm$ 4 m, and the marine ice varies from 13–27 m thick, with an error in the range 4–8 m.

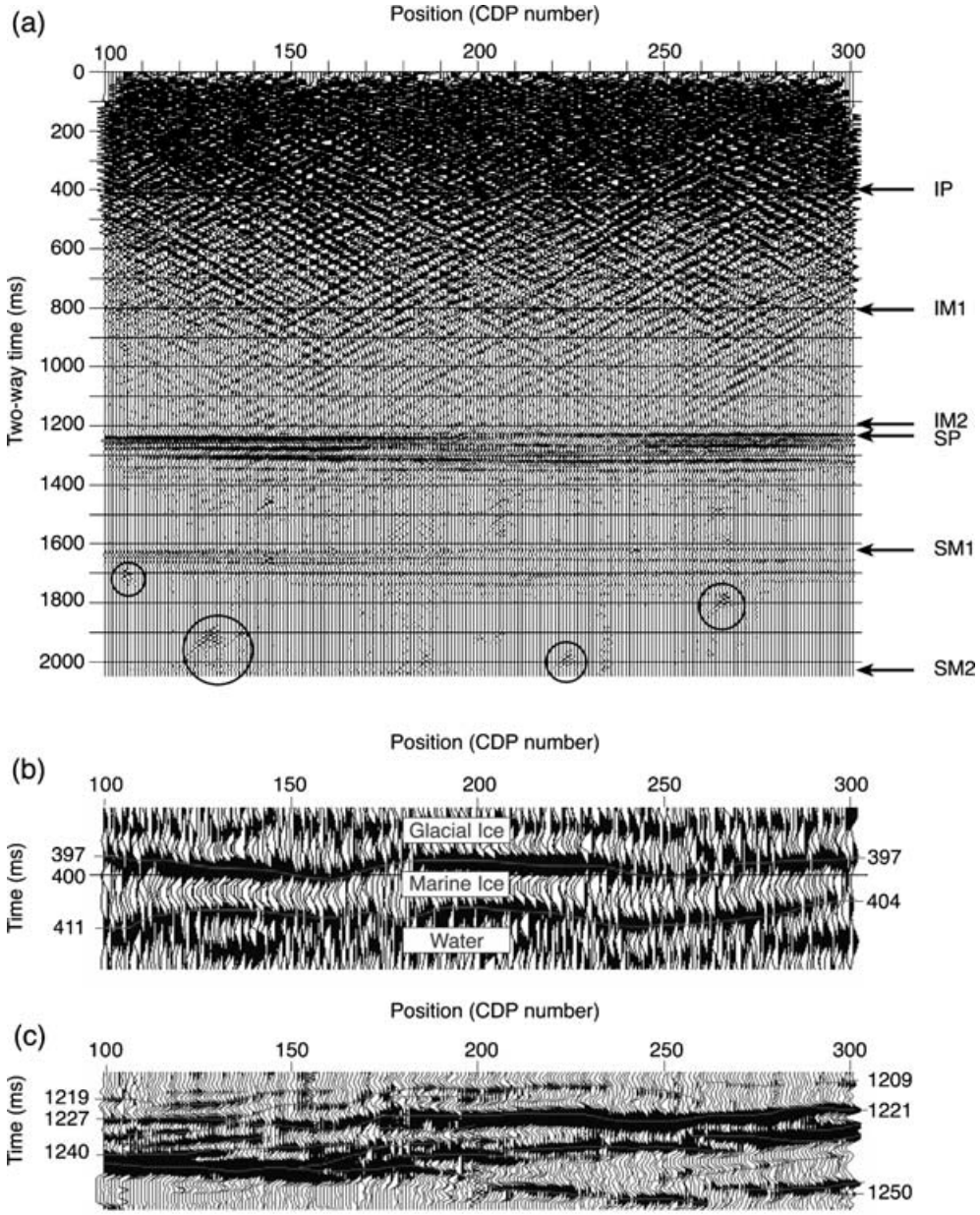

Figure 4. (a) CDP stacked section of processed reflection data showing all major reflections. Legend: IP—primary ice reflection; IM1—first-order ice multiple; IM2—second-order ice multiple; SP—primary sediment reflection; SM1—first-order sediment multiple; SM2—second-order sediment multiple. Circled objects are the deep hyperbolic reflections. (b) Detailed image of ice boundaries, with interpretation. (c) Detailed image of sedimentary layering, with interpretation.

The thickness of the water column can be calculated using a seismic velocity between 1400 and 1500 m s^{-1}. Cochrane & Cooper (1991) used a seismic velocity of 1460 m s^{-1} for the Prydz Bay water column, based on temperature and salinity measurements made at the Prydz Bay drill sites, whereas Beaudoin *et al.* (1992) used a velocity of 1440 m s^{-1} on the RIS. Cochrane & Cooper's (1991) value is the closer in proximity to the AIS, however, the environmental setting must be taken into account. The 1460 m s^{-1} value for Prydz Bay is based on the specific temperature and salinity measurements taken in Prydz Bay ocean waters. Under the AIS, there would be mixing of fresh water with the saline sea water from the melting of the shelf itself. Therefore, it would have a lower salinity, and a different seismic velocity. Beaudoin *et al.*'s (1992) value, 1440 m s^{-1}, has been proposed for the water under the RIS, and taking this as indicative of Antarctic waters under ice shelves, this velocity was used to calculate the water column thickness of the AIS. The water column thickness ranges from 597 m at the south end of the line to 594 m in the north, the average thickness being 595 m. This places the seafloor at a depth below the surface ranging from 1378 to 1362 m, from south to north.

Glacial material under the RIS has a seismic velocity of 2700 m s^{-1} (Beaudoin *et al.* 1992; Parasnis 1997; Sharma 1997), and sediment thickness under the ice shelf was calculated using this value (Beaudoin *et al.* 1992). Sonobuoy seismic studies in Prydz Bay taken on ODP Leg 119 show near surface seismic velocities exceed 2000 m s^{-1} at all sites studied (Cochrane & Cooper 1991). The data collected at Sonobuoy 5 (at Site 740; see Fig. 1), the closest to the AIS, show a range of seismic velocities for the glacial sediments

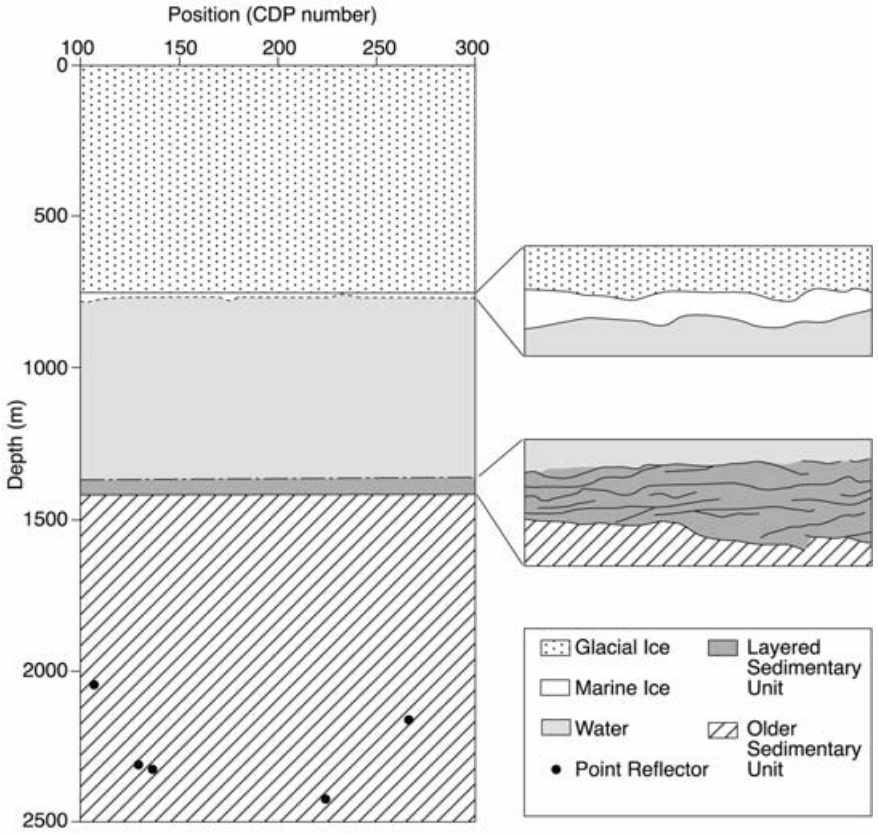

Figure 5. A converted depth model of the reflection data, showing enlargements of the glacial/marine–ice boundary and sedimentary layering.

between ∼2300 and 2850 m s^{-1}. This supports the use of 2700 m s^{-1} as a seismic velocity for the glacial sediments under the AIS. The AIS being in a similar environment with glacial sediments, a velocity of 2700 m s^{-1} has been used to calculate the thickness of this sedimentary column, which gives the stratified sedimentary sequence a thickness of 51–58 m. Using the full range of velocities (2300–2850 m s^{-1}) and a picking error of less than 0.5 ms to gain an idea of the error in this value, the thickness maybe be a maximum of 10 m thinner, or 5 m thicker. The point reflectors have also had depths calculated using 2700 m s^{-1} as the velocity, since there is no indication that the overlying materials have changed from a glacial type. These occur at depths ranging from approximately 2020 to 2400 m, with the average depth being approximately 2225 m.

The thicknesses of the ice and ocean cavity as modelled by Hunter *et al.* (2004) agree with the results we have obtained at G2A, and with previous depths measured from actual core data taken at site AM01 (near G1) (Fig. 1). In a bathymetry image of the AIS produced by Hunter *et al.* (2004) (produced in part from the sparse 1970s SAE seismic data), the depth to the seafloor in the image around our survey area is anywhere from 1100 to 1800 m in depth. The depth we found at G2A is well within this range. The thickness of ice under our survey location according to the profile produced by Hunter *et al.* (2004), extracted from the above-mentioned bathymetry image, is about 700 m, with no delineation given between meteoric and marine ice. The seafloor boundary in the profile is at about 1375 m below the surface. The depths gained from our survey relate well to these values, and can be used to support the models produced by Hunter *et al.* (2004).

From the AIS marine ice thickness models produced by Fricker *et al.* (2001), the marine ice thickness at our survey location is ∼20–30 m. This model is in good agreement with what is seen in the seismic data, where the marine ice thickness varies from 13–27 m. Fricker *et al.* (2001) model can also be compared to studies at G1, including a 315 m drill core taken in 1969 (Budd *et al.* 1982). This core revealed a three-layer structure in the AIS, with the marine ice being 45 m thick starting at a depth of 270 m (Allison 2003). Morgan (1972) used oxygen isotope evidence to show that the marine ice does indeed start at 270 m depth. He also states that the thickness of the shelf at G1 is 428 m thick, as determined by ice radar, and this results in a marine ice thickness of 158 m. Fricker *et al.* (2001) have given the thickness of marine ice here to be 141 m ± 30 m, which is consistent with Morgan's (1972) value. Fricker *et al.*'s (2001) model can then be considered as a robust image of the marine ice beneath the AIS.

The sediments under our survey line, as defined by seismic reflections, can be interpreted in terms of bedding (Fig. 4c). Individual beds are of approximately 3 ms thickness in TWT. The sedimentary layering shows evidence of sedimentary processes. The two major amplitude boundaries seen in the reflections decrease in amplitude to either end of the record—the upper reflection loses amplitude to the south, whereas the major reflection below that decreases in amplitude to the north, which may indicate a possible sedimentary foreset. The sediment reflections also reveal structures such as truncated beds (Fig. 4c, Fig. 5). Structures such as this have been described in sediments under other ice shelves and in glacial environments (Eyles & Eyles 1992; Lachniet *et al.* 1999; Raunholm *et al.* 2002).

It may be that the ∼55 m of stratified sediments seen in our seismic data are unconsolidated, and below these are more massive (hence non-reflection producing) and/or more compacted sedimentary units

that could be as old as the Oligocene or Eocene (Cochrane & Cooper 1991; Ehrmann 1991). In Prydz Bay, sedimentary units have been identified, including diatomaceous clay, diamictites, sands and carbonaceous shales, Lower Cretaceous sandstones and silts, and red bed sandstones and siltstones (Cochrane & Cooper 1991; Cooper *et al.* 1991; Stagg 1985). The bedrock under these sedimentary units, in Prydz Bay and under the AIS, is most likely Meso- to Early Neoproterozoic (Precambrian) high-grade metamorphic rocks (Cooper *et al.* 1991; Mikhalsky *et al.* 2001), based on mapping of the nearby PCMs.

The sediments taken from AM02 (Fig. 1) show lodgement till at the base of the core sample (Hemer & Harris 2003). Lodgement till is deposited closest to the grounding zone of the glacier, and is commonly compact with oriented clasts (Bennett & Glasser 1997; Drewry 1986; Sugden & John 1976). Till generally contains a large amount of erratic material, and so the point reflectors may be large boulders.

The point reflectors are seen quite distinctly in the raw data, and do not appear to be a relict of processing, but a true feature. Upon analysis of every raw record, the hyperbolic reflections do appear in numerous records at approximately the correct position as where they would appear in the CDP gather. They do not appear in every record, but consistently enough for the existence of something at depth producing these hyperbolae to be a definite possibility. They are not simply caused by shot-generated noise, since they do not show the same characteristic as this type of event, which is a persistent high-amplitude anomaly throughout the record for two to three traces around the shot location. Also, the hyperbolae are found in the record unrelated to shot location.

When comparing the times and positions of the significant hyperbolae seen in the stacked record to times and positions of hyperbolae in the individual records, there is a remarkable correlation. Times in the records closely, and sometimes almost exactly, match arrivals in the stacked section.

From the hyperbola reflection shapes in the stacked section, whatever is responsible would appear to be inclined to the south, except for the one at CDP 107, which seems to be more vertical than the others. However, in the raw records, the hyperbolae appear to be more symmetric. The inclination could be due to the stacking process.

The hyperbolae could represent the presence of boulders, which would fit a glacial environment of deposition, possibly from a time when the grounding zone of the AIS was further north, dropping large boulders within the till. Hyperbolic point reflections could indicate vertical fractures (broken bedrock) or a blocky, bouldery texture—the result of basal ice structures from the glaciation that deposited the sediments (Sweat 1997). In the case of our data, it is possible that the point reflectors indicate a broken or jagged bedrock surface. Assuming the AIS was grounded somewhere nearby in its past, the action of the ice working on the bedrock could have deformed the substrate, as happens in glacial environments (Eyles & Eyles 1992), producing this kind of surface. The absence of any linear reflection between the individual hyperbolae in the data, however, means it cannot be confidently stated that the hyperbolae indicate a bedrock surface.

Other surveys performed in the region of the AIS suggest that the bedrock could appear in the data record (Federov *et al.* 1982). According to a cross-section through the AIS based on geophysical data, especially deep seismic sounding (Federov *et al.* 1982), the bedrock begins at a depth of $\sim$1 km. Mishra *et al.* (1999), who studied the gravity and magnetic anomalies of the Lambert Graben, also mention that the bottom of the subglacial valley is greater than 1 km below sea level. Fricker *et al.* (2001) states the AIS sits in a long, narrow cavity with a maximum draft of 2200 m. This depth is also approximately coincident with the depth where the point reflectors appear. If the glaciers were once grounded further north than where they are at present, features could be evident at this same depth, again meaning the hyperbolae are possibly related to features produced by basal glacier processes.

The Ocean Drilling Program (ODP) Leg 188, discussed by Passchier *et al.* (2003), took drill cores in Prydz Bay. The closest drill site to the shelf is Site 1166, located approximately 400 km from the front of the ice shelf on the continental shelf, where drilling penetrated 343 m of Holocene through to Cretaceous sediments. A seismic interpretation of the extent and depth of the sediments shows that they are around 670 m deep. If the depth of hyperbolic point reflections under G2A indicate a bedrock surface, and the material above that, is therefore, sediment deposits, to an approximate thickness of 835 m, this would indicate a much larger thickness of sediments in the ice shelf cavity than in the open sea.

A 225.5 m sediment core was retrieved from Site 740, showing sandstones and siltstones overlain by diatom ooze (Hambrey *et al.* 1991). The seismic line ODP-119, part of ODP Leg 119, was surveyed over Sites 739, 742, 741, and 740 (Fig. 1). It shows basement rock, most likely eroded Precambrian metamorphic rock, occurs to depths of up to 2 km, and probably deeper (Cooper *et al.* 1991; Federov *et al.* 1982). Magnetic profiles that have been taken across Prydz Bay show there is a minimum basement depth of 2.5–3 km (Cooper *et al.* 1991). This shows a similar depth as our data, so again this suggests the possibility that bedrock is seen under the glacial units in our data.

Another possible cause for the deep hyperbolic reflections is the presence of dykes within the basement. An eroded surface in which dykes display higher relief than surrounding weathered softer material could form a terrain that would produce the results we have seen. In effect, the dykes would be a relatively narrow ridge, acting like a point for the seismic waves to reflect off, producing a hyperbola in the seismic record. The difference in physical properties alone of the dykes compared to their host rock may also be sufficient to produce the hyperbolic reflections.

The most likely rocks to be found under G2A are those belonging to the Beaver-Lambert Terrane, as described by Mikhalsky *et al.* (2001). Within the Beaver-Lambert Terrane are found mafic granulite, ultramafic and metadolerite dykes, mostly 2–15 m wide, with some material gathering in small plutons up to 50 m across (Mikhalsky *et al.* 2001). These types of dykes may be what our detailed reflection survey has imaged.

CONCLUSION

The seismic survey employed on the AIS to produce a detailed image of the subsurface structure has been successful. Using a geophone spacing of 10 m, with 20 m spaced interior shots to maintain a six fold coverage, a seismic data set has been produced that has revealed detailed information about the AIS subsurface. In particular it has imaged the marine ice layer, which up to now, beside time-consuming drill core sampling, had only been imaged using numerical modelling, such as Fricker *et al.*'s (2001) method utilizing RESs and DEMs. It is extremely important to note the seismic technique's ability to directly view the marine ice itself.

The detailed reflection data collected in this survey on the AIS has revealed a detailed view of the subsurface structure, clearly delineating the meteoric and marine ice boundaries, defining a water column thickness, and sedimentary structure with the upper 55 m

of sediments. The marine ice layer ranges in thickness from 13 to 27 m, and the 55 m of stratified sediments show structures such as truncated beds and foresets. The part of the record below this unit that displays no reflections is likely formed of massive sandstones or siltstones (Hambrey *et al.* 1991), and compared to sediments off the front of the shelf, they could possibly be as old as Oligocene in age (Ehrmann 1991). Point reflectors seen at ∼2200 m depth are in most likelihood features of a broken bedrock surface (the result of glacial action), large boulders or the presence of dykes. This bedrock surface refers to older Proterozoic rocks, whereas above this would be the Permian–Tertiary sediments (Hambrey 1991). The depth to this surface found from our data correlates with estimated depths made by Federov *et al.* (1982) and Fricker *et al.* (2001), and bedrock depths gained from reflection data off the front of the ice shelf (Cooper *et al.* 1991).

Detailed seismic studies make a valuable accompaniment to current GPS and drill core studies on the AIS. It overcomes the problems encountered with ice radar where the marine ice cannot be seen, and improves upon the SAE seismic data where the marine ice was also not mapped. So overall, the method for seismic studies on the AIS as used for this study is a useful method for mapping the subsurface structure of the AIS in a quick, easy to repeat manner, and would be beneficial in a continuation of studies on the AIS.

The bathymetry, and hence the water column thickness, under the AIS is poorly known up to this date (Hunter *et al.* 2004), and performing more surveys such as this seismic survey would greatly improve the quantity and quality of data gathered on the AIS, providing clarification on the current structural model of the AIS. A better model means improvements can be made to mass balance calculations, and any change of the mass balance can be better recorded and analysed. This is turn will improve studies of global climate change, and how this affects the volume of ice in Antarctica and fluctuations in global sea level.

ACKNOWLEDGMENTS

Thanks go to Richard Coleman (University of Tasmania), Jeremy Bassis (SCRIPPS Institute), Alan Elcheikh (AAD), Michael Woolridge (AAD) and Chris Legge (AAD), for their assistance in the collection of data. Also to Phil O'Brien, Tim Barton, and Alan Crawford of Geoscience Australia for generously supplying seismic equipment for the survey, and to ANARE for their logistical support. Phil O'Brien and an anonymous reviewer are thanked for their constructive reviews, which have resulted in an improved manuscript. This research was funded by ASAC Project 2542. This is contribution 430 from the ARC National Key Centre for Geochemical Evolution and Metallogeny of Continents (GEMOC).

REFERENCES

Allison, I., 2003. The AMISOR project: ice shelf dynamics and ice-ocean interaction of the Amery Ice Shelf. Forum for Research into Ice Shelf Processes, Report (14). Web address: http://www.gfi.uib.no/frisp/Rep14/allison.pdf (accessed 15/06/05)

Beaudoin, B.C., ten Brink, U.S. & Stern, T.A., 1992. Characteristics and processing of seismic data collected on thick, floating ice: results from the Ross Ice Shelf, Antarctica, *Geophysics*, **57**(10), 1359–1372.

Bennett, M.R. & Glasser, N.F., 1997. *Glacial geology, ice sheets and landforms*, p. 364, John Wiley & Sons, New York, NY.

Blindow, N., 1994. The central part of the Filchner-Ronne Ice Shelf, Antarctica: internal structures revealed by 40 Hz monopulse RES, *Ann. Glaciol.*, **20,** 365–371.

Budd, W., Corry, M.J. & Jacka, T.H., 1982. Results from the Amery Ice Shelf Project, *Ann. of Glaciol.*, **3,** 36–41.

Cochrane, G.R. & Cooper, A., 1991. Sonobuoy seismic studies at ODP drill sites in Prydz Bay, Antarctica, in *Proceedings of the Ocean Drilling Program, Scientific Results*, Vol. 119, pp. 27–43, eds Barron, J., Enderson, J., Baldauf, J. & Larsen, B.

Cooper, A., Stagg, H. & Geist, E., 1991. Seismic stratigraphy of Prydz Bay, Antarctica: implications from Leg 119 drilling, in *Proceedings of the Ocean Drilling Program, Scientific Results*, Vol. 119, pp. 5–25, eds Barron, J., Enderson, J., Baldauf, J. & Larsen, B.

Craven, M., Elcheikh, A., Brand, R. & Allison, I., 2003. Hot water drilling on the Amery Ice Shelf, East Antarctica. Forum for Research into Ice Shelf Processes, Report (14). Web address: http://www.gfi.uib.no/frisp/Rep14/craven.pdf (accessed 15/06/05)

Drewry, D.J. (Ed.), 1983. *Antarctica: Glaciological and Geophysical Folio*, Scott Polar Research Institute, Cambridge.

Drewry, D.J., 1986. *Glacial Geologic Processes*, 1st edn, pp. 132–133, Edward Arnold Ltd., London.

Ehrmann, W.U., 1991. Implications of sediment composition on the southern Kerguelen Plateau for paleoclimate and depositional environment, in *Proceedings of the Ocean Drilling Program, Scientific Results*, Vol. 119, pp. 185–210, eds Barron, J., Enderson, J., Baldauf, J. & Larsen, B.

Eyles, N. & Eyles, C., 1992. Glacial depositional systems, in *Facies Models: Response to Sea Level Change*, pp. 73–100, eds Walker, R.G. & James, N.P., Geological Association of Canada.

Federov, L.V., Grikurov, G.E., Kurinin, R.G. & Masolov, V.N., 1982. Crustal structure of the Lambert Glacier from geophysical data, in *Antarctic Geoscience*, pp. 931–936, eds Craddock, C., Loveless, J.K., Vierima, T.L. & Crawford, K., University of Wisconsin Press, Madison, Wisconsin.

Fricker, H.A., Popov, S., Allison, I. & Young, N., 2001. Distribution of marine ice beneath the Amery Ice Shelf, *Geophys. Res. Lett.*, **28**(11), 2241–2244.

Fricker, H.A. *et al.*, 2002. Redefinition of the Amery Ice Shelf, East Antarctica, grounding zone, *J. geophys. Res.*, **107**(B5), ECV 1/1–1/9.

Hambrey, M.J., 1991. Structure and dynamics of the Lambert Glacier-Amery Ice Shelf system: implications for the origin of Prydz Bay sediments, in *Proceedings of the Ocean Drilling Program, Scientific Results*, Vol. 119, pp. 61–74, eds Barron, J., Enderson, J., Baldauf, J. & Larsen, B.

Hambrey, M.J., Ehrmann, W.U. & Larson, B., 1991. Cenozoic glacial record of the Prydz Bay Continental Shelf, East Antarctica, in *Proceedings of the Ocean Drilling Program, Scientific Results*, Vol. 119, pp. 77–132, eds Barron, J., Enderson, J., Baldauf, J. & Larsen, B.

Hemer, M. & Harris, P.T., 2003. Sediment core from beneath the Amery Ice Shelf, East Antarctica, suggests mid-Holocene ice-shelf retreat, *Geology*, **31**(2), 127–130.

Hunter, J., Hemer, M. & Craven, M., 2004. Modeling the circulation under the Amery Ice Shelf. Forum for Research into Ice Shelf Processes, Report (15). Web address: http://www.gfi.uib.no/frisp/Rep15/hunter.pdf (accessed 15/06/05)

Lachniet, M.S., Larson, G.J., Strasser, J.C., Lawson, D.E., Evenson, E.B. & Alley, R.B., 1999. Microstructures of glacigenic sediment-flow deposits, Matanuska Glacier, Alaska, in *Glacial processes: past and present*, pp. 45–57, eds Mickelson, D.M. & Attig, J.W., Boulder, Colorado, Geological Society of America Special Paper 337.

Lønne, I., 1995. Sedimentary facies and depositional architecture of ice-contact glaciomarine systems, *Sediment. Geol.*, **98,** 13–43.

Mikhalsky, E.V., Sheraton, J.W., Laiba, A.A., Tingey, R.J., Thost, D.E., Kamenev, E.N. & Federov, L.V., 2001. Geology of the Prince Charles Mountains, Antarctica. AGSO—Geoscience Australia, Canberra; bulletin 247.

Mishra, D.C., Chandra Sekhar, D.V., Venkata Raju, D. Ch. & Vijaya Kumar, V., 1999. Crustal structure based on gravity-magnetic modelling constrained from seismic studies under Lambert Rift, Antarctica and Godavari and Mahanadi rifts, India and their relationship, *Earth planet. Sci. Lett.*, **172**(3–4), 287–300.

Morgan, V.I., 1972. Oxygen isotope evidence for bottom freezing on the Amery Ice Shelf, *Nature*, **238**(5364), 393–394.

Parasnis, D.S., 1997. *Principles of applied geophysics*, 5th edn, Chapman & Hall, London.

Passchier, S., O'Brien, P.E., Damuth, J.E., Januszczak, N., Handwerger, D.A. & Whitehead, J.M., 2003. Pliocene-Pleistocene glaciomarine sedimentation in eastern Prydz Bay and development of the Prydz Bay trough-mouth fan, ODP Sites 1166 and 1167, East Antarctica, *Mar. Geol.*, **199,** 279–305.

Raunholm, S., Larsen, E. & Sejrup, H.P., 2002. Weichselian sediments at Foss-Eikeland, Jæren (southwest Norway): sea level changes and glaciation history, *J. Quat. Sci.*, **17**(3), 241–260.

Ravich, M.G., 1974. Section through the Permian coal measures in the Beaver Lake area (Prince Charles Mountains, East Antarctica), *Antarktica, Doklady Komissii*, **13,** 19–35.

Ravich, M.G. & Federov, L.V., 1977. Geologic structure of MacRobertson Land and Princess Elizabeth Land, East Antarctica, in *Antarctic Geoscience*, pp. 499–504, eds Craddock, C., Loveless, J.K., Vierima, T.L. & Crawford, K., University of Wisconsin Press, Madison, Wisconsin.

Robin, G. deQ., 1958. Seimic shooting and related investigations: Norwegian-British-Swedish Antarctic Expedition, 1949–1952, Scientific Results. V5, Norsk Polarinstitutt, Oslo.

Sharma, P.V., 1997. *Environmental and engineering geophysics*, Cambridge University Press, Cambridge.

Stagg, H.M.J., 1985. The structure and origin of Prydz Bay and MacRobertson Shelf, East Antarctica, *Tectonophysics*, **114,** 315–340.

Sugden, D.E. & John, J.S., 1976. *Glaciers and landscape*, p. 376, Edward Arnold Ltd., London.

Sweat, M.J., 1997. Continuous seismic-reflection profiling near Grassy Island, Wyandotte Unit of Shiawassee National Wildlife Refuge, Wyandotte, Michigan. USGS Administrative Completion Report for WRD Reimbursable Agreement No. 8-4426-06000 of USFWS Parent Project No. 14-48-0003-97-905, DCN#1448-30181-97-N344, Unofficial publication #ACR97-01, Lansing, Michigan. Web address: http://mi.water.usgs.gov/pubs/MISC/ACR97-01/ACR97-01LW.php (accessed 10/06/05)

Thiel, E. & Ostenso, N.A., 1961. Seismic studies on Antarctic ice shelves, *Geophysics*, **26**(6), 706–715.

Tingey, R.J., 1972. Geological work in Antarctica, 1971. *Record of Bureau of Mineral Resources, Geology & Geophysics, Australia.* 1972/132, 49 p.

Tingey, R.J., 1982. The geologic evolution of the Prince Charles Mountains—an Antarctic cratonic block, in *Antarctic Geoscience*, pp. 455–464, ed. Craddock, C., University of Wisconsin Press, Madison, Wisconsin

Zelt, C.A. & Smith, R.B., 1992. Seismic traveltime inversion for 2-D crustal velocity structure, *Geophys. J. Int.*, **108,** 16–34.

Appendix B

Source reference for online Javascript Sea Water Equation of State calculator used in Chapter 6 to convert AMISOR CTD data to seismic property values (including P wave velocity) to be used in reflection coefficient calculations.

Webpage title: A Sea Water Equation of State Calculator
Website URL: http://fermi.jhuapl.edu/denscalc.html
Date Accessed: July 2007
Author: Rick Chapman
Affiliation: The Johns Hopkins University Applied Physics Laboratory
Webpage last updated: 26th November 2006 17:17:54

Screen Shot of Calculator:

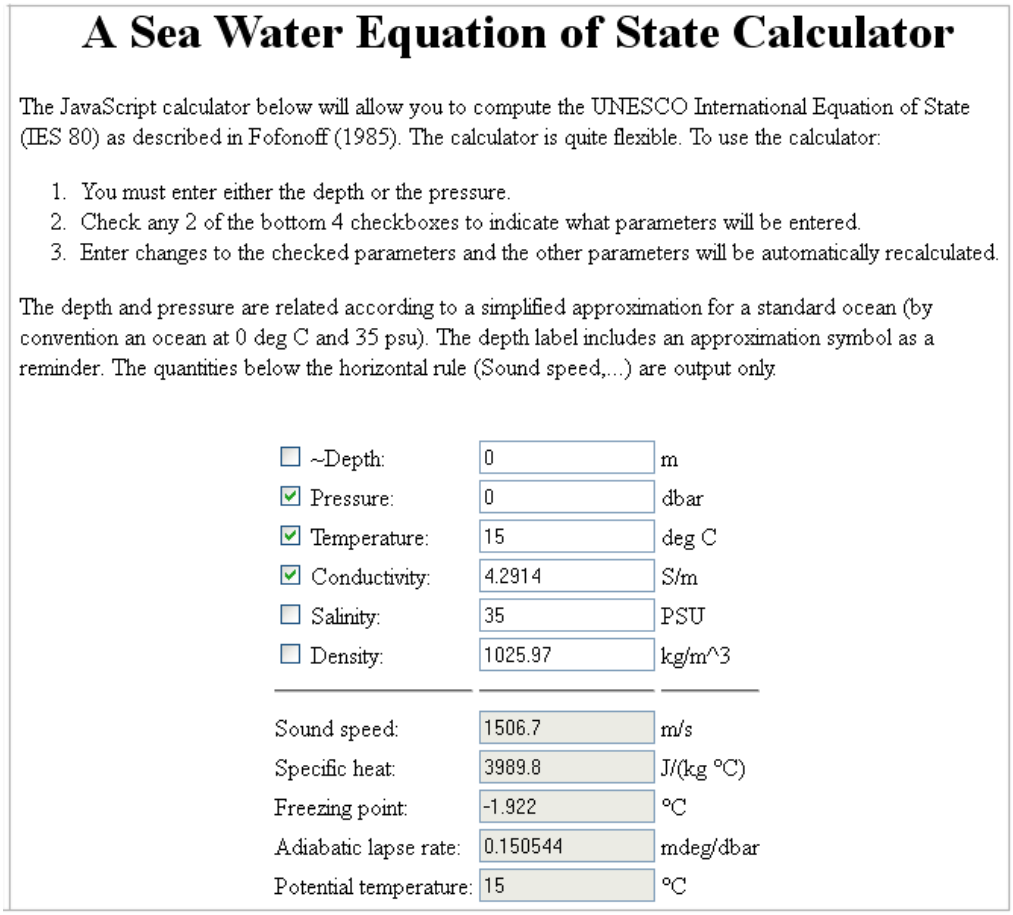

A Sea Water Equation of State Calculator

The JavaScript calculator below will allow you to compute the UNESCO International Equation of State (IES 80) as described in Fofonoff (1985). The calculator is quite flexible. To use the calculator:

1. You must enter either the depth or the pressure.
2. Check any 2 of the bottom 4 checkboxes to indicate what parameters will be entered.
3. Enter changes to the checked parameters and the other parameters will be automatically recalculated.

The depth and pressure are related according to a simplified approximation for a standard ocean (by convention an ocean at 0 deg C and 35 psu). The depth label includes an approximation symbol as a reminder. The quantities below the horizontal rule (Sound speed,...) are output only.

☐ ~Depth:	0	m
☑ Pressure:	0	dbar
☑ Temperature:	15	deg C
☑ Conductivity:	4.2914	S/m
☐ Salinity:	35	PSU
☐ Density:	1025.97	kg/m^3
Sound speed:	1506.7	m/s
Specific heat:	3989.8	J/(kg °C)
Freezing point:	-1.922	°C
Adiabatic lapse rate:	0.150544	mdeg/dbar
Potential temperature:	15	°C

Further webpage update information given by author: Text was updated on November 24, 2006 to include reference list and links to UNESCO papers. The calculator was updated on January 22, 2006. A description of how to access the Javascript code was added to address a frequently asked question. Additional comments were also added to the Javascript code to make it slightly easier to read. This calculator was updated on June 17, 1998 and again on November 8, 1999 to fix bugs in the interpretation of pressure units (dbar vs bar). The updated version has been checked against additional test points and seems to be accurate. The calculator now also updates automatically if the pressure or depth units are changed. The depth and pressure calculations were updated on Feb 23, 2000, based on the suggestion of Pascal Vernin.

Sources:

Calculator is based on the International Equation of State described by Fofonoff (1985).

Fofonoff, N. P., "Physical Properties of Seawater: A New Salinity Scale and Equation of State of Seawater," *Journal of Geophysical Research*, Vol 90 No. C2, pp 3332-3342, March 20, 1985.

The speed of sound calculation is based on Chen and Millero (1977).

Chen and Millero, "Speed of sound in seawater at high pressures," *Journal of the Acoustical Society of America*, Vol. 62, No. 5, 1129-1135, Nov 1977.

The values for the other four parameters are based on Fofonoff & Millard (1983).

Fofonoff and Millard, "Algorithms for computation of fundamental properties of seawater," *UNESCO Technical papers in marine science* No. 44, 1983.

Paper available through URL:

http://fermi.jhuapl.edu/denscalc/fofonoff_millard_1983.pdf

Date Accessed: 20/7/2007

Appendix C

SeisImager discrete layer models and Rayinv velocity gradient models

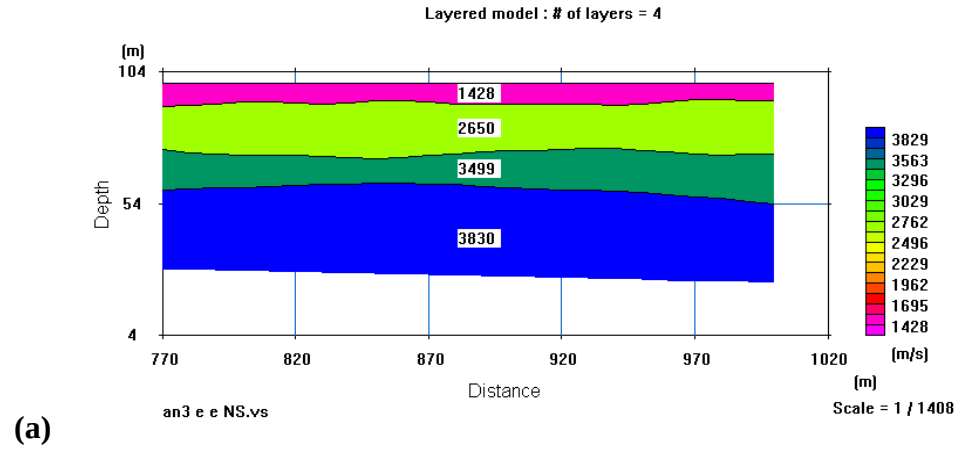

(a)

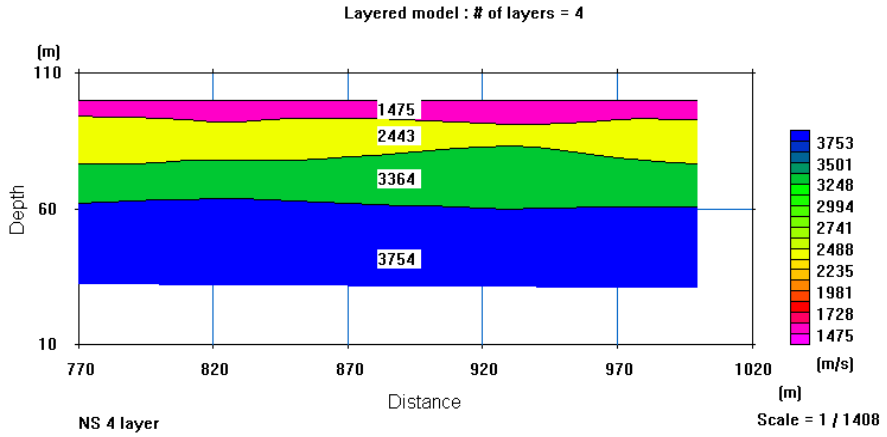

(b)

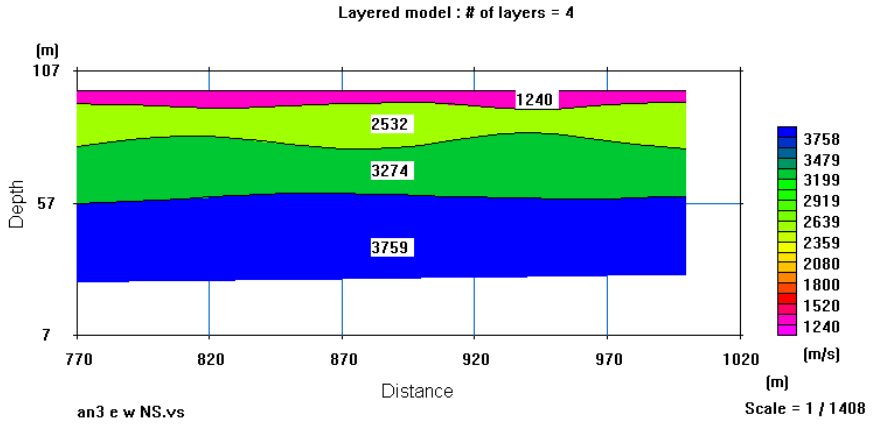

(c)

Figure C1- 2D Seismic refraction profiles for the LME-3 group; NS profile lines. At locations (a) LME-3E, (b) LME-3Ct, (c) LME-3W.

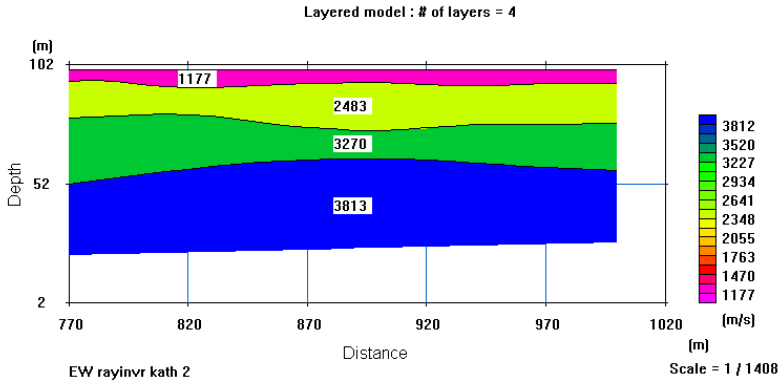

(a)

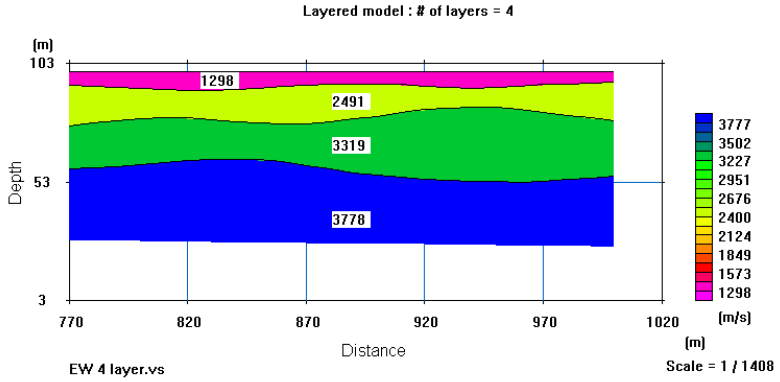

(b)

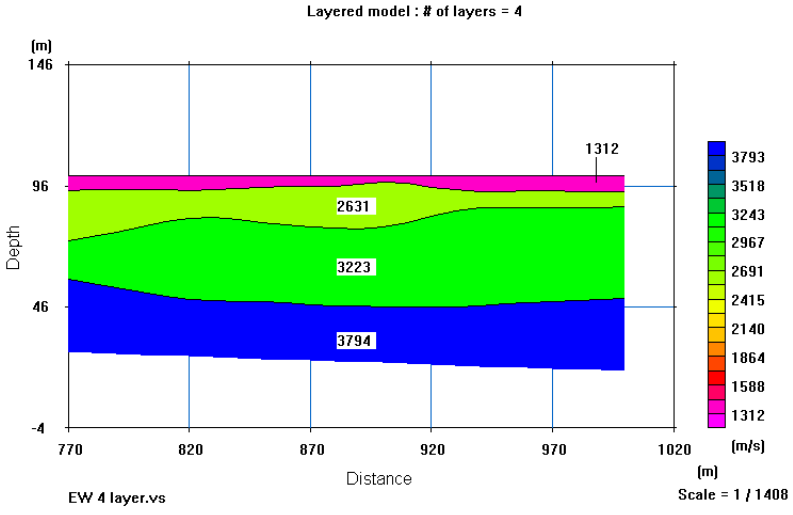

(c)

Figure C2 - 2D Seismic refraction profiles for the LME-3 group; EW profile lines. At locations (a) LME-3E, (b) LME-3C, (c) LME-3W.

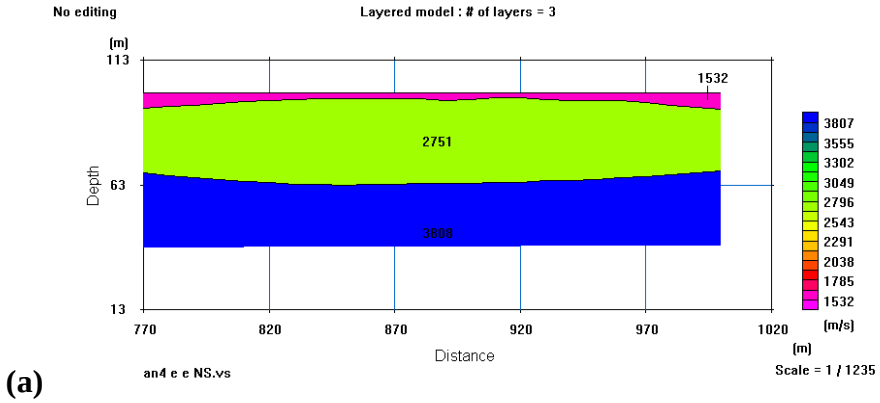

(a)

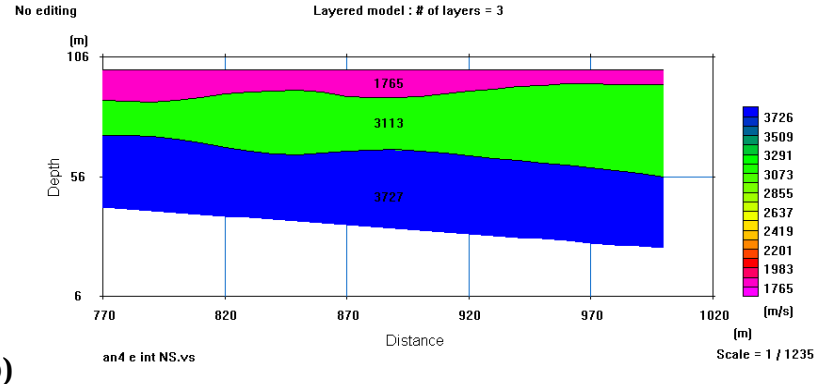

(b)

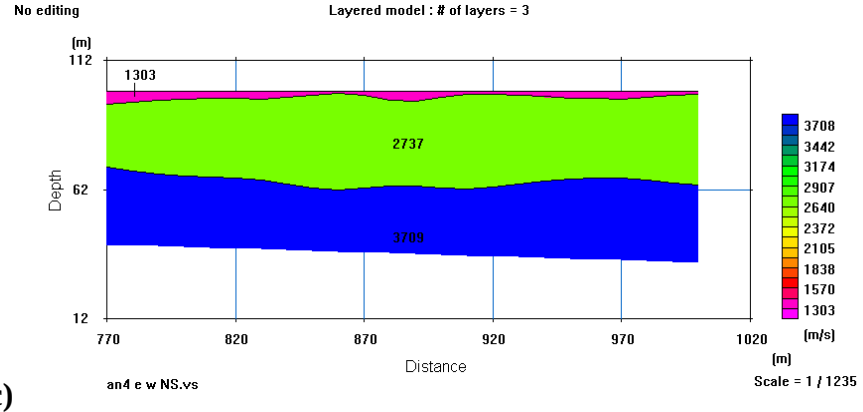

(c)

Figure C3 - 2D Seismic refraction profiles for the LME-1 group; NS profile line. At locations (a) LME-1E, (b) LME-1C, (c) LME-1W.

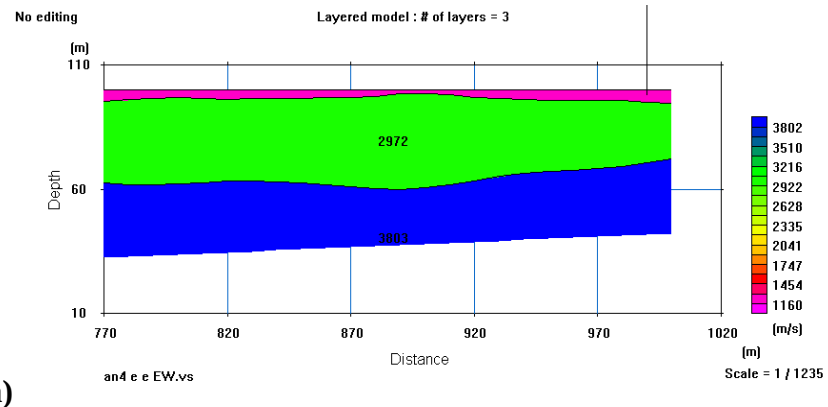

(a)

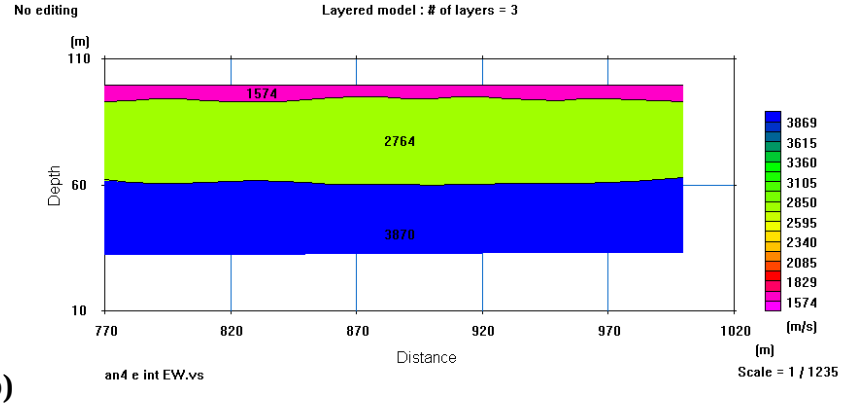

(b)

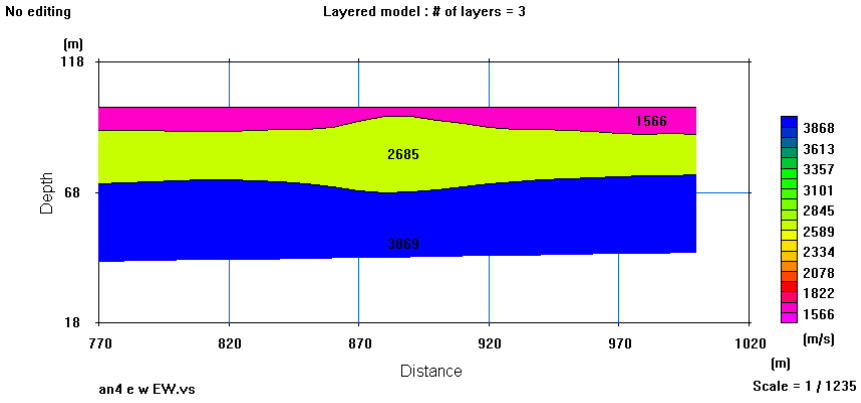

(c)

Figure C4 - 2D Seismic refraction profiles for the LME-1 group; EW profile lines. At locations (a) LME-1E, (b) LME-1C, (c) LME-1W

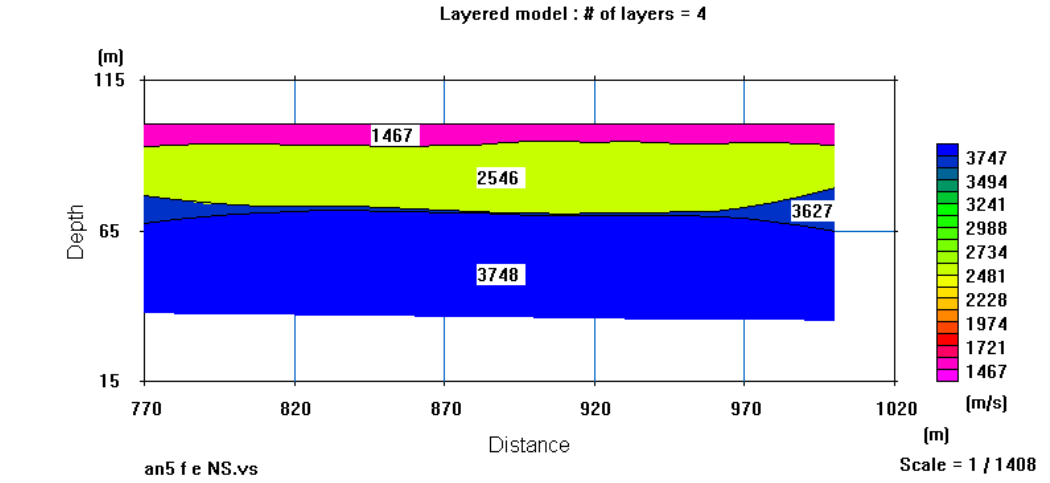

(a)

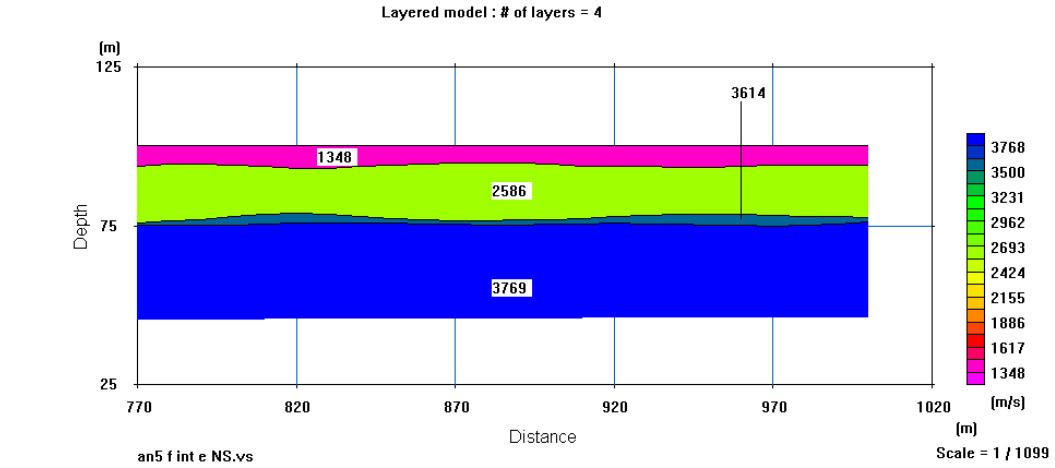

(b)

Figure C5 - 2D Seismic refraction profiles for the ML group; NS profile lines. At locations (a) ML-E, (b) ML-CE.

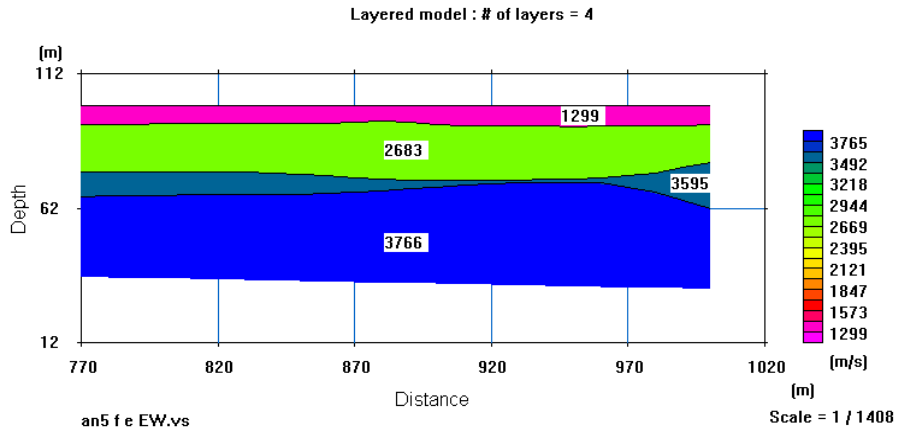

(a)

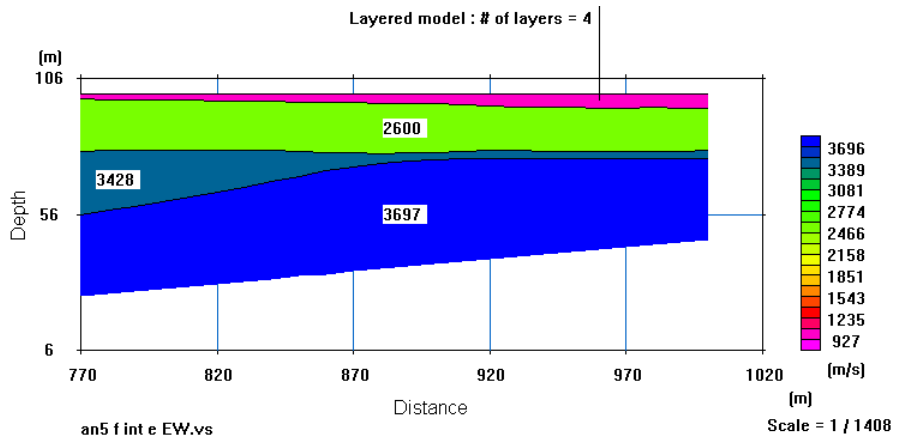

(b)

Figure C6 - 2D Seismic refraction profiles for the ML group; EW profile lines. At locations (a) ML-E, (b) ML-CE

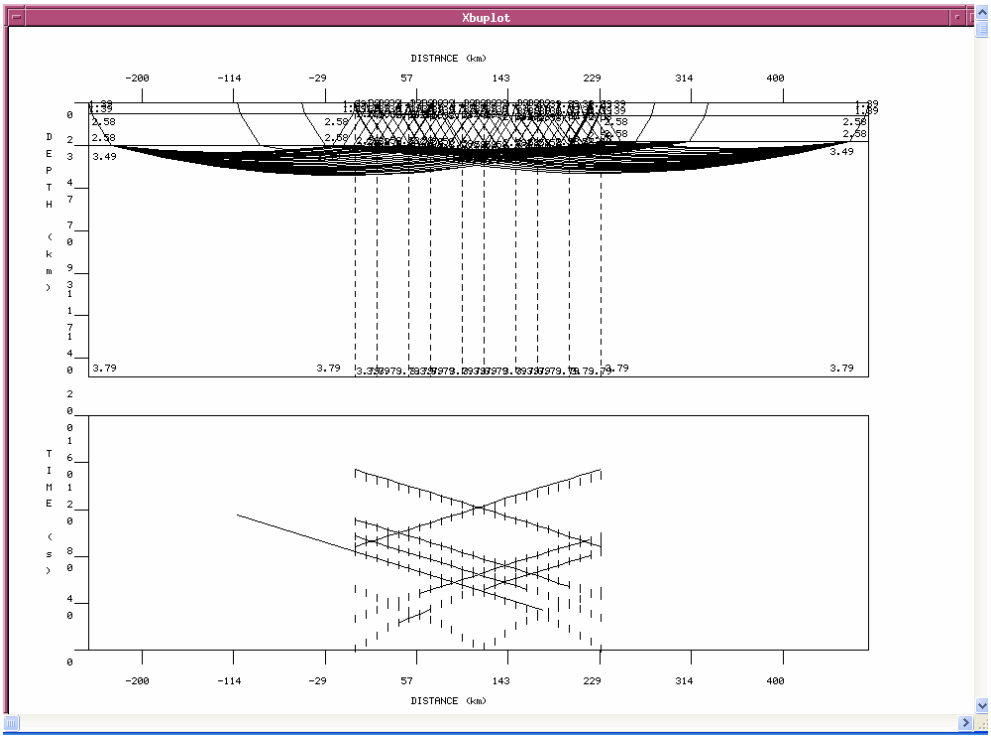

Figure C7 – Ray inverse tracing model for LME-2C NS line, with a three layer model. Depths are in km and velocities in km/s.

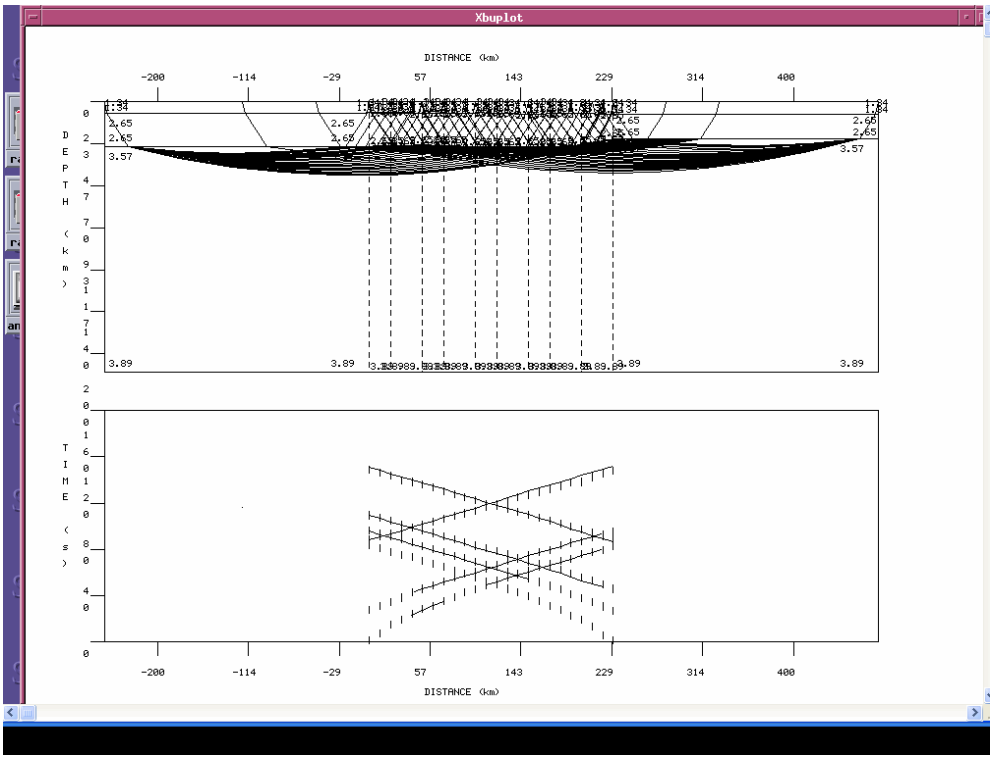

Figure C8 – Ray inverse tracing model for LME-2C EW line, with a three layer model. Depths are in km and velocities in km/s.

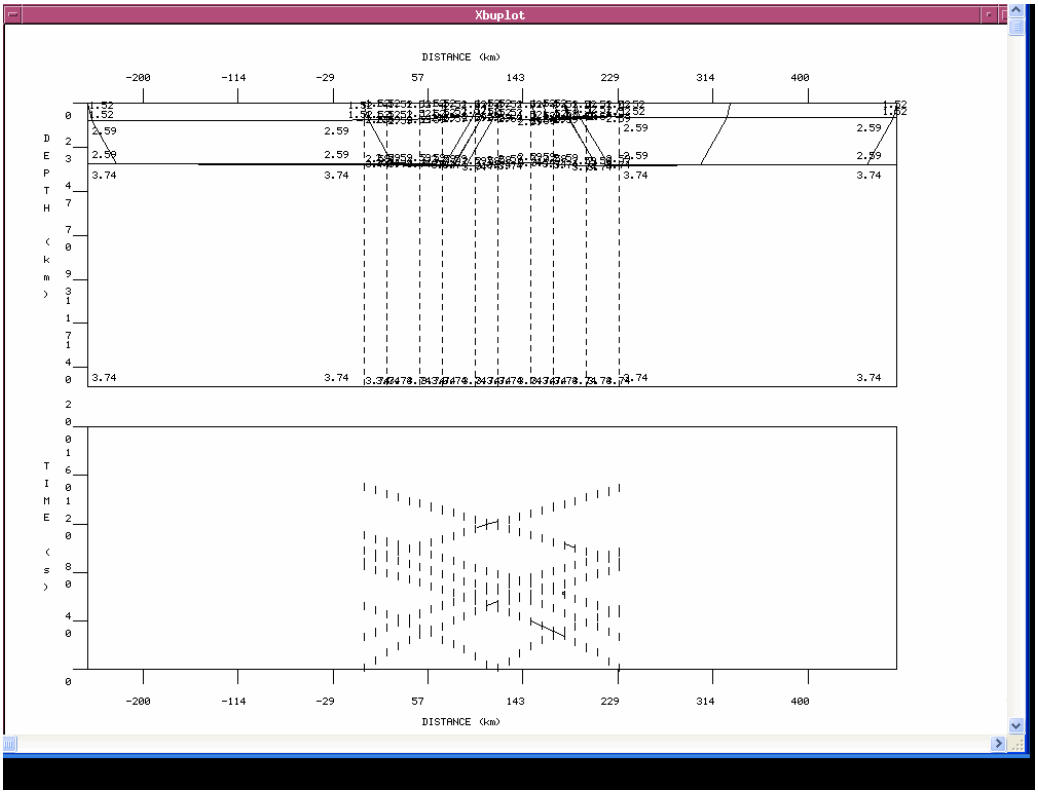

Figure C9 – Ray inverse tracing model for LME-2EE NS line, with a three layer model. Depths are in km and velocities in km/s.

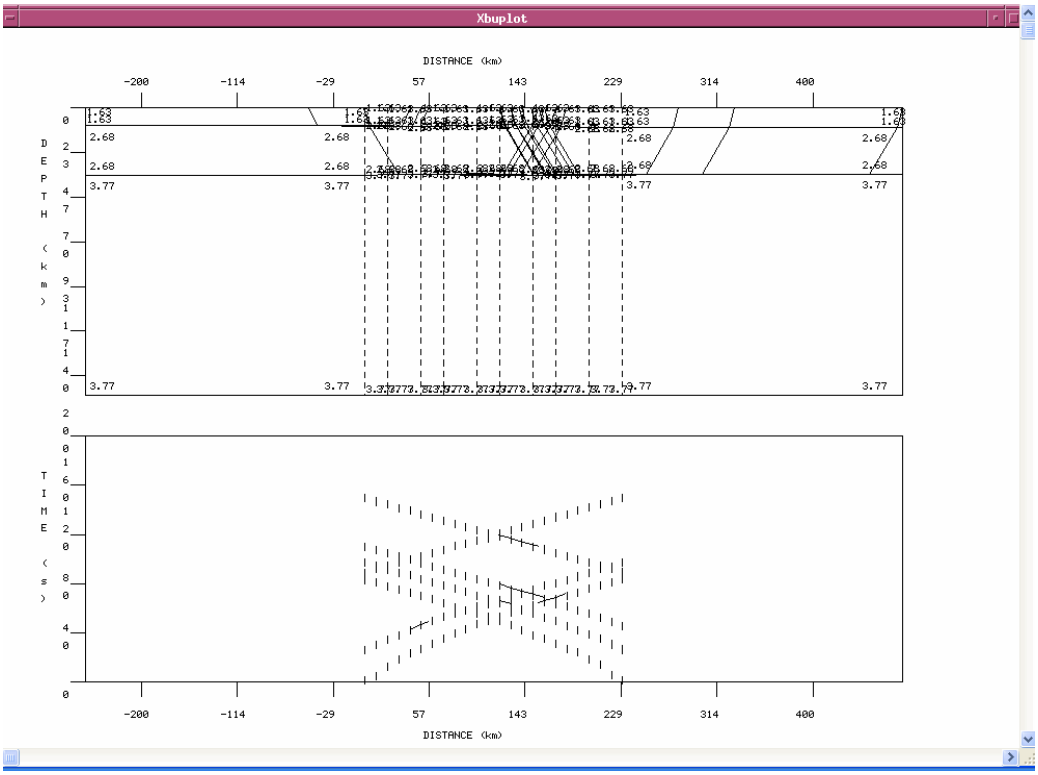

Figure C10 – Ray inverse tracing model for LME-2EE EW line, with a three layer model. Depths are in km and velocities in km/s.

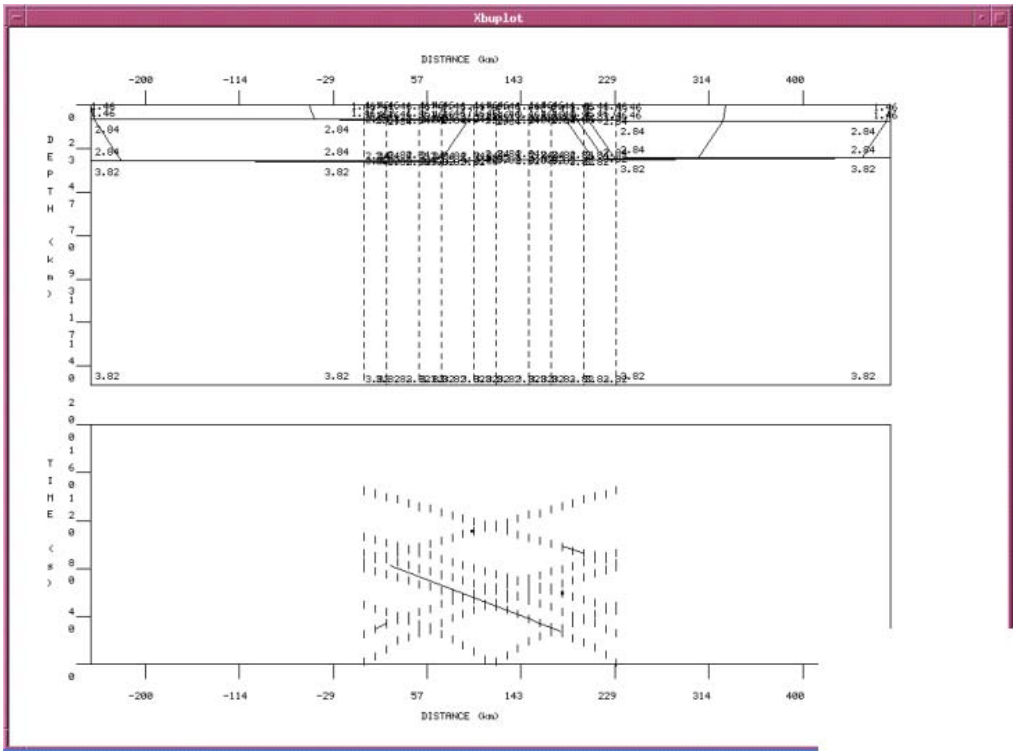

Figure C11 – Ray inverse tracing model for LME-1W NS line, with a three layer model. Depths are in km and velocities in km/s.

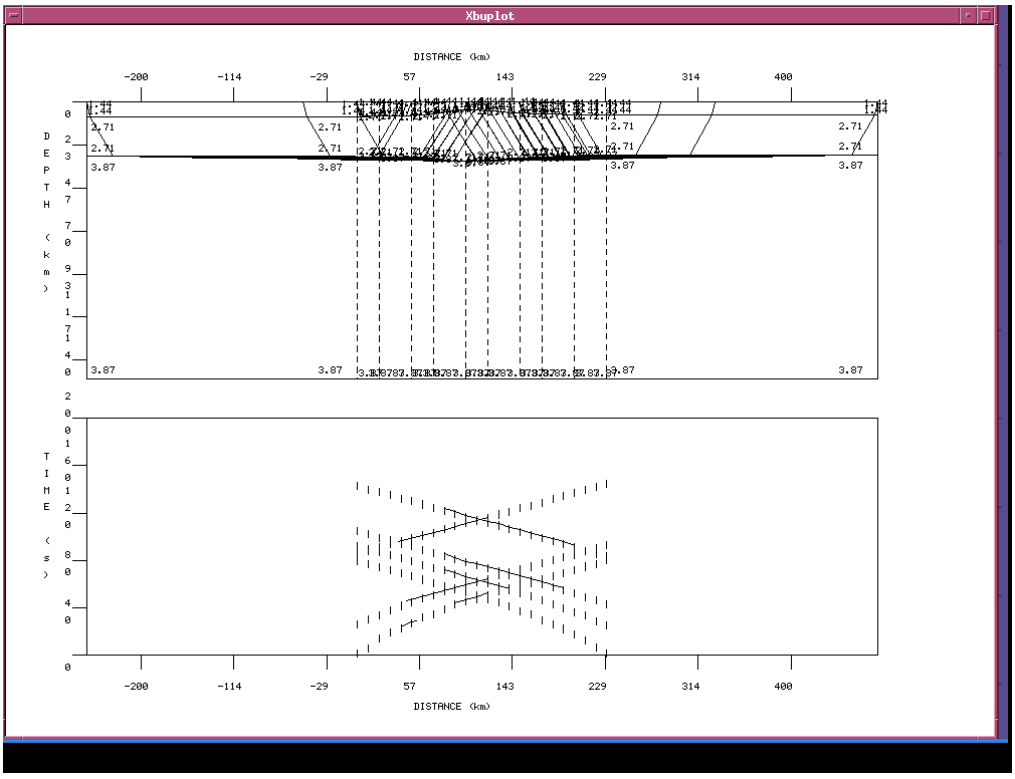

Figure C12 – Ray inverse tracing model for LME-1W EW line, with a three layer model. Depths are in km and velocities in km/s.

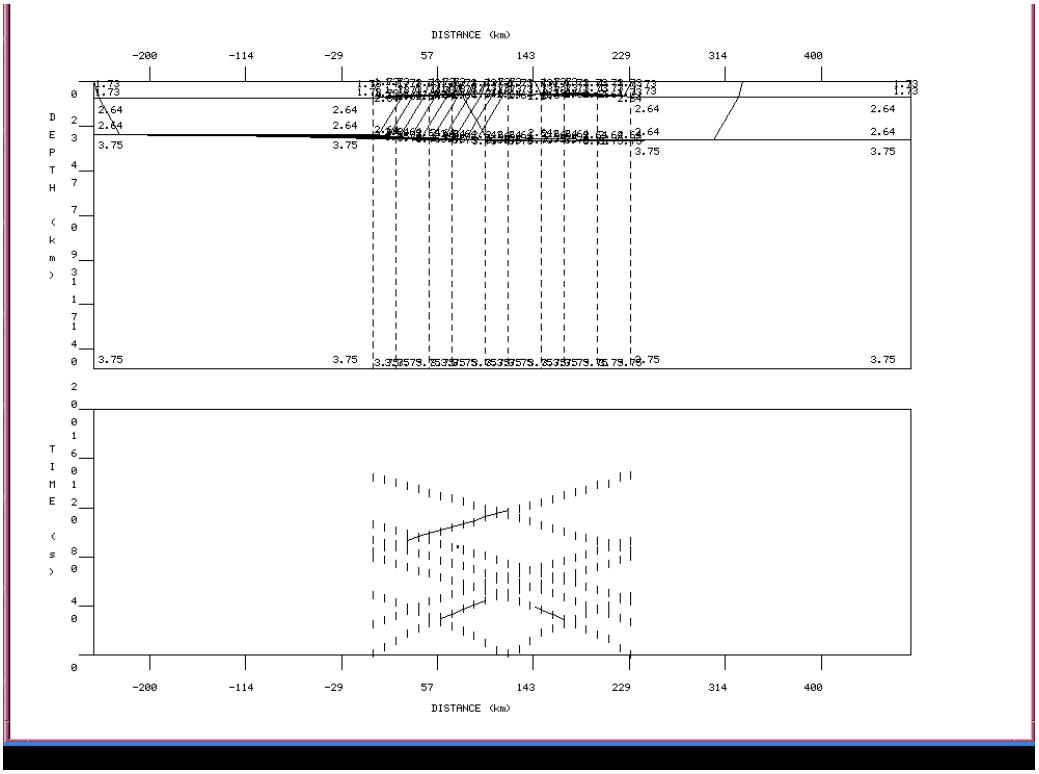

Figure C13 – Ray inverse tracing model for LME-1C NS line, with a three layer model. Depths are in km and velocities in km/s.

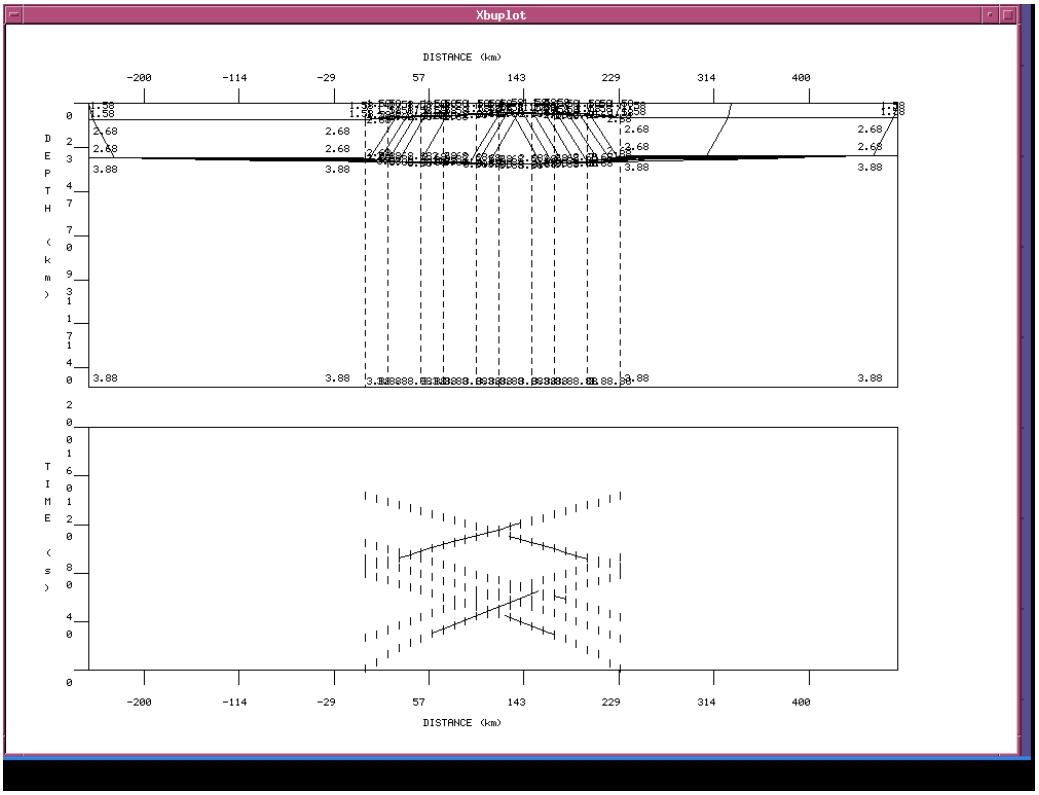

Figure C14– Ray inverse tracing model for LME-1C EW line, with a three layer model. Depths are in km and velocities in km/s.

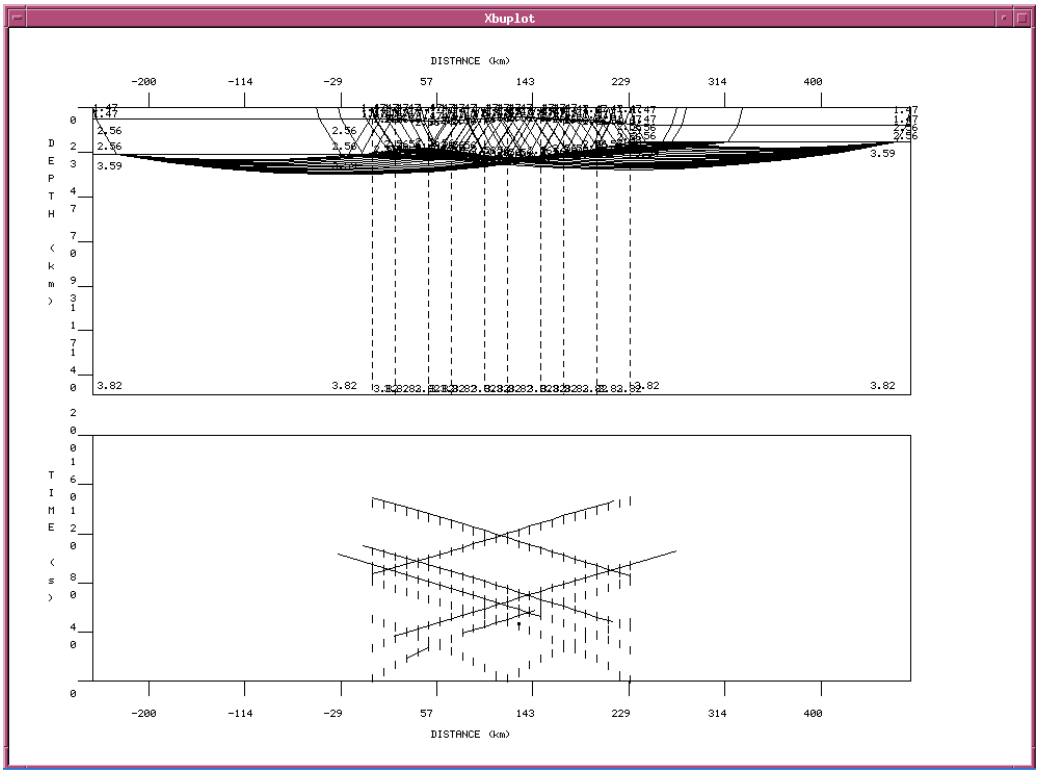

Figure C15 – Ray inverse tracing model for LME-1E NS line, with a three layer model. Depths are in km and velocities in km/s.

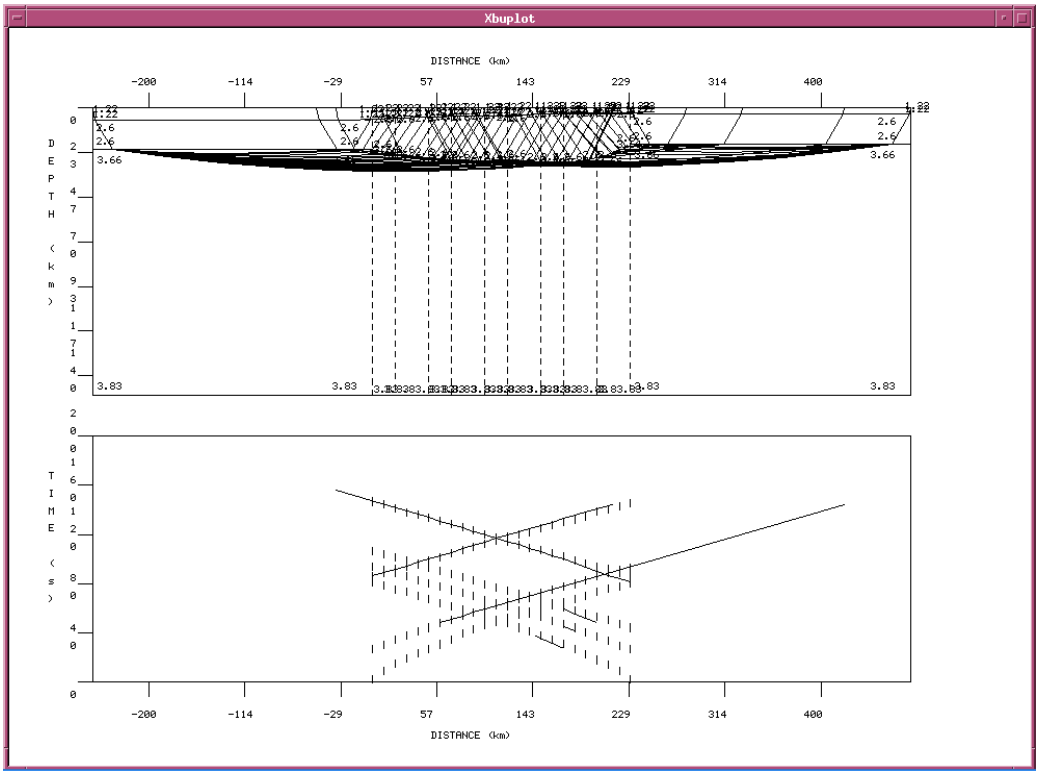

Figure C16 – Ray inverse tracing model for LME-1E EW line, with a three layer model. Depths are in km and velocities in km/s.

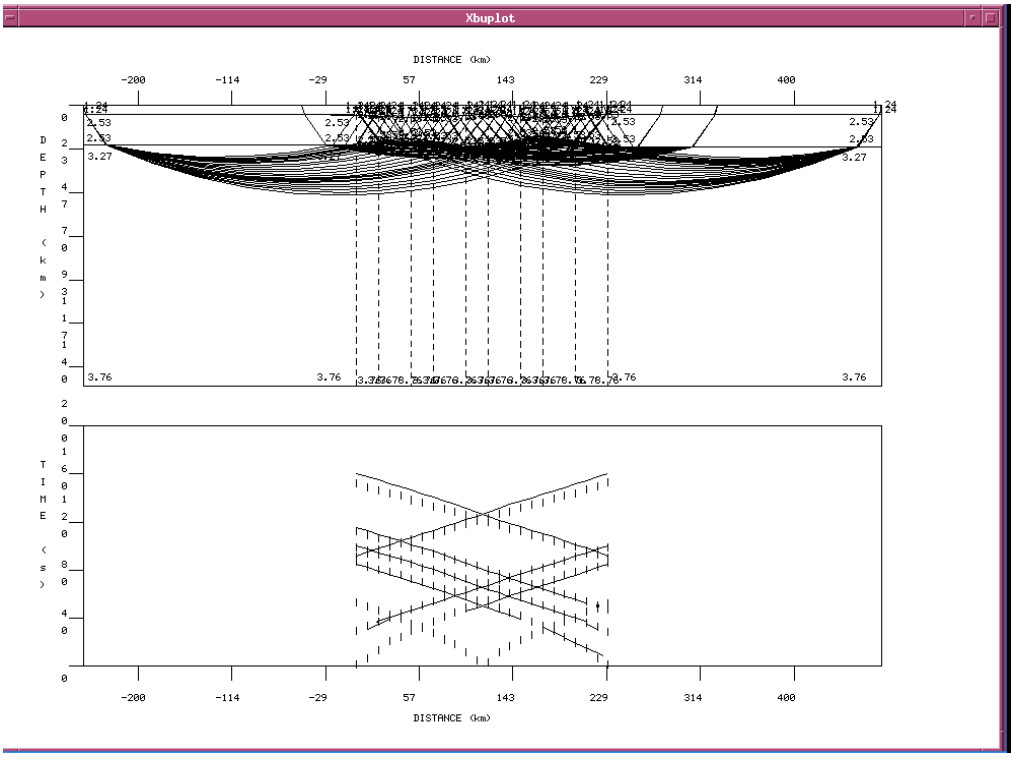

Figure C17 – Ray inverse tracing model for LME-3W NS line, with a three layer model. Depths are in km and velocities in km/s.

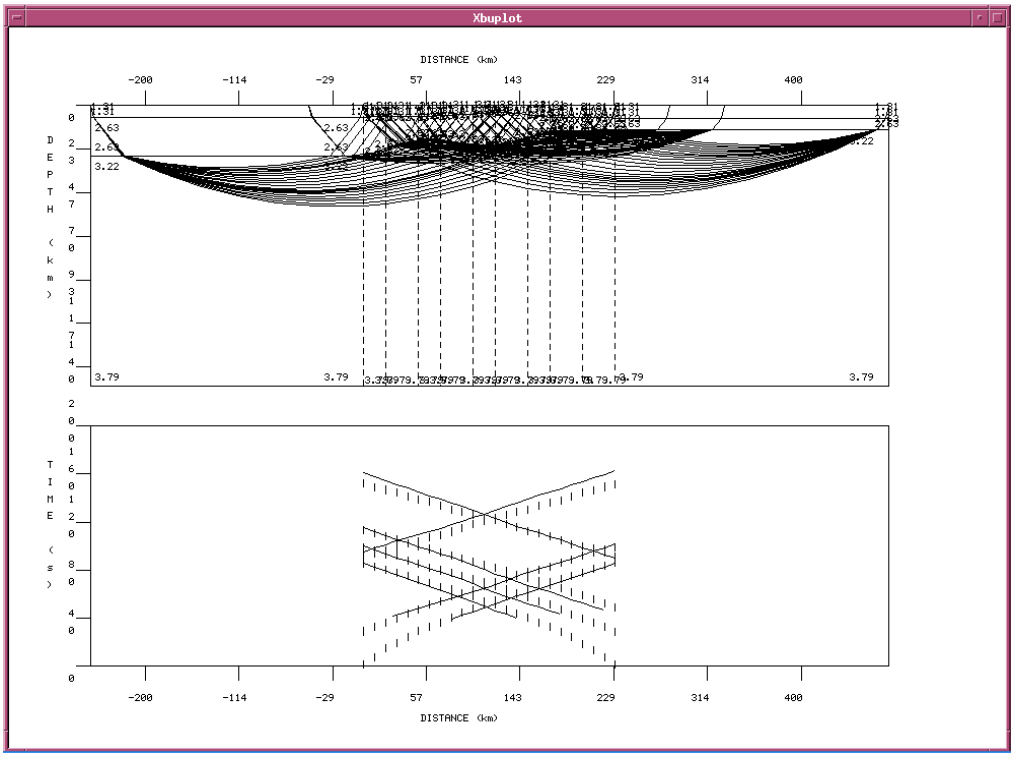

Figure C18– Ray inverse tracing model for LME-3W EW line, with a three layer model. Depths are in km and velocities in km/s.

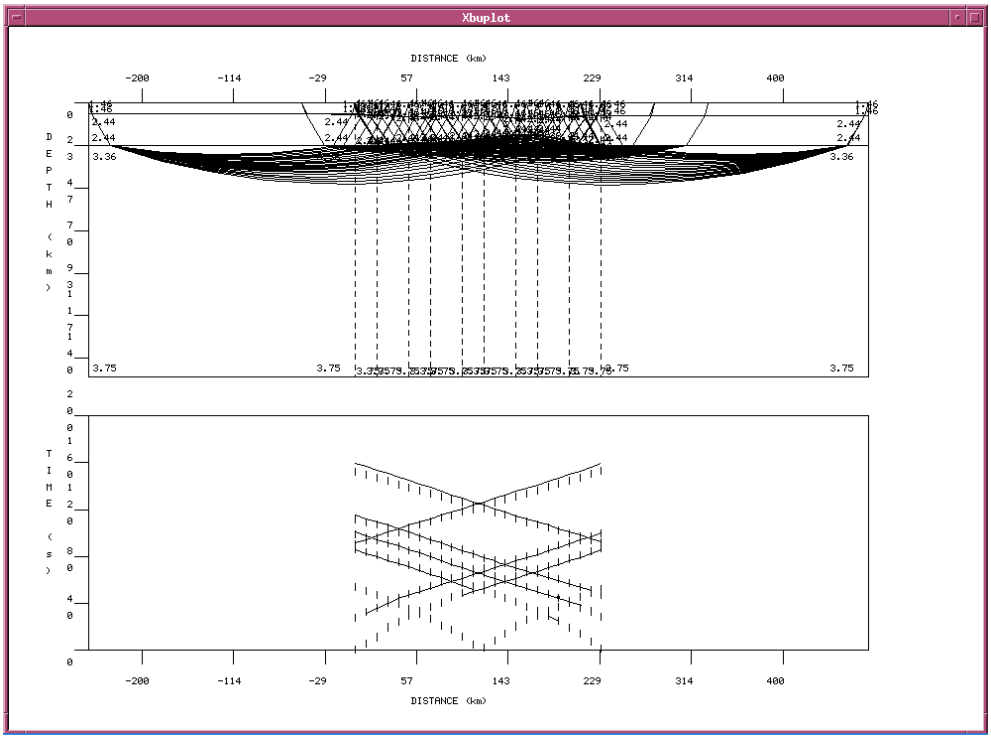

Figure C19 – Ray inverse tracing model for LME-3C NS line, with a three layer model. Depths are in km and velocities in km/s.

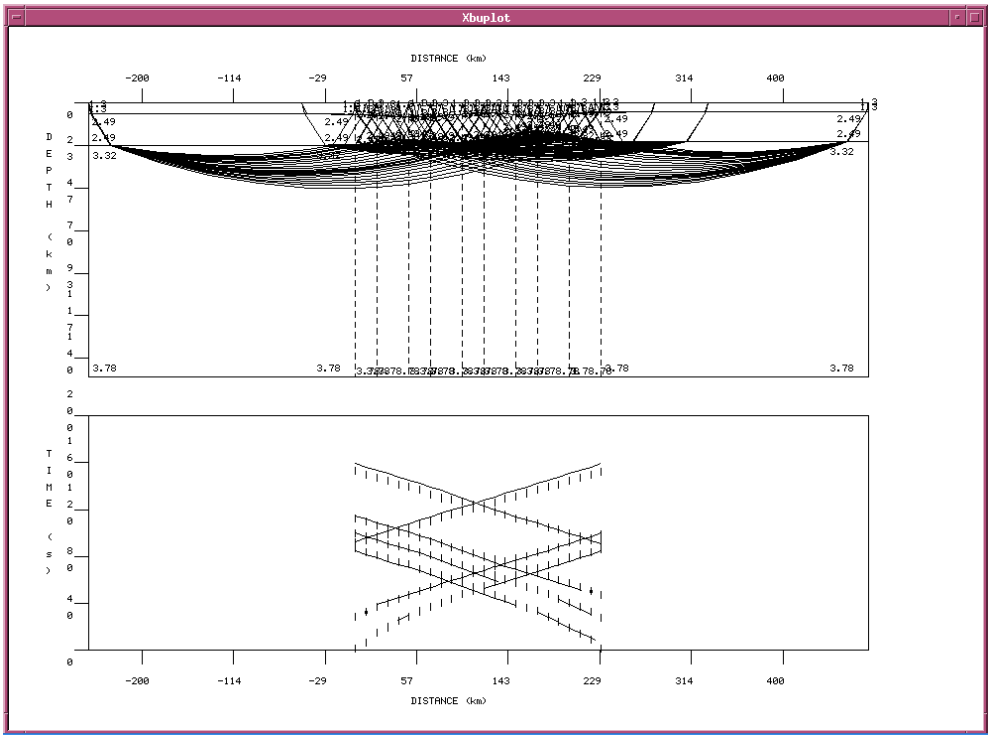

Figure C20 – Ray inverse tracing model for LME-3C EW line, with a three layer model. Depths are in km and velocities in km/s.

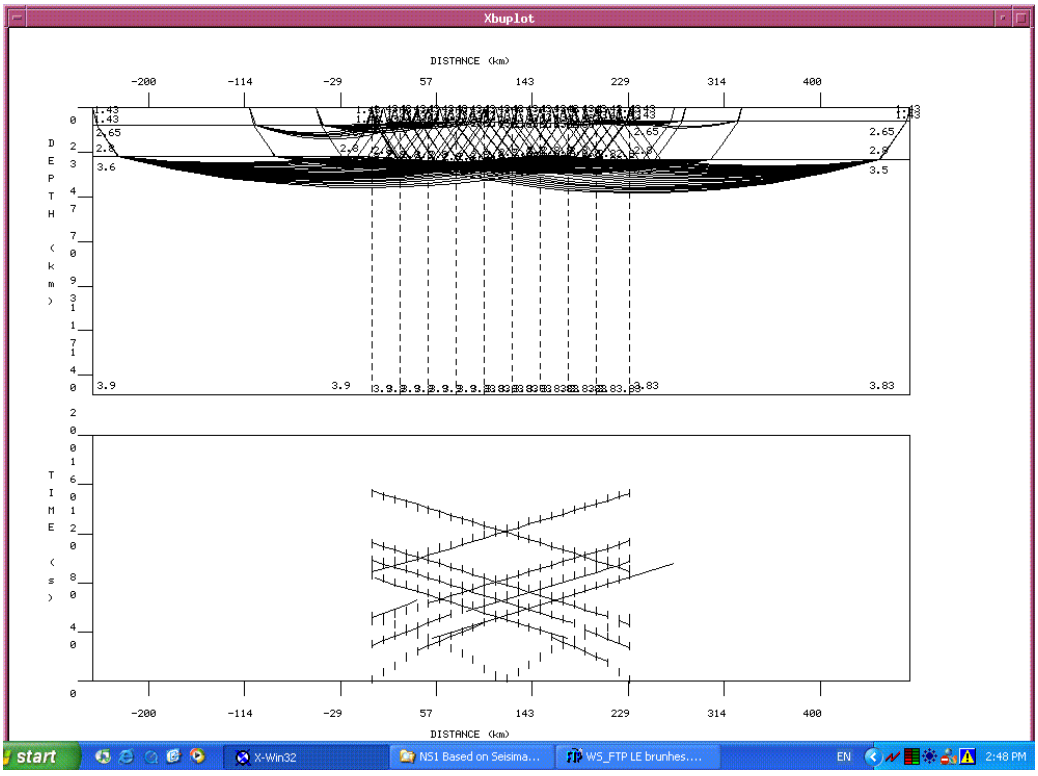

Figure C21 – Ray inverse tracing model for LME-3E NS line, with a three layer model. Depths are in km and velocities in km/s.

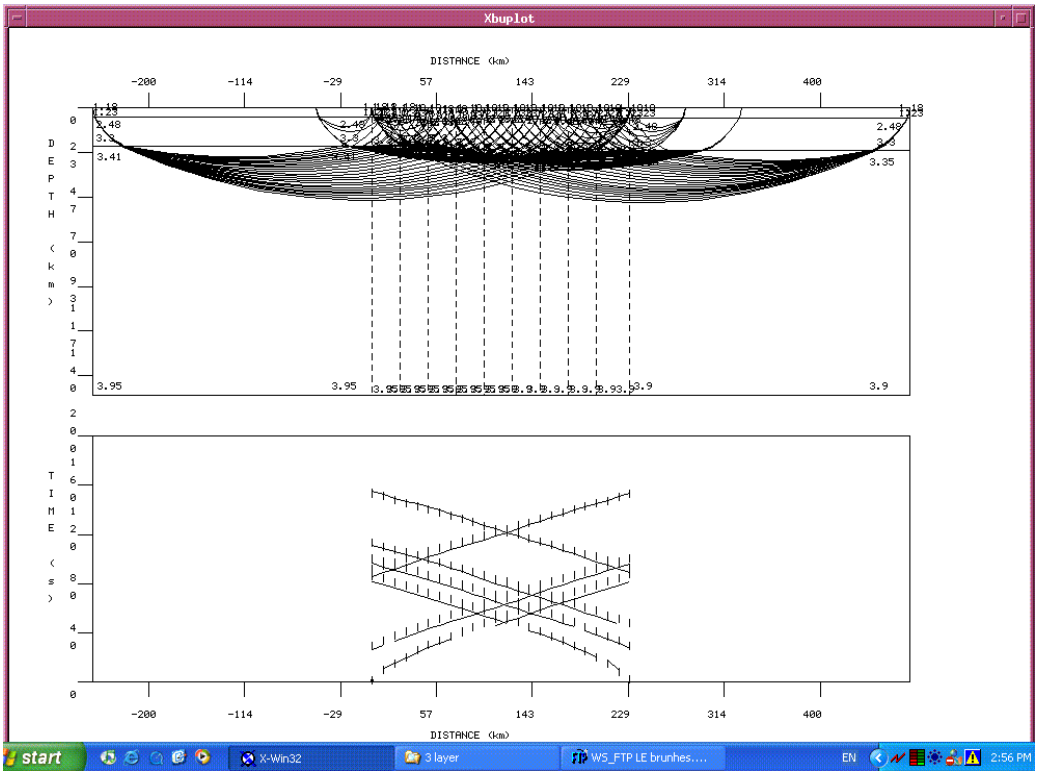

Figure C22 – Ray inverse tracing model for LME-3E EW line, with a three layer model. Depths are in km and velocities in km/s.

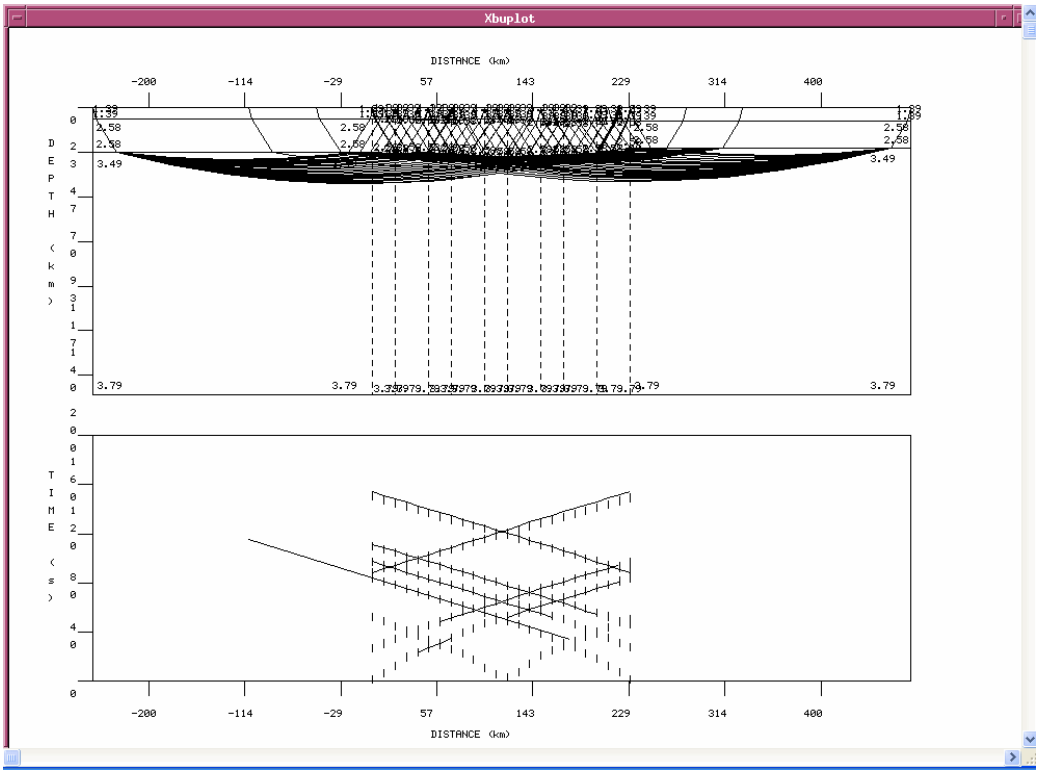

Figure C23– Ray inverse tracing model for ML-CE NS line, with a three layer model. Depths are in km and velocities in km/s.

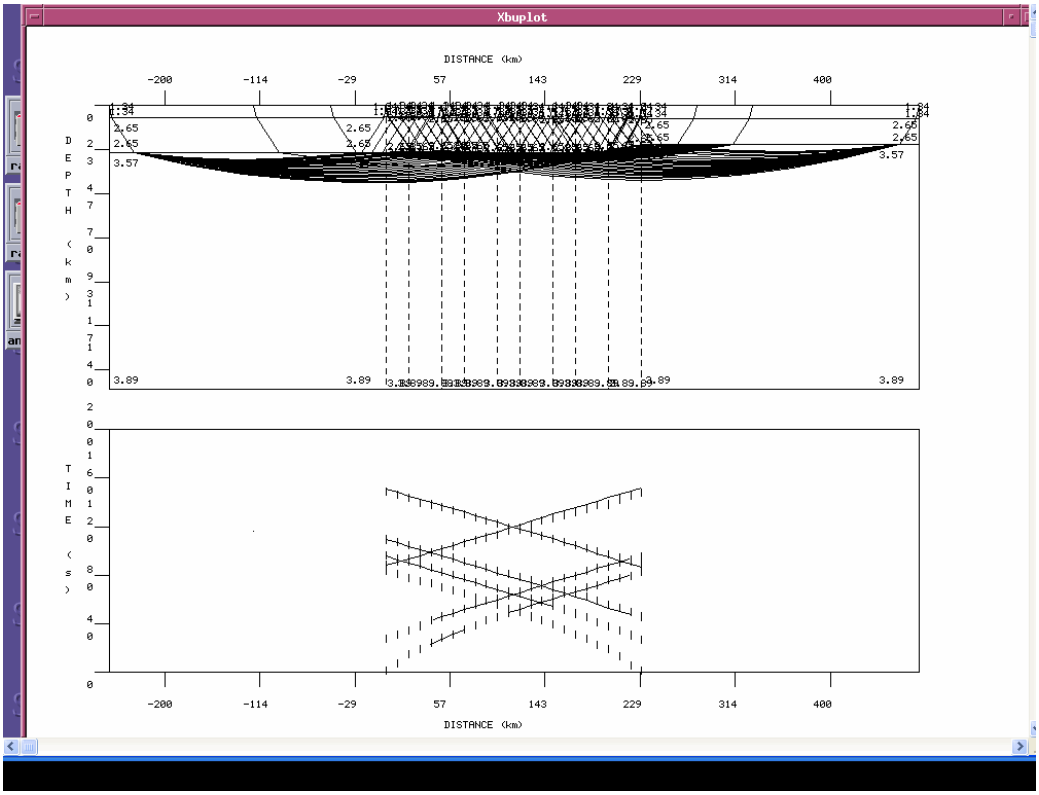

Figure C24 – Ray inverse tracing model for ML-CE EW line, with a three layer model. Depths are in km and velocities in km/s.